

**ACCURACY IMPROVEMENT IN ROBOTIC MILLING THROUGH  
DATA-DRIVEN MODELLING AND CONTROL**

A Dissertation  
Presented to  
The Academic Faculty

by

Vinh Nguyen

In Partial Fulfillment  
of the Requirements for the Degree  
Doctor of Philosophy in the  
School of Mechanical Engineering

Georgia Institute of Technology  
August 2020

**COPYRIGHT © 2020 BY VINH NGUYEN**

**ACCURACY IMPROVEMENT IN ROBOTIC MILLING THROUGH  
DATA-DRIVEN MODELLING AND CONTROL**

Approved by:

Dr. Shreyes Melkote, Advisor  
School of Mechanical Engineering  
*Georgia Institute of Technology*

Dr. Steven Liang  
School of Mechanical Engineering  
*Georgia Institute of Technology*

Dr. Thomas Kurfess  
School of Mechanical Engineering  
*Georgia Institute of Technology*

Dr. Roshan Vengazhiyil  
Industrial and Systems Engineering  
*Georgia Institute of Technology*

Dr. Stephen Balakirsky  
Robotic Systems and Technology Branch  
*Georgia Tech Research Institute*

Date Approved: [July 07, 2020]

## **ACKNOWLEDGEMENTS**

I would like to greatly thank the students and faculty of the PMRC for help with their support. I would like to thank Boeing for providing feedback and funding for this project. I would like to thank Dr. Melkote for his guidance as an advisor, both with my Master's and PhD in addition to life guidance. I would also like to thank Dr. Liang, Dr. Kurfess, Dr. Balakirsky, and Dr. Joseph for their time to be on my committee. I would like to thank my family and many friends for making sure I never forget the value of being a good person. I would like to thank my wife Ye Qi for her support throughout my time at Georgia Tech and many years to come.

# TABLE OF CONTENTS

ACKNOWLEDGEMENTS	iii
LIST OF TABLES	vi
LIST OF FIGURES	vii
LIST OF SYMBOLS AND ABBREVIATIONS	ix
SUMMARY	xi
CHAPTER 1. Introduction	1
1.1 Motivation	1
1.2 Research Objectives	3
1.3 Approach	3
1.4 Thesis Outline	5
CHAPTER 2. Literature Review	6
2.1 Modelling of Robot Tool Tip Dynamics	6
2.2 Minimizing Tool Tip Vibrations in Robotic Milling	9
2.3 Calibration of Robot FRF Models	13
2.4 Summary	16
CHAPTER 3. Data-Driven Modeling of the Modal Properties of a 6-DOF Industrial Robot	17
3.1 Introduction	17
3.2 Modal Analysis Experiments	17
3.2.1 Experimental Setup	18
3.2.2 Results	22
3.3 Gaussian Process Regression Model	24
3.3.1 Model Description	24
3.3.2 Validation	25
3.4 Comparison of Analytical Model with Experiments	28
3.4.1 Analytical Cartesian Stiffness and Inertia Models	29
3.4.2 Comparison with Measured Modal Parameter Values	33
3.5 Prediction of Tool Tip Vibrations	34
3.5.1 Experimental Setup	35
3.5.2 Prediction of Robot Tool Tip Vibrations during Milling	37
3.5.3 Results	40
3.6 Summary	44
CHAPTER 4. Pose-Dependent Optimal Control of Vibrations in Robotic Milling	46
4.1 Introduction	46
4.2 Data-Driven Model Calibration Experiments	47
4.2.1 Experimental Setup	47
4.2.2 Modal Analysis Results	48

4.2.3	GPR Model Cross Validation Results	49
4.3	Optimal Control Methodology	50
4.3.1	Linear Quadratic Regulator	50
4.3.2	Offset Mass Experiments	53
4.3.3	Pose-Dependent Controller versus Constant Gain Controller	56
4.4	Milling Experiments	60
4.4.1	Experimental Setup	60
4.4.2	Vibration Measurements	63
4.4.3	Part Surface Measurements	66
4.5	Summary	68
CHAPTER 5. Hybrid Statistical Modelling of Robot Frequency Response Function		70
5.1	Introduction	70
5.2	Hybrid Modelling Methodology	72
5.2.1	FRF Computation using EMA	72
5.2.2	FRF Computation using OMA	72
5.2.3	Initial Model Calibration	73
5.2.4	Bayesian Updating with OMA-based FRFs	74
5.3	OMA and EMA Experiments	76
5.3.1	EMA Experiments	76
5.3.2	OMA Experiments	78
5.4	Hybrid Statistical Modeling Evaluation	81
5.4.1	Prediction Accuracy	82
5.4.2	Updating Iterations	83
5.5	Summary	84
CHAPTER 6. Conclusions and Recommendations		86
6.1	Conclusions	86
6.2	Original Contributions	88
6.3	Recommendations for Future Work	88
APPENDIX A. Modal Parameter Measurements		90
REFERENCES		96

## LIST OF TABLES

Table 1	Ranges of tested locations. Cartesian units are in the robot base frame.	22
Table 2	Correlation coefficient and Root Mean Square Error (RMSE) values from cross validation.	27
Table 3	Test robot joint angles for compliance experiments (degrees)	31
Table 4	Measured joint stiffness values (x 10 <sup>6</sup> Nm/rad)	31
Table 5	Joint angles for the start and end points of the linear robot path utilized in the impact hammer experiments. Units are in degrees.	48
Table 6	Correlation coefficients and RMSE values from cross validation.	50
Table 7	Start and end vibration amplitudes. Units are in mm.	60
Table 8	GPR model predictions at robot Positions 1 and 2.	62
Table 9	Optimal control gains.	63
Table 10	RMS vibration amplitude results (mm) for milling experiments. “Open” refers to open loop and “Control” refers to LQR control.	64
Table 11	RMS surface deviations (in mm) in milling experiments. “Open” refers to open loop and “Control” refers to closed-loop optimal control.	68
Table 12	RMSE of FRF predictions (all units in $\mu\text{m}/\text{N}$ ).	82
Table 13	Number of optimization iterations for complete retraining of GPR models vs. using model updating with OMA-based FRFs.	84

## LIST OF FIGURES

Figure 1	Summary of approach.	5
Figure 2	Experimental setup for joint stiffness identification.	7
Figure 3	Workpiece surface before and after deformation compensation using material removal rate control.	11
Figure 4	Impact hammer experiments conducted in a 6-dof robot at 3 different locations along the tool tip to calibrate a pose-dependent FRF model.	14
Figure 5	Close-up view of robot modal test setup.	19
Figure 6	Measured robot end effector FRF (solid line) and its corresponding second order transfer function fit (dashed).	21
Figure 7	Results of the impact hammer tests.	23
Figure 8	Cross validation residual plots.	26
Figure 9	Relative errors between the measured and predicted values of the modal parameters in external validation tests.	28
Figure 10	Schematic of the static compliance experiments.	30
Figure 11	Relative errors in the natural frequency and stiffness between the analytical model and impact hammer measurements.	34
Figure 12	Robot poses and corresponding (top) joint angles (degrees) and (bottom) Cartesian XYZ (mm), Rx, Ry, and Rz (degrees) used in the milling experiments.	36
Figure 13	Simplified structural dynamics model of the robotic milling system.	37
Figure 14	Frequency decomposition of the measured milling forces.	39
Figure 15	Measured and predicted FRFs for the two robot positions.	40
Figure 16	Representative tool tip deflections during robotic milling experiments.	42
Figure 17	Comparison of predicted and measured average peak-to-valley tool tip vibration amplitudes.	43
Figure 18	Start and end points for impact hammer experiments.	47

Figure 19	Modal parameter trends estimated from impact hammer tests.	49
Figure 20	Control implementation block diagram.	53
Figure 21	a) Robot and b) zoomed in tooling setup for offset mass experiments.	55
Figure 22	Offset mass experiment results for spindle speeds of (a) 480 RPM, (b) 960 RPM, and (c) 1440 RPM.	56
Figure 23	LQR gains for (a) $w_1$ and (b) $w_2$ along the path.	58
Figure 24	Offset mass experiment results.	59
Figure 25	Robot poses for milling experiments.	61
Figure 26	Vibration data with and without LQR control for (a) Test 1 and (b) Test 8.	65
Figure 27	Spectral decomposition of the vibration data for (a) Test 1 and (b) Test 8.	66
Figure 28	CMM results for (a) Test 1 and (b) Test 8.	67
Figure 29	Example of hybrid modelling approach.	67
Figure 30	Robot configurations for impact hammer experiments.	71
Figure 31	Robot FRFs computed from EMA experiments.	78
Figure 32	Milling experimental setup for OMA.	79
Figure 33	Measured a) milling forces and b) robot vibrations obtained in the longer tool path OMA experiment.	80
Figure 34	Top-down view of the calibration and validation points used in the experiments.	81
Figure 35	Model prediction a) before and b) after updating.	83

## LIST OF SYMBOLS AND ABBREVIATIONS

$c$	Data-driven model observation
$\mu$	Gaussian Process Regression basis function
$p$	Robot pose
$\mathcal{C}(p, p')$	Covariance matrix
$\sigma_l$	Characteristic length scale
$\sigma_f$	Pose standard deviation
$y$	Observation point
$p_*$	Query robot pose
$\sigma^2$	Model variance
$\bar{c}_*$	Gaussian Process Regression mean prediction
$\eta_*$	Gaussian Process Regression covariance prediction
$\mathbf{K}$	Cartesian stiffness matrix
$\mathbf{J}(\boldsymbol{\theta})$	Robot Jacobian
$\mathbf{K}_c$	Complementary stiffness matrix
$\Delta$	Cartesian deflection
$v$	Applied wrench
$\mathbf{K}_\theta$	Joint stiffness matrix
$\mathbf{M}$	Cartesian mass matrix
$\mathbf{I}_i$	Rotational inertia matrix about joint $i$
$\rho$	Mass density
$\mathbf{C}$	Cartesian damping matrix
$\mathbf{F}$	External milling force

$\delta_p$	State space vector
$u_p$	Controller command
$T$	System sampling time
$w_n$	Natural frequency
$\zeta$	Damping ratio
$m$	Modal mass
$c$	Damping coefficient
$k$	Modal stiffness
$\mathbf{W}$	State feedback gain vector
$J$	Linear Quadratic Regulator cost function
$F_c$	Force due to centripetal acceleration
$t$	Time
$\Omega$	Spindle rotational speed
$m_o$	Point mass in offset mass experiments
$d$	Distance along path
$T(f)$	Power Spectral Density of the robot tool tip vibration
$X(f)$	Power Spectral Density of input force
$H(f)$	Power Spectral Density of robot structure
$N(f)$	Power Spectral Density of vibration sensor noise
$P(y p, \theta)$	Log likelihood function
$\theta$	Set of hyperparameters

## SUMMARY

Six degree of freedom (6-dof) articulated arm industrial robots are promising candidates for aerospace machining operations such as milling due to their low-cost and large workspace compared to Computer Numerical Control (CNC) machine tools. However, the instantaneous position accuracy of industrial robots during milling is dependent on the vibratory behavior of the end effector tool tip. Consequently, it is important to model and predict the robot's tool tip vibration as the arm configuration changes over the workspace. This dissertation addresses the modeling, prediction, and control of instantaneous tool tip vibrations of a 6-dof industrial robot over its workspace using data-driven methods.

First, a data-driven modeling approach utilizing Gaussian Process Regression (GPR) of data acquired from modal impact hammer experiments to predict the modal parameters of a 6-dof industrial robot as a function of its arm configuration is presented. The GPR model is found to be capable of predicting the robot's dominant natural frequency of vibration, stiffness, and damping coefficient in its workspace with root mean squared errors of 3.31 Hz, 150 KN/m, and 810 Ns/m, respectively. The predicted modal parameters are used to predict the average peak-to-valley vibrations of the tool tip during robotic milling. The results show that the average peak-to-valley vibrations predicted by the model follow the experimental trends with a maximum error of 0.028 mm. The prediction errors are attributed to the fact that the model only predicts the modal parameters corresponding to the dominant mode of vibration instead of the entire Frequency Response Function (FRF) of the robot.

The GPR model is also used to create a Linear Quadratic Regulator (LQR) based pose-dependent optimal controller to suppress tool tip vibrations of a 6-dof industrial robot during milling. Robotic milling experiments show that the LQR controller reduces tool tip vibration amplitudes by an average of 47%. However, offset mass experiments show that the optimal controller has a bandwidth limitation of 24 Hz due to an intrinsic delay in the robot controller response to control commands.

Finally, a hybrid statistical modelling approach that augments the GPR model of the robot's pose-dependent FRF derived from experimental modal analysis, i.e. impact hammer tests, with the robot's FRF derived from operational modal analysis, which utilizes milling forces and tool tip vibrations to compute the FRF, is presented. The hybrid model augmentation approach is demonstrated to be an efficient method to improve the prediction accuracy of the robot's FRF with minimal optimization iterations. Specifically, the hybrid model is shown to reduce the root mean squared errors in predicting the FRF by 34% and the number of optimization iterations by 50%.

# CHAPTER 1. INTRODUCTION

## 1.1 Motivation

Gantry type Computer Numerical Control (CNC) machine tools are currently used for machining of large structural parts in the aerospace industry. However, such machine tools suffer from several drawbacks including their large footprint, high cost and limited versatility to perform multiple tasks in a manufacturing environment. In contrast, industrial robots have a smaller footprint, cost less (30% cheaper for the equivalent workspace) [1], and possess the versatility to perform a variety of manufacturing tasks including material removal and metrology. Thus, there is considerable interest in the aerospace sector to utilize industrial robots for machining and other manufacturing tasks [2].

However, before industrial robots can be used for high accuracy aerospace manufacturing tasks such as high force milling operations they must overcome fundamental limitations arising from their relatively large compliance (demonstrated to be approximately 50 times more compliant) [3], which negatively affects part dimensional accuracy and surface finish [4]. In addition, the vibration characteristics of the robot at its tool tip vary with robot configuration (or pose) within its work volume [5, 6]. Knowledge of robot tool tip vibration characteristics is vital to selecting the optimal machining parameters to minimize undesirable process behavior including structural resonance and self-excited vibrations (chatter) during milling [7]. Consequently, it is important to develop a model to predict the robot's pose-dependent vibration behavior as a function of its compliance, resonant frequency, and damping. Such a model can then be used to predict the robot's tool tip vibrations, which influence its instantaneous position accuracy.

However, existing analytical and numerical models cannot accurately simulate the dynamic behavior of 6-dof industrial robots due to modeling assumptions and uncertainty in calibration of the joint stiffnesses and link moments of inertias. Therefore, a different modeling approach is required to predict the robot's modal properties as a function of its pose or its corresponding tool tip position in task or Cartesian space.

While a model that enables offline process parameter selection is useful for minimizing the robot's tool tip instantaneous positioning inaccuracies during milling, on-line compensation is necessary to further improve the robot's tool tip accuracy when offline optimization is insufficient. Because the periodic forces in milling result in tool tip vibrations that reduce part accuracy, implementing a controller that suppresses these tool tip vibrations is also useful for improving part quality. Vibration suppression controllers usually require manual tuning of controller gains to produce the desired performance [8, 9]. However, because the controller performance depends on pose-dependent modal parameters of the robot, manually tuned controllers are only valid for a specific robot arm configuration. Therefore, a control technique to suppress tool tip vibrations in articulated arm robots without manual controller tuning is required.

Creating a data-driven model that accurately describes how the robot's modal parameters vary over its workspace requires off-line model calibration using vibration data from modal impact hammer tests (or Experimental Modal Analysis) performed at many discrete robot configurations or points in the workspace. This can be very time consuming and can result in long robot downtimes, especially if a large workspace is involved. On the other hand, low density sampling of the robot's workspace can lead to model prediction inaccuracies for arm configurations not utilized in the model calibration process.

Alternatively, Operational Modal Analysis [10], a method that utilizes force and vibration data obtained from the dynamic system during its operation, can provide convenient and dense sampling of the modal parameters corresponding to the continuously changing robot configurations along the robot tool path without significant downtime. However, application of this method to robotic milling is limited by the lack of an intelligent method to determine the tool paths required to adequately sample the robot's workspace. Therefore, a hybrid modeling approach that can combine the advantages of both off-line and operational modal analysis to create a cost-effective and sufficiently accurate model for predicting the modal parameters of an industrial robot over its workspace as a function of arm configuration is desirable.

## **1.2 Research Objectives**

In light of the above motivations, the research objectives of this thesis are:

1. Predict the pose-dependent tool tip vibrations of industrial robots during milling operations.
2. Suppress tool tip vibrations during robotic milling using closed-loop control without manual tuning.
3. Efficiently calibrate models that predict the modal parameters of an industrial robot over its workspace.

## **1.3 Approach**

The above research objectives are pursued in this thesis through the tasks summarized in Figure 1. First, a data-driven model to predict the robot's modal parameter

variation within its workspace is developed. A data-driven modelling approach is proposed as the most accurate method to model the robot's modal properties (natural frequency, stiffness, and damping coefficient) because it does not rely on modelling assumptions inherent in analytical modelling. The data-driven model is created from modal parameters determined from Experimental Modal Analysis (EMA), which involves conducting impact hammer tests at discrete points in the robot's workspace. The data-driven model is then validated through modal impact hammer measurements and compared to the results obtained from a well-established analytical model of robot stiffness and natural frequency. In addition, the data-driven model is used to predict the robot's tool tip vibrations in milling applications by using the cutting forces as inputs to the second order transfer function created from the modal parameters determined from the data-driven model. Next, an optimal control methodology is used to suppress robot vibrations in robotic milling. The data-driven model of the robot's modal parameters is used to automatically calculate the gains of the optimal controller as a function of changing robot arm configuration. It is shown that the optimal control methodology is able to suppress robot vibrations at different points in the workspace. The controller performance is then evaluated using robotic milling experiments. Finally, a hybrid statistical modelling method that augments the data-driven model created from impact hammer tests with Frequency Response Functions (FRFs) determined from Operational Modal Analysis (OMA), that is from milling forces and robot tool tip displacements generated during the robotic milling operation, is presented. The proposed approach is evaluated by quantifying the prediction accuracy and model calibration efficiency improvements obtained from the hybrid approach.

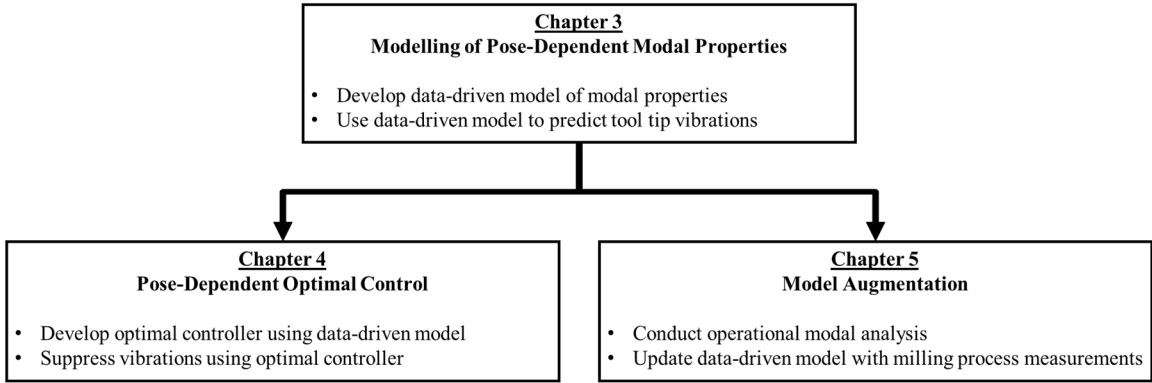


Figure 1. Summary of approach.

## 1.4 Thesis Outline

The remainder of this thesis is organized as follows. Chapter 2 presents a literature review to justify the research objectives of this thesis. Chapter 3 presents the data-driven modelling approach to predict the robot’s modal properties and tool tip vibrations within its workspace. Chapter 4 presents a pose-dependent optimal controller that utilizes the data-driven model to minimize the robot tool tip vibrations during milling. Chapter 5 presents the hybrid statistical modelling approach to augment the data-driven model previously calibrated by impact hammer test data with operational milling process data. Finally, the major conclusions, contributions, and recommendations for future work are given in Chapter 6.

## CHAPTER 2. LITERATURE REVIEW

This chapter presents an overview of the literature relevant to the research objectives of this thesis. The review is divided into three topics: 1) modelling of robot tool tip dynamics, 2) minimizing tool tip vibrations in milling, and 3) calibration of robot pose-dependent modal parameter models.

### 2.1 Modelling of Robot Tool Tip Dynamics

Analytical models have been developed to predict the dynamic properties (specifically the Cartesian mass and stiffness properties) of the robot end effector as a function of robot arm configuration or tool tip position in the workspace. The end effector stiffness of industrial robots have been calculated using models that characterize the robot's joint stiffness values and transform them from the joint space to the Cartesian space [11-13]. Specifically, the Cartesian stiffness as a function of the pose-dependent Jacobian  $\mathbf{J}(\theta)$  and joint stiffness  $\mathbf{K}_\theta$  is expressed as follows

$$\mathbf{K} = \mathbf{J}(\theta)^{-T} \mathbf{K}_\theta \mathbf{J}(\theta)^{-1} \quad (1)$$

Figure 2 shows an experimental setup used to identify the joint stiffness matrix  $\mathbf{K}_\theta$ . To identify the stiffness, a known static force decomposed into forces and torques along each Cartesian axis is applied to the end effector and the corresponding static displacement is measured. The measured forces and displacements are used to determine the Cartesian stiffness  $\mathbf{K}$ , and Equation (1) is used to calculate  $\mathbf{K}_\theta$ . However, these models assume that the robot's joint stiffnesses are constant throughout its workspace and therefore the joint stiffness models assume a linear relationship between the torque applied at the joint and

the corresponding joint deflection. However, this is not a valid assumption due to the presence of gear backlash in the joints and torque limits of the joint motors [14]. Schneider et al. [15] accounted for 6-dof deformation at the joints but failed to consider link stiffnesses. Hence, joint stiffness models assume infinitely rigid links, which can result in over-prediction of the Cartesian stiffness. Mousavi et al. [16] considered all modes of deflection (3 translational and 3 rotational) of the joints to derive multiple modes of vibration of the robot. However, their model incorrectly assumed that the robot links were made of aluminum and the work did not experimentally validate the model.

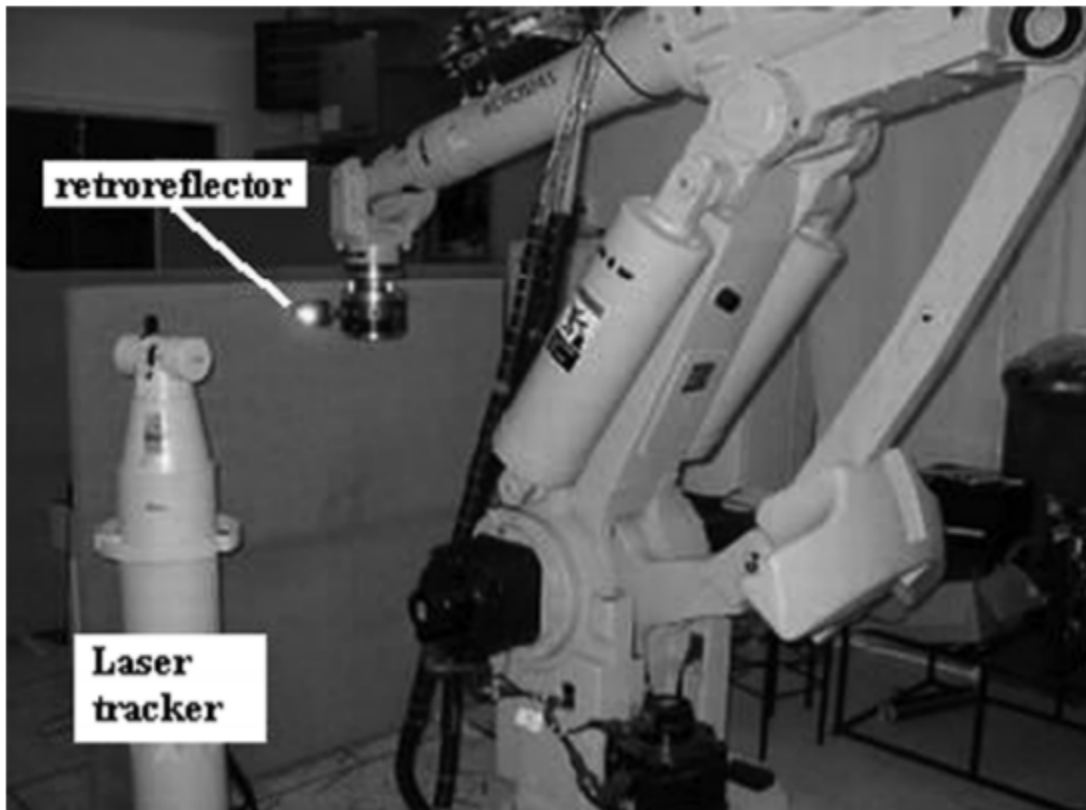


Figure 2. Experimental setup for joint stiffness identification [13].

A common approach to computing the mass matrices of 6-dof industrial robots is to identify the rotational moment of inertia about each joint and transform the joint inertias

to an effective mass matrix at the end effector position. This approach is expressed as follows

$$\mathbf{M} = \sum J_i(\theta)^T \mathbf{I}_i J_i(\theta) \quad (2)$$

where  $\mathbf{I}_i$  is the moment of inertia for link  $i$ . However, accurate determination of the moment of inertia about each joint requires knowledge of the distribution of mass within each link and therefore requires proprietary information of the motor placements and link construction. Armstrong et al. [17] and Pan et al. [18] assume that the mass of the robot links are uniformly distributed, which is an incorrect assumption since the mass distribution around the joint motors are denser than the mass distribution in the links [19]. In addition, damping characteristics of robots are difficult to calculate analytically. Adhikari et al. [20] consider structural damping by assuming the damping coefficient to be a linear combination of the stiffness and mass matrices, referred to as Rayleigh damping. However, constant linear coefficients are not a valid assumption in the robot workspace where the stiffness and mass change at different rates than the damping coefficient. This is because the joints experience backlash, which influences the joint stiffness at a different rate than friction-induced damping [21]. In addition, analytical models primarily predict the modal parameters corresponding to a finite number of modes as opposed to the entire FRF. Therefore, analytical models that predict the robot's modal parameters are inherently limited in their ability to predict the entire FRF of the robot.

In the context of generalized dynamical systems, methods to predict the changing system dynamic parameters as a function of a scheduling parameter have been explored [22]. Specifically, methods have been developed to interpolate between local time invariant

state-space matrices using intermediate state-space matrix transformations to represent time-varying matrices. For instance, Ferrati et al. [23] demonstrated a method to transform local time invariant state space matrices into a common state space form to interpolate between significantly differing state space matrices. However, the underlying parameterization of state space models is limited to polynomial functions, and the sinusoidal terms in the Jacobian shown in Equations (1) and (2) clearly illustrate that the robot vibratory cannot be expressed in this fashion. In addition, although methods to predict modal vibration parameters of machine tools based on the tool tip position have been presented [24, 25], unlike a 6-dof robot, a machine tool generally has fewer degrees of freedom and its modal parameters do not vary significantly over its workspace.

Therefore, accurate simulation of the time-varying vibration response of 6-dof industrial robots is difficult due to the inherent uncertainties in the mass distribution and internal link structure and inaccurate assumptions concerning the structural stiffness and damping. In addition, flexible end effector tooling (e.g. end mills with large extensions) requires further calibration of the analytical models. Hence, a data-driven modelling method that accurately describes the robot tool tip modal parameters for robotic milling applications within its workspace is necessary.

## **2.2 Minimizing Tool Tip Vibrations in Robotic Milling**

Methods to improve robotic machining accuracy by minimizing tool tip vibrations can be divided into two classes: off-line and on-line methods. Off-line model-based methods utilize milling structural dynamic models to select the machining parameters (e.g. feed and speed) and robot poses that minimize robot vibrations. Kaldestad et al. [26]

utilized a pose-dependent static robot deflection model to select the appropriate tool feed direction and therefore did not consider the influence of robot vibrations. Off-line tool path planning using the robot modal parameters involves selecting the correct feed direction to minimize chatter instabilities arising from regenerative [6, 27, 28] and mode-coupling [7, 29] effects, and selecting the appropriate tool path [30] or robot configuration [31] to reduce the magnitude of stable tool tip vibrations. In addition, part accuracy improvement through deformation compensation, which involves predicting the tool tip deflections generated by an initial tool path and reprogramming a compensated tool path has been reported [15, 32]. Finally, increasing the feed rate has been shown to alter the orientation of the robot's principal stiffness axes relative to the machining force vector due to small changes in the Jacobian matrix arising from elastic deformation of the robot, thereby enabling minimization of mode coupling chatter vibrations [33]. However, off-line methods for vibration suppression must rely on accurate modelling of the robot modal properties, which is difficult to achieve through analytical models, especially for practical machining applications.

Therefore, on-line compensation is necessary to further improve robot tool tip accuracy by accounting for calibration inaccuracies and sources of vibration not considered in off-line models. On-line feedback controllers require an external sensor to measure the instantaneous tool tip position to perform corrective actions based on measured deviations from the nominal tool path. Figure 3 shows the improvement of measuring cutting forces in robotic milling to control the material removal rate to improve surface accuracy [3]. Another example includes wireless force sensor feedback was used to estimate the actual depth of cut, and a corrective action was then implemented to improve the average

positional error [34]. In addition, force sensor feedback was used with proportional control to command the robot feed rate to reduce the average part dimensional error [35]. However, these methods did not consider that the milling process is characterized by large periodic forces that can excite the robot structure dynamics. To address this deficiency, Sörnmo et al. [36] utilized a PID controller to actuate a piezoelectric stage holding the milling head to reduce vibrations experienced by the industrial robot, which held the workpiece. Daniali et al. [37] simulated vibration control in robotic milling through a neurofuzzy controller. In addition, Wang et al. [38] used PD control of an inertial coil actuator to minimize the robot vibrations in milling, as shown in Figure 3.

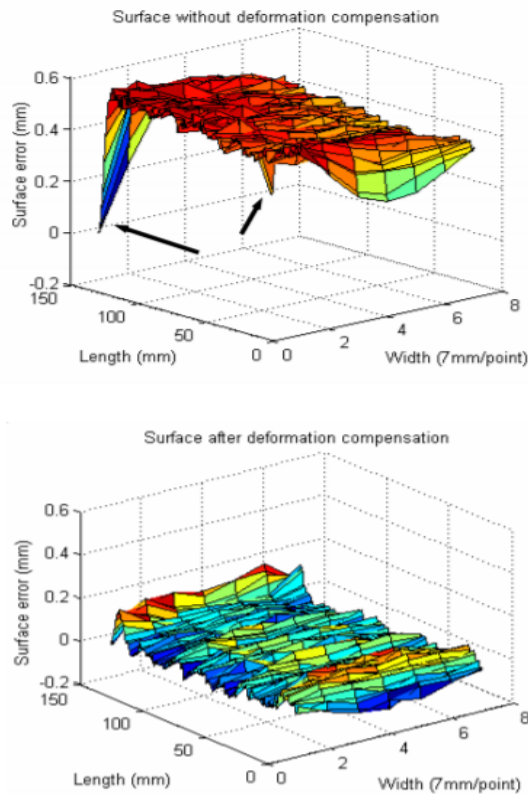


Figure 3. Workpiece surface before and after deformation compensation using material removal rate control [3].

Wang et al. discussed the fundamental limitations of the aforementioned on-line compensation methods. The previously described work on active vibration suppression in robotic machining make use of empirically tuned controllers, which are only valid for a specific robot arm configuration and its corresponding modal vibration response. Alternatively, optimal controllers do not require manual empirical tuning of the controller gains because their control laws are determined by minimization of a cost function, which is derived from a model of the dynamic system [39]. Optimal controllers designed to reduce vibrations due to chatter and forced vibrations have been demonstrated in CNC milling. For instance, a model-based adaptive controller was used to control the feed rate to reduce regenerative chatter vibrations in CNC milling [40]. In addition, a Linear Quadratic Regulator (LQR) was demonstrated to control the force to minimize nonlinear regenerative chatter in CNC milling [41]. A fuzzy controller was used to adjust the spindle speed for vibration suppression in CNC milling operations [9]. In addition, an optimal controller was used to select gain criteria to satisfy a stability condition for disturbance rejection in CNC milling [42]. An adaptive controller was demonstrated for piezoelectric active vibration control in both stable and unstable milling processes [43].

However, to implement optimal control in robotic milling, a controller that accounts for pose-dependent tool tip dynamics of the robot is required, which is not considered in the foregoing studies. Therefore, it is clear from the review of the relevant literature that there is a need for an on-line feedback control methodology that accounts for the pose-dependence of the modal vibration parameters of the milling system (both CNC and industrial robot), which has not been previously investigated. Because the vibration characteristics of the robot tool tip vary with robot pose, the feedback controller gains used

for disturbance rejection must account for changes in the robot's vibration characteristics with arm configuration as it moves along a tool path. However, empirically tuned feedback controllers require manual tuning of the controller gains throughout the robot workspace. Therefore, to efficiently implement vibration suppression in robotic milling, a pose-dependent optimal controller that uses a system model of the robot's tool tip dynamics to automatically determine the controller gains as the arm configuration changes along the tool path is required.

### **2.3 Calibration of Robot FRF Models**

Calibration of pose-dependent structural dynamic models directly from FRFs is usually done through offline Experimental Modal Analysis (EMA). Specifically, EMA utilizes impact hammer tests to determine the FRF since the method is capable of directly obtaining the mode shape and scaling [44]. Generally, EMA is conducted at various points in the workspace to calculate the robot joint stiffness, damping and mass parameters, which are then used in the joint-to-Cartesian space transformation to obtain the Cartesian FRF at the other points in the workspace. For instance, Chen et al. [45] used impact hammer tests with 2-level ( $0^\circ$  and  $90^\circ$ ) combinations of the six joints to calibrate their FRF model as shown in Figure 4.



Figure 4. Impact hammer experiments conducted in a 6-dof robot at 3 different locations along the tool tip to calibrate a pose-dependent FRF model [45].

In addition, EMA was conducted to identify the joint and link parameters (modal mass, stiffness, and damping) in a flexible joint multi-body dynamic model of the robot's modal parameters [46]. EMA has also been used to establish pose-dependent modal parameter models of machine tools [24, 25]. However, FRF measurements for off-line model calibration can only be conducted at discrete robot configurations and therefore require significant off-line testing effort to obtain adequate spatial resolution and coverage. Hence, a method to calibrate models using operational (e.g., machining) data can be useful for maximizing both testing efficiency and spatial resolution.

In the context of milling applications, Operational Modal Analysis (OMA) involves calculation of the milling structure's modal FRF (and modal parameters) using milling force and structural vibration data gathered from the milling operation. OMA has been previously shown to be capable of identifying the structural FRF of CNC machine tools. For instance, Suzuki et al. [47] used OMA on data derived from regenerative chatter cutting

tests to calculate the modal parameters of a CNC machine tool structure. In addition, Poddar et al. [48] and Li et al. [49] implemented random cutting force excitation of CNC milling machines through a novel workpiece design and by programming the feed drives to induce random excitation, respectively. In addition, OMA has been demonstrated for CNC milling [50] and robotic milling applications [51, 52] by utilizing the transmissibility function-based method, though only the mode shape was identified. Another established method to calculate the modal parameters involves the use of Enhanced Frequency Domain Decomposition, where the natural frequency is determined from the time domain zero crossing and the mode shape is determined through empirical fitting [53]. In addition, alternative OMA techniques applicable under stable milling conditions without random excitation have been demonstrated to be capable of only identifying the natural frequency of the structure [54, 55]. This is insufficient for optimal control and for predicting stable vibrations because identification of the natural frequency does not specify the vibration amplitude. However, table milling forces consist of both periodic content and background random noise [56, 57]. In addition, application of OMA in fields outside of manufacturing, such as in vibrating civil structures [58], in-flight helicopters [59], and wind turbines [60], have shown that a force signal that has both periodic and random noise content can generate broadband excitation of the structure and thereby enable estimation of the FRFs.

However, use of only OMA to derive the robot FRFs over its entire workspace is limited by the lack of knowledge of the number, length, and spacing of tool paths required to adequately sample the robot's vibration modes corresponding to different arm configurations over its workspace. Even if a suitable method for identification of the optimal tool paths were available, execution of OMA would be constrained by cumbersome

part fixturing requirements, especially if the workspace is large. Specifically, part fixturing would need to be modified to collect milling force and robot tool tip vibration data for the various tool paths required thereby making the data acquisition process time-consuming and expensive. Hence, a hybrid modeling approach that incorporates FRF measurements from both EMA and OMA can be beneficial for achieving the required modal parameter prediction accuracy over the robot's workspace at an acceptable cost.

## **2.4 Summary**

It can be seen from the literature review that prior work on modelling of pose-dependent robot dynamics and active vibration suppression in robotic milling suffer from at least one of the following drawbacks: 1) use of inaccurate assumptions, 2) failure to consider pose-dependent modal parameters in feedback controllers, and 3) limitations associated with only using either EMA or OMA methods for efficient model calibration. Hence, the existing robot vibration modelling techniques are insufficient for use in off-line and on-line compensation, which in turn limits the practical use of industrial robots in machining applications, especially in the aerospace industry.

The remainder of this thesis describes the data-driven model used to predict the robot's pose-dependent tool tip vibrations in milling, the development of a pose-dependent optimal controller, and the combination of EMA and OMA to obtain pose-dependent FRF models valid over a large workspace.

## **CHAPTER 3. DATA-DRIVEN MODELING OF THE MODAL PROPERTIES OF A 6-DOF INDUSTRIAL ROBOT**

### **3.1 Introduction**

Prediction of the pose-dependent modal parameters of industrial robots are important for manufacturers to select the appropriate process parameters in robotic milling. However, existing analytical models are insufficient for accurately predicting the pose-dependent modal parameters of industrial robots. Thus, the objective of this chapter is to study a statistical modeling approach known as Gaussian Process Regression (GPR) to model and predict the structural dynamic properties (frequency, stiffness, and damping coefficient). First, the modal analysis experiments for determining the robot's dominant modal parameters via EMA at a finite number of pre-defined points in its workspace are described. The modal responses of the robot at the pre-defined points are then used to build the GPR model. The resulting GPR model is then evaluated using cross validation and external validation methods. An established analytical model of the robot tool tip dynamics using Jacobian based methods is compared with the GPR model and experimental data. In addition, the GPR model is used to predict the natural frequency, stiffness, and damping coefficient at two specific robot Cartesian positions and to utilize them in predicting the tool tip vibrations produced during robotic milling at the two positions.

### **3.2 Modal Analysis Experiments**

This section describes the determination of the modal parameters (modal frequency, modal stiffness, and modal damping coefficient) from EMA tests performed on

a 6-dof industrial robot. This is followed by a discussion of how the modal parameters change within the robot workspace.

### *3.2.1 Experimental Setup*

EMA tests were performed on a 6-dof industrial robot (KUKA KR500-3) to determine the modal parameters corresponding to the most dominant vibration mode of the robot tool tip in the excitation direction at different points in the robot's workspace. Note that while the most dominant vibration mode is considered in this work, the robot structure has multiple vibration modes that will influence the frequency response function (FRF) of the robot and thereby introduce additional sources of compliance. In this chapter, the contribution of such additional modes is assumed to be negligible. The Cartesian positions of the robot tool tip where the EMA tests were conducted were confined to a 1.22 x 1.54 m<sup>2</sup> area of the robot cell occupied by an optical breadboard, mounted to the floor of the robot cell, on which the workpiece was attached at a fixed height. Figure 5 shows the experimental setup for the experiments. The vibration response of the robot was measured with a single-axis accelerometer (PCB 352A21) mounted at the tool tip on the tool flank 6 mm from the bottom face. To excite the robot structure, an impact hammer (PCB 086D05) was used to apply an impulse excitation collinear with the accelerometer measurement axis opposite of the impact point. Impact hammer tests were performed in the Cartesian X, Y, and Z directions of the robot's base frame for each test point in the workspace.

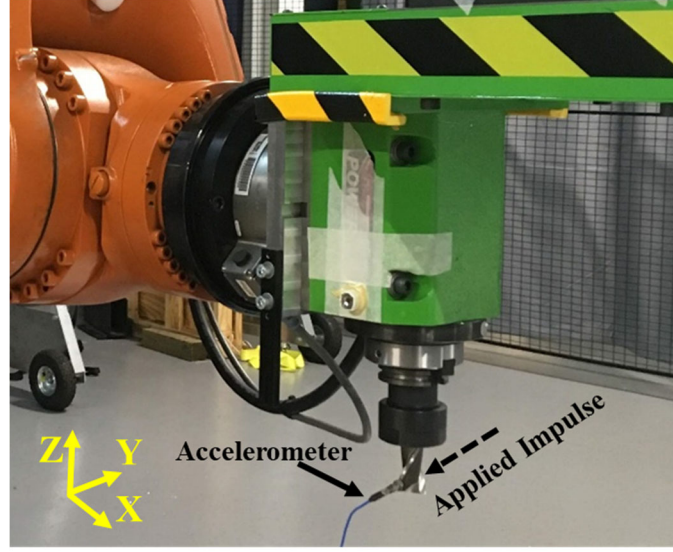


Figure 5. Close-up view of robot modal test setup.

To calculate the FRF from the impact hammer and accelerometer time series measurements, consider the power spectral density of the robot tool tip vibration  $T(f)$  for an impulse force input to be

$$T(f) = X(f)H(f) + N(f) \quad (3)$$

where  $X(f)$ ,  $H(f)$ , and  $N(f)$  are the power spectral densities of the input impulse force, robot structure, and noise of the vibration sensor, respectively. Multiplying Equation (3) by the complex conjugate of  $X(f)$  and transforming each term into the auto and cross spectral densities using Welch's Method [44] results in

$$G_{xt}(f) = G_{xx}(f)H(f) + G_{xw}(f) \quad (4)$$

where  $G_{xt}(f)$ ,  $G_{xx}(f)$ , and  $G_{xw}(f)$  are the force-vibration cross spectral density, the force auto spectral density, and the force-sensor noise cross spectral density, respectively. Note that the cross spectral density  $G_{xw}(f)$  approaches zero after averaging because the vibration

measurement sensor noise and input signal are not correlated. Hence, the following equation can be used to calculate the robot FRF

$$H(f) = \frac{G_{xt}(f)}{G_{xx}(f)} \quad (5)$$

Thus, the FRF of the robot structure can be determined from Equation (5) after calculating the auto spectral density of the input force signal and the cross-spectral density of the force and vibration signals. Figure 6 shows a representative FRF in the Cartesian Y direction of the robot tool tip obtained from impact hammer tests for a particular robot configuration in the workspace. A second order transfer function was fit to the most dominant mode of the FRF to extract the corresponding modal parameters. Note that while the robot consists of several vibration modes for each pose, the most dominant mode in the excitation direction was extracted due to its largest contribution to the tool tip vibration during robotic milling [5]. It is also assumed that the contribution of vibration modes generated in directions orthogonal to the excitation direction (due to cross-coupling) have negligible contribution to the tool tip vibration. Specifically, it was found that the largest compliances in directions orthogonal to the excitation direction were at most 6% of the dominant mode in the excitation direction, and can therefore be assumed to have a negligible effect on the vibration in the excitation direction [6]. Thus, the parameters of the second order transfer function that best fit the FRF's most dominant mode were used to calculate the modal stiffness, damping coefficient, and modal natural frequency for that robot position in the workspace.

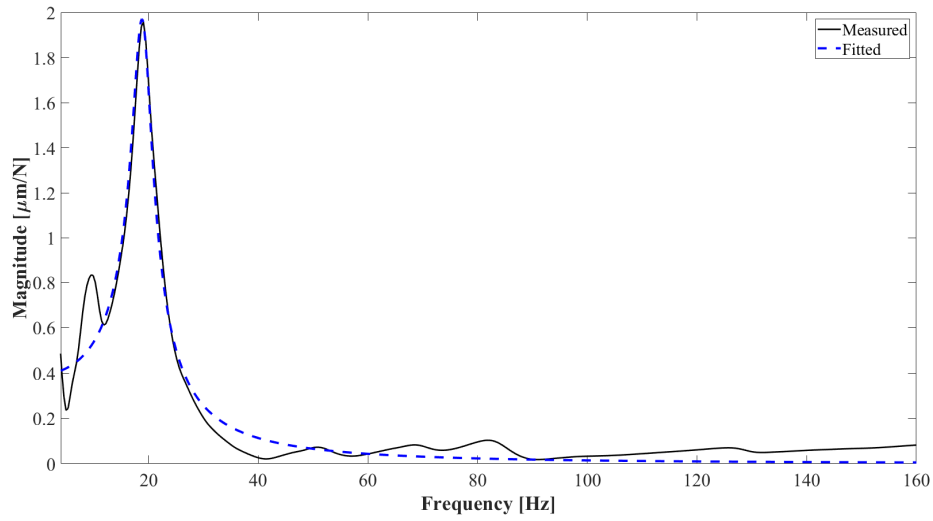


Figure 6. Measured robot end effector FRF (solid line) and its corresponding second order transfer function fit (dashed). The excitation and response were measured in the Cartesian X direction at the Cartesian XYZ (mm),  $R_x$ ,  $R_y$ , and  $R_z$  (degrees) position of [2100 mm, -300 mm, 325 mm,  $0^\circ$ ,  $0^\circ$ ,  $0^\circ$ ].

The procedure to extract the stiffness, damping coefficient, and natural frequency was repeated at multiple positions in the robot's workspace where the robot could physically reach the available workpiece mounting area. The tool axis was constrained to be perpendicular to the X-Y plane of the robot's base frame in all experiments. Modal impact hammer tests were replicated three times for a total of 60 unique configurations (12 XYZ points and 5 rotational orientations about the tool tip axis  $R_z$  at each point). The corresponding ranges of the robot joint angles are given in Table 1 and the modal parameters for each test replication are given in the Appendix (see Table A1).

Table 1. Ranges of tested locations. Cartesian units are in the robot base frame.

	Cartesian			Joint					
	$X$ [mm]	$Y$ [mm]	$R_z$ [deg]	$\theta_1$ [deg]	$\theta_2$ [deg]	$\theta_3$ [deg]	$\theta_4$ [deg]	$\theta_5$ [deg]	$\theta_6$ [deg]
Min	2100.0	-300.0	0.0	-27.7	-25.5	8.6	68.6	54.6	-74.5
Max	2700.0	600.0	180.0	19.9	6.6	114.5	287.1	110.0	74.8

### 3.2.2 Results

The results of the EMA tests in the X, Y, and Z directions are shown in Figure 7. Note that the average standard deviation of the natural frequency, stiffness, and damping coefficient measurements were 0.05 Hz, 0.04 MN/m, and 0.15 KNs/m. It is seen that the dominant natural frequency of the robot in the X direction increases as the arm moves further away from the robot base, with a drastic increase occurring when the arm is fully extended. The natural frequencies in the Y and Z directions are found to decrease as the arm is extended, although the change in natural frequency is not as dramatic as in the X direction. As the robot tool tip moves further away from the base, its stiffness in the X direction increases while the stiffness in the Y and Z directions decrease due to the cantilever beam effect produced when the arm is extended. The damping coefficient trends are more difficult to generalize, but the results show that damping tends to decrease in all directions as the robot moves further away from its base.

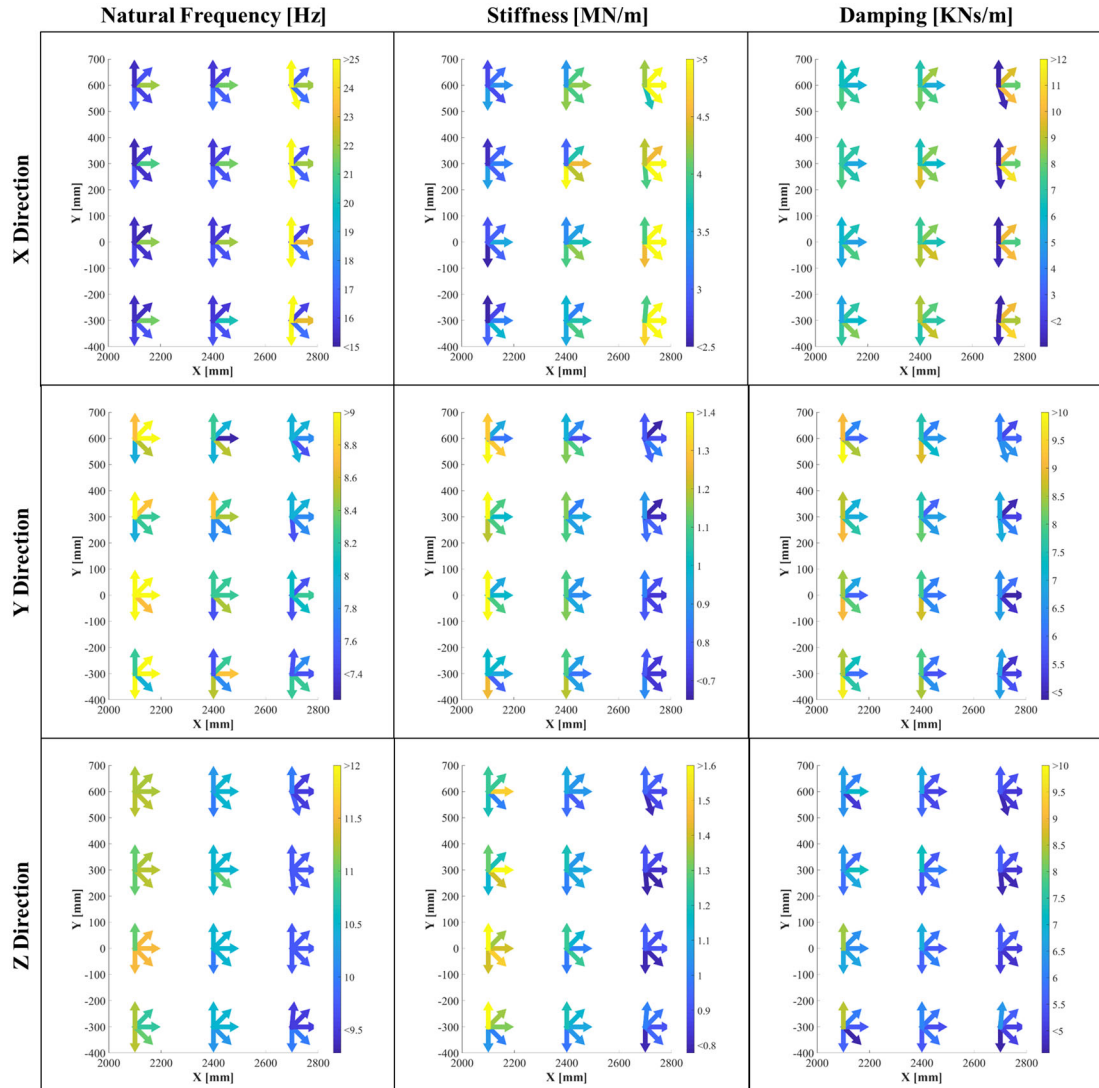


Figure 7. Results of the impact hammer tests. The X, Y, and Z notation refers to the modal parameter in those directions. The base of the arrow denotes the XYZ position where the tool tip was located. The arrows point in the direction normal to the robot flange and denote the rotation about the tool axis at the position. The coordinates are defined in the robot base frame.

### 3.3 Gaussian Process Regression Model

The measurements shown in Figure 7 were used to create the GPR model of the robot's dominant natural frequency, damping coefficient, and stiffness as a function of the end effector position. A brief overview of the model is provided, followed by validation results.

#### 3.3.1 Model Description

The natural frequency, stiffness, and damping coefficient of the dominant mode of robot vibration in each Cartesian direction for a given pose  $q$  can be expressed as a Gaussian Process with the following prior [61]

$$c(q) \sim GP(\mu(q), \mathbf{C}(q, q')) \quad (6)$$

where  $\mu(q)$  is a basis function and  $\mathbf{C}(q, q')$  is the covariance matrix [61]. Note that in this work,  $\mu(q)$  is a constant basis function and  $\mathbf{C}(q, q')$  consists of the squared exponential kernel function of the form

$$k(q_i, q_j) = \sigma_f^2 \exp\left(-\frac{(q_i - q_j)^T (q_i - q_j)}{2\sigma_l}\right) \quad (7)$$

where  $\sigma_l$  and  $\sigma_f$  are the characteristic length scale and signal standard deviation, respectively. In addition, treating an observation point  $y$  as a Gaussian Process results in the following prior for a prediction point  $q_*$

$$\begin{bmatrix} y \\ c_* \end{bmatrix} \sim N\left(\begin{bmatrix} \mu(q) \\ \mu(q_*) \end{bmatrix}, \begin{bmatrix} \mathbf{C}(q, q) + \sigma^2 I & \mathbf{C}(q, q_*) \\ \mathbf{C}(q_*, q) & \mathbf{C}(q_*, q_*) \end{bmatrix}\right) \quad (8)$$

where  $\sigma^2$  is the model variance. Thus, because a Gaussian Process prior is chosen, the predictive posterior distribution is traceable through Bayesian inference and its mean  $\bar{c}_*$  and covariance  $\eta_*$  are expressed as

$$\bar{c}_* = \mu(q_*) + \mathbf{C}(q_*, q)[\mathbf{C}(q, q) + \sigma^2 \mathbf{I}]^{-1}(y - \mu(q)) \quad (9)$$

$$\eta_* = \mathbf{C}(q_*, q_*) - \mathbf{C}(q_*, q)[\mathbf{C}(q, q) + \sigma^2 \mathbf{I}]^{-1}\mathbf{C}(q, q_*) \quad (10)$$

### 3.3.2 Validation

After fitting the GPR model using the modal impact hammer test data, two types of model validations, namely cross validation and external validation, were conducted. Cross validation consists of comparing the model against all but one of the data points while external validation consists of comparing the model predictions with a test dataset not utilized in building the model.

A 5-fold cross validation, where the entire dataset was partitioned into 5 equal sub-sets and a single sample sub-set is used as the test dataset while the remaining are used for model fitting, was performed for each of the modal parameters. Figure 8 shows the residual plots obtained from the cross validation process. It can be seen that the residuals are uncorrelated, indicating that the model captures the main trends in the data well. The correlation coefficients and the root mean squared errors (RMSE) of the cross validation exercise are listed in Table 2. Note that damping coefficient was found to have the lowest correlation coefficient due to its low correlation with position compared to natural frequency and stiffness. In addition, the residual plots show that the error appropriately scales with the range of values. Hence, since the X Direction exhibits the largest ranges for natural frequency, stiffness, and damping coefficient, the RMSE values are shown to be the largest out of the three Cartesian directions. However, the cross validation is shown to

be sufficient for predicting the modal parameters as a function of the robot position. In addition, a 2<sup>nd</sup> order Multivariate Linear Regression (MLR) model was calibrated with the robot arm configuration to predict the modal parameters for comparison with the GPR model. The correlation coefficient and RMSE values of the MLR model are shown in Table 2. The MLR model was found to have consistently lower correlation coefficients and higher RMSE values than the GPR model. Hence, the GPR model is shown to be a more suitable model to predict the modal parameters without the need to specify model order.

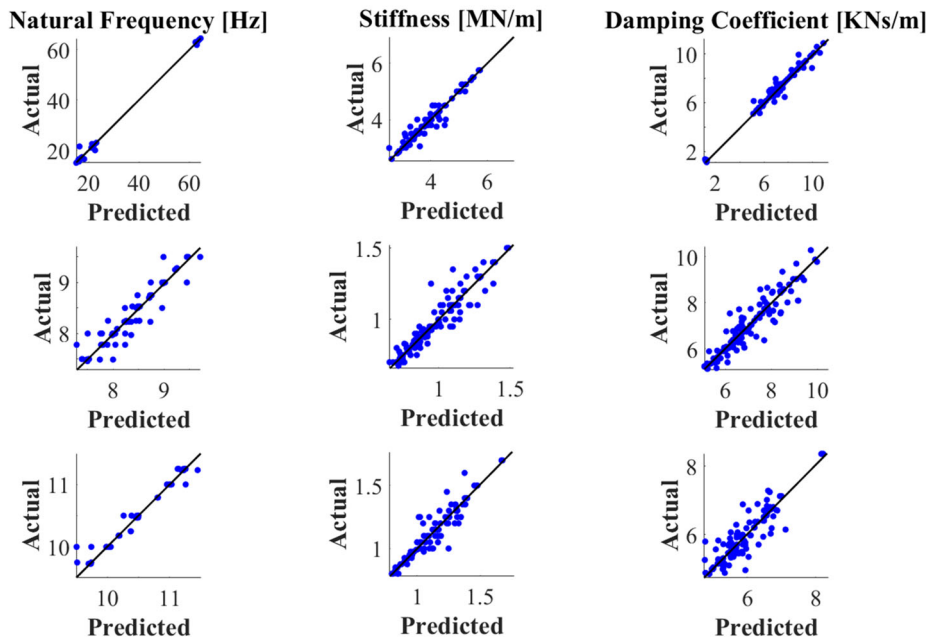


Figure 8. Cross validation residual plots.

Table 2. Correlation coefficient and Root Mean Square Error (RMSE) values from cross validation.

		X			Y			Z		
		Natural Freq. [Hz]	Stiffness [MN/m]	Damping [KNs/m]	Natural Freq. [Hz]	Stiffness [MN/m]	Damping [KNs/m]	Natural Freq. [Hz]	Stiffness [MN/m]	Damping [KNs/m]
GPR	$R^2$	0.96	0.97	0.90	0.92	0.92	0.90	0.98	0.92	0.88
	RMSE	3.31	0.15	0.81	0.16	0.06	0.42	0.09	0.06	0.29
MLR	$R^2$	0.47	0.79	0.25	0.59	0.80	0.87	0.92	0.80	0.66
	RMSE	11.91	0.44	2.34	0.38	0.10	0.48	0.19	0.11	0.49

For external validation, the GPR model was used to predict the modal parameters extracted from 30 points (6 XYZ points with 5 rotational orientations about the cutting tool axis at each point) in the workspace not considered during model building. The external validation evaluates the GPR model's capability of predicting the response at different XYZ points. The results of the validation experiments are shown in Figure 9 and the raw measurements are shown in Table A. 2. It is seen that larger differences between the model predictions and measured values are obtained when the robot tool tip is further from its base while the smallest differences are observed when the robot tool tip is closest to its base. This is because the measurements at the points used to build the GPR model (Figure 7) follow smooth, linear trends. Therefore, the linear basis functions utilized in the GPR model are less accurate at these positions. Because the GPR model is a probabilistic model, variance estimates associated with potential predictions can be determined. Hence, using the GPR model, points of high uncertainty can be identified, and additional measurement points can be performed at such points. The additional measurements can then be used to augment the GPR model, which then would reduce the uncertainty prediction at points of high variance.

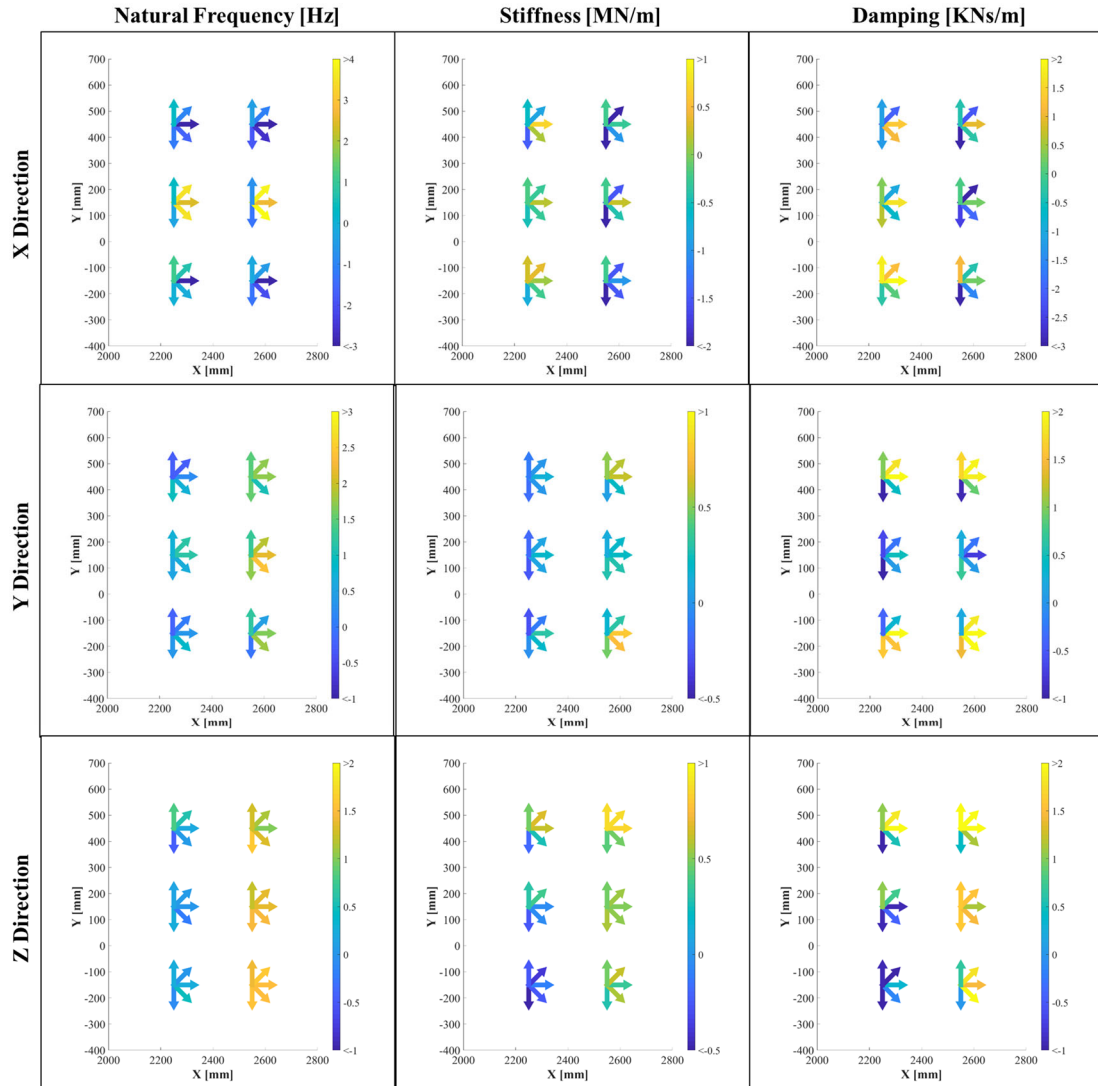


Figure 9. Relative errors between the measured and predicted values of the modal parameters in external validation tests.

### 3.4 Comparison of Analytical Model with Experiments

The measured modal parameter values were compared with those derived from a Jacobian-based analytical model to determine possible locations in the workspace where the analytical model is not sufficiently accurate. Specifically, the Cartesian stiffness and mass matrices were calculated analytically from a joint stiffness and inertia model,

respectively, and the undamped natural frequency was calculated by solving the eigenvalue problem resulting from the system of second order differential equations of motion obtained using the Cartesian stiffness and mass matrices of the robot arm.

### 3.4.1 Analytical Cartesian Stiffness and Inertia Models

The Cartesian stiffness was obtained from a joint stiffness model, which assumes negligible compliance of the robot links compared to the joints. The methodology used to obtain the joint stiffness can be found in [62]. As specified in [62], Cartesian stiffness matrix  $\mathbf{K}(q)$  of the robot can be calculated as

$$\mathbf{K}(q) = \mathbf{J}(\theta)^{-T}(\mathbf{K}_\theta - \mathbf{K}_c)\mathbf{J}(\theta)^{-1} \quad (11)$$

where  $\mathbf{J}(\theta)$  is the robot Jacobian matrix,  $\mathbf{K}_\theta$  is the diagonal matrix of joint stiffnesses, and  $\mathbf{K}_c$  is the complementary stiffness matrix. Note that [62] showed that  $\mathbf{K}_c$  is significant in regions near a singularity. Since the robot poses utilized in this work were not close to singularities, the effect of  $\mathbf{K}_c$  is assumed to be minimal. Hence,  $\mathbf{K}(q)$  is position dependent while  $\mathbf{K}_\theta$  is assumed to be independent of position. The joint stiffness values  $\mathbf{K}_\theta$  were established through static compliance experiments. Specifically, for an applied wrench  $\mathbf{v}$  at a given robot configuration, the Cartesian deflections can be expressed as

$$\Delta = \mathbf{J}(\theta)\mathbf{K}_\theta^{-1}\mathbf{J}(\theta)^T\mathbf{v} \quad (12)$$

By measuring  $\Delta$  for known  $\mathbf{J}(\theta)$  and  $\mathbf{v}$ ,  $\mathbf{K}_\theta$  can be calculated for a robot configuration [62]. To apply a load, a six degree of freedom wrench using gravitational loading was applied to the robot end effector to induce a screw displacement as shown schematically in Figure 10.

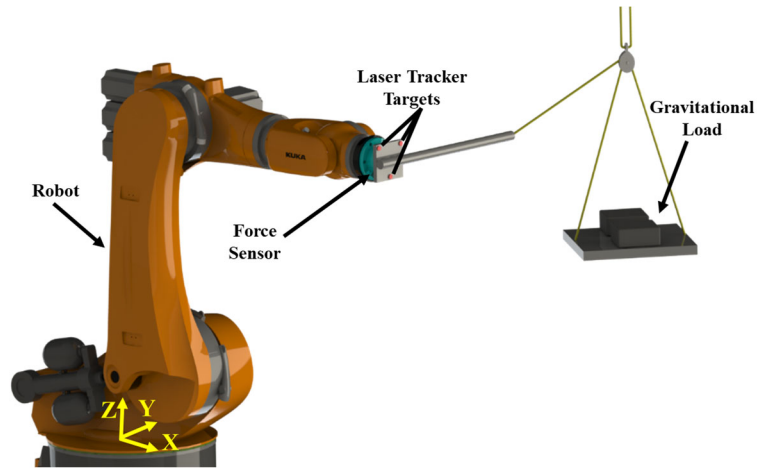


Figure 10. Schematic of the static compliance experiments.

Note that, aside from the mass of the end effector, no preload was applied in these experiments. The wrenches were measured using a flange mounted six-axis force/torque sensor (ATI Omega 160). The screw displacements were measured using a FARO Ion laser tracker, which measured three individual targets before and after the external wrench was applied. Note that the joint brakes were disengaged, and the robot controller was active throughout the compliance experiments. To account for measurement variations, ten experiments were performed at the locations specified in Table 3. The robot configurations were chosen such that significant torques could be applied to all of the robot joints.

Table 3. Test robot joint angles for compliance experiments (degrees)

Test No.	$\theta_1$	$\theta_2$	$\theta_3$	$\theta_4$	$\theta_5$	$\theta_6$
1	19.67	-52.14	117.9	11.86	-66.08	-4.84
2	26.35	-32.54	123.49	-8.99	-90.81	-0.15
3	58.28	-10.5	105.98	42.39	-115.04	-2.57
4	44.71	-70.81	58.16	138.51	-41.63	-125.84
5	-23.13	-85.41	80.84	70.31	83.63	-71.78
6	2.39	-34.82	69.97	115.13	72.1	176.98
7	25.21	-55.7	130.03	169.88	72.17	-179.78
8	42.99	-40.39	97.42	-177.38	72.1	-179.8
9	42.99	-57.91	110.04	-155.79	51.1	-179.83
10	28.12	-55.4	84.06	-167.6	27.07	-179.85

Note that when calculating  $\mathbf{K}_\theta$  for multiple robot configurations, Equation (12) is overdetermined. Thus, a nonlinear least squares approach was used to minimize the Euclidean norm of the difference between the measured and predicted joint stiffness values. Singular regions, where some joints may experience close to zero torque, were avoided. The resulting joint stiffness values are given in Table 4. Note that the analytical stiffness model in this thesis assumes that nonlinearities in the joints such as hysteresis and backlash are negligible. For instance, prior work has shown that the nonlinearity owing to hysteresis results in a max torsional angle deflection error of  $0.005^\circ$  for  $\theta_1$  [63].

Table 4. Measured joint stiffness values ( $\times 10^6$  Nm/rad)

$K_{\theta_1}$	$K_{\theta_2}$	$K_{\theta_3}$	$K_{\theta_4}$	$K_{\theta_5}$	$K_{\theta_6}$
3.93	3.46	2.77	1.57	0.24	0.17

Note that the values in Table 4 are consistent with the joint stiffness trends reported in [62]. Specifically,  $K_{\theta_1}$  is the joint with the lowest compliance while  $K_{\theta_4}$ ,  $K_{\theta_5}$ , and  $K_{\theta_6}$  are the most compliant joints. To determine the system natural frequency, the Cartesian mass

matrix of the robot must be determined. The effective Cartesian mass matrix  $\mathbf{M}(q)$  is related to the robot's rotational inertia matrix  $\mathbf{I}_i$  as follows

$$\mathbf{M}(q) = \sum \mathbf{J}_i(\theta)^T \mathbf{I}_i \mathbf{J}_i(\theta) \quad (13)$$

where

$$\mathbf{I}_i = \int \begin{bmatrix} (y - y_c)^2 + (z - z_c)^2 & -(x - x_c)(y - y_c) & -(z - z_c)(x - x_c) \\ -(x - x_c)(y - y_c) & (z - z_c)^2 + (x - x_c)^2 & -(y - y_c)(z - z_c) \\ -(z - z_c)(x - x_c) & -(y - y_c)(z - z_c) & (x - x_c)^2 + (y - y_c)^2 \end{bmatrix} \rho dV \quad (14)$$

$\mathbf{J}_i(\theta)$  is the Jacobian of link  $i$ ,  $\rho$  is the mass density,  $x_c$ ,  $y_c$ , and  $z_c$  are the coordinates of the centroid of link  $i$ , and  $dV$  is the infinitesimal volume element. Note that the internal density of the arm cannot be determined without proprietary knowledge of the robot construction. Because of the lack of knowledge of the internal construction of the links (i.e. the possibility of the links being hollow or housing a pulley system), the links were assumed to be solid and their mass uniformly distributed. The free vibration response of the robot system after neglecting damping can be determined from the solution of the following system of equations

$$\mathbf{M}(q)\ddot{\Delta} + \mathbf{K}(q)\Delta = 0 \quad (15)$$

whose general solution is of the form

$$\Delta(t) = \mathbf{U}e^{i\lambda t} \quad (16)$$

The undamped natural frequencies of the system are obtained from the square root of  $\lambda$  [64]. While the analytical derivation considers rotational modes about the end effector,

in this work the rotational modes are assumed to have minimal effect on the robot tool tip vibration and therefore only the translational modes are considered.

### *3.4.2 Comparison with Measured Modal Parameter Values*

Figure 11 shows the comparison of the analytically derived modal parameter values (natural frequency, stiffness) with the measured values derived from the experiments reported earlier. Note that since the GPR model interpolates between the experimental points, comparison of the analytical model with the GPR model at the measured points is redundant. As the arm extends further away from the base, the differences in the analytically predicted and measured stiffness values grow. The analytical approach tends to overestimate the stiffness primarily due to the assumption of infinitely stiff links. While the assumption may hold under static loading conditions, the flexibility of each link must be considered for dynamic loading situations. However, even when flexibility of the links is considered, the analytical model is still expected to overestimate the stiffness because the links are usually stiffer than the joints. Generally, the analytical model is found to underestimate the dominant natural frequency of the robot. This is because the analytical model overestimates the mass in addition to overestimating the stiffness due to modelling errors associated with determination of the link inertias. However, note that even though the analytical model exhibits modelling errors, it can still be used to identify regions of the robot's workspace, especially its joint configuration space, that need to be sampled to develop the data-driven model. For instance, the analytical model can be used to identify symmetric behavior in the modal parameters and locations of high variance.

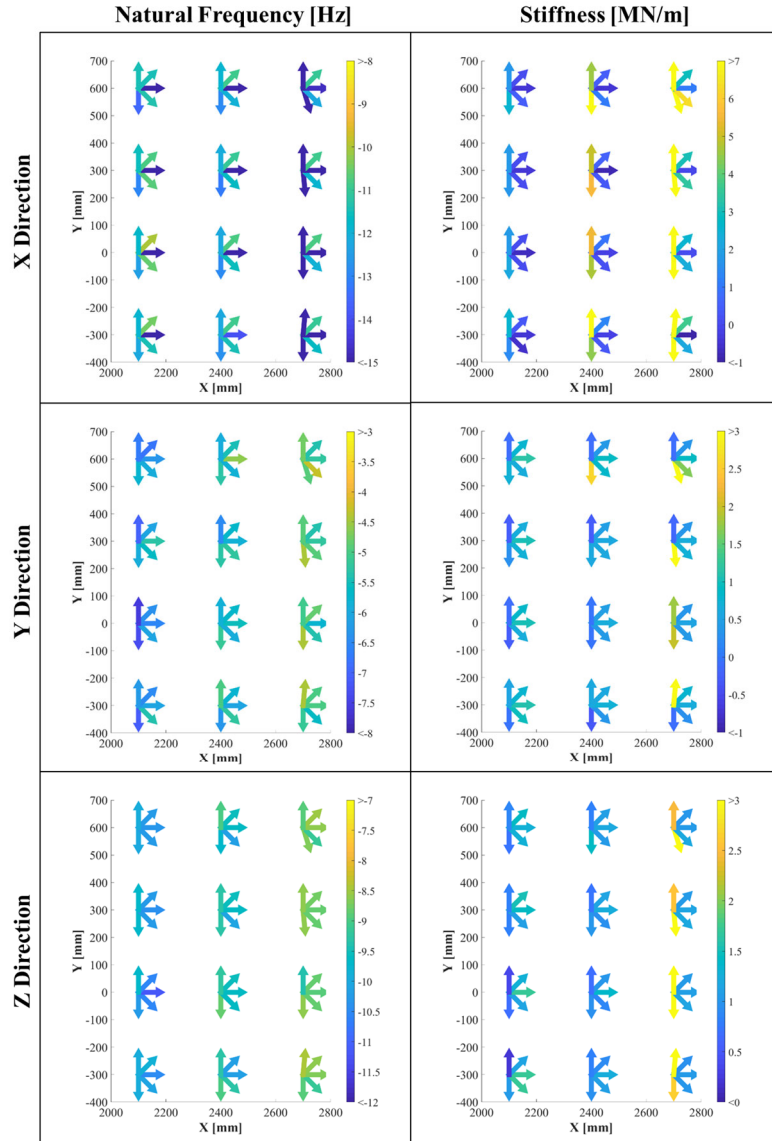


Figure 11. Relative errors in the natural frequency and stiffness between the analytical model and impact hammer measurements.

### 3.5 Prediction of Tool Tip Vibrations

This section describes the use of the GPR model to predict the natural frequency, stiffness, and damping coefficient at two specific robot Cartesian positions and to utilize them in predicting the tool tip vibrations produced during robotic milling at the two

positions. This section describes the robotic milling experimental setup and methodology for calculating the average peak-to-valley tool tip vibrations followed by results and discussion.

### *3.5.1 Experimental Setup*

The two robot positions shown in Figure 12 were selected for evaluating the performance of the GPR model when used to predict the robot tool tip vibrations produced during milling. The two positions were chosen to highlight the differences in the vibration responses of the robot with changing robot tool tip position. Note that the modal stiffness in the X direction of Position 2 is higher than the modal stiffness in the Y direction of Position 1. Thus, Position 2 would normally be preferred to minimize the surface errors in the wall direction (X) of the machined slot due to robot deflection. However, because the dominant resonant frequency of the robot tool tip suddenly transitions to approximately 62 Hz in the X direction around Position 2, an excitation force close to the resonant frequency can in fact generate larger vibrations and therefore larger surface error in the slot wall direction. Thus, the cutting conditions were chosen to highlight the capability of the GPR model, which can accurately capture the sudden transition in the robot's natural frequency.

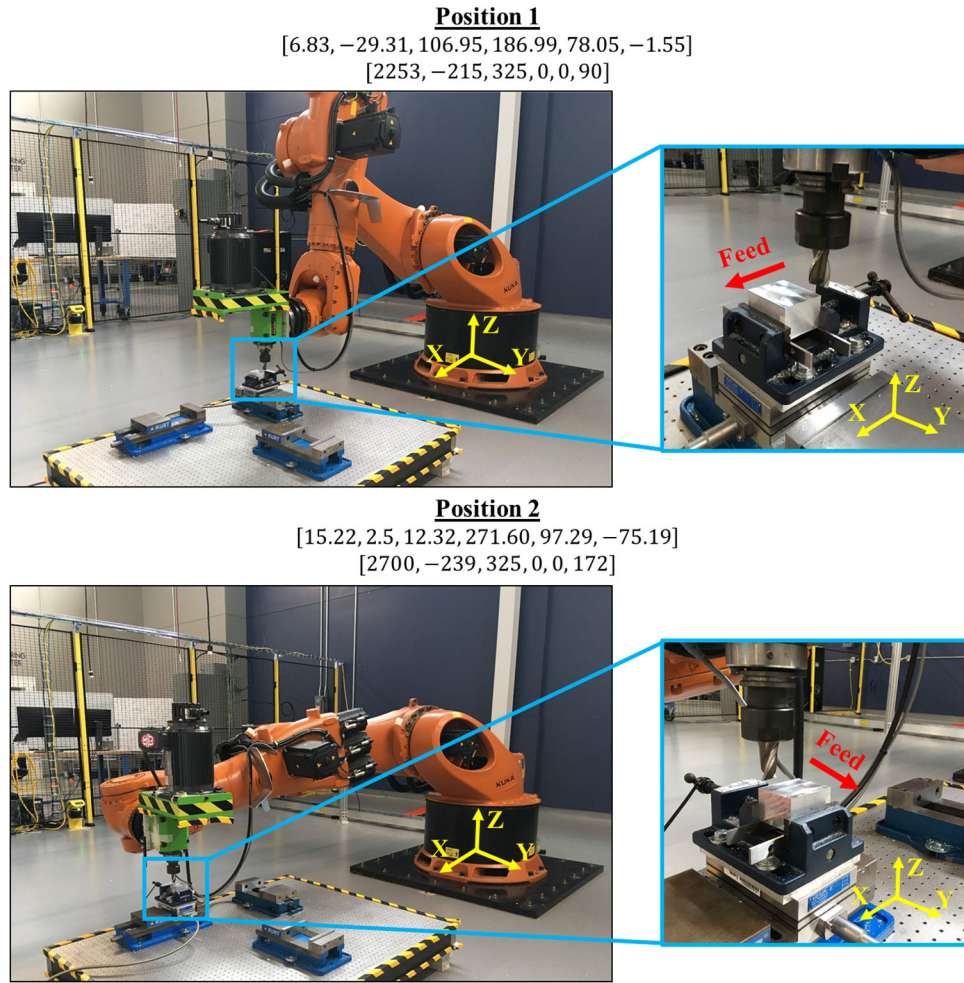


Figure 12. Robot poses and corresponding (top) joint angles (degrees) and (bottom) Cartesian XYZ (mm),  $R_x$ ,  $R_y$ , and  $R_z$  (degrees) used in the milling experiments.

Slot end milling cuts were made to generate the slot wall surface and floor surface features. Note that the wall features for Position 1 and Position 2 are in the Y and X directions, respectively. A two flute, 25.4 mm diameter, 30° helix angle, cobalt tool was used to machine Aluminum 7075-T7351 without coolant. The machining process parameters were selected to induce significant deflections at the robot tool tip. Specifically, the axial depth of cut was 3 mm while the feed per tooth was 0.058 mm and the spindle speed was 1750 RPM, which corresponds to a spindle rotation frequency of 29.16 Hz and

a tooth passing frequency of 58.3 Hz. The machining forces were measured using a three-component piezoelectric force transducer (Kistler 9257B) fixed to the optical breadboard while the robot instantaneous positions during milling were measured by the FARO Ion laser tracker from which the instantaneous robot tool tip deflections were determined. The cutting tests were replicated three times under the same cutting condition.

### 3.5.2 Prediction of Robot Tool Tip Vibrations during Milling

To predict the robot tool tip vibrations during milling, the generalized system model shown in Figure 13 was utilized. In general, the robotic milling system consists of the dynamic models of the cutting tool, the robot, and their corresponding fixturing systems. In this work, the flexibility of the robot arm-tool assembly was considered to dominate the system vibrations.

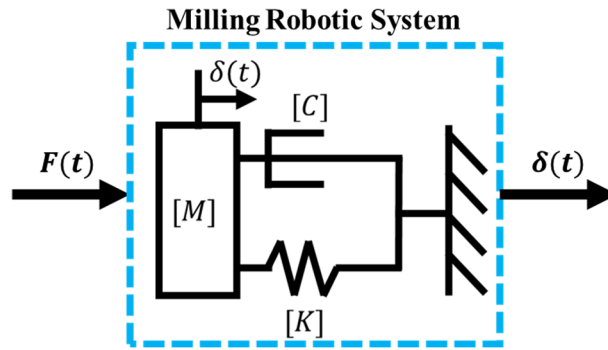


Figure 13. Simplified structural dynamics model of the robotic milling system.

Therefore, the system equations of motion are given by

$$\mathbf{M}(q)\ddot{\boldsymbol{\delta}} + \mathbf{C}(q)\dot{\boldsymbol{\delta}} + \mathbf{K}(q)\boldsymbol{\delta} = \mathbf{F} \quad (17)$$

where  $\mathbf{M}(q)$ ,  $\mathbf{C}(q)$ ,  $\mathbf{K}(q)$ ,  $\mathbf{F}$ , and  $\delta$  are the system mass matrix, damping coefficient matrix, stiffness matrix, milling force vector, and tool tip displacement vector, respectively.  $\mathbf{C}(q)$  and  $\mathbf{K}(q)$  were obtained from the GPR model while  $\mathbf{M}(q)$  was computed from the natural frequencies and stiffnesses derived from the GPR model [64]. Note that the theoretical milling forces are periodic and are characterized by a dominant tooth passing frequency [65]. However, Figure 14 shows the frequency decomposition of the measured milling forces from the experiments, which shows the milling force has other frequencies in addition to the tooth passing frequency and its harmonics. The milling forces will induce robot tool tip vibrations that modify the instantaneous chip thickness, and therefore the cutting forces [5]. For instance, Figure 14a) and c) show 8 Hz and 10.5 Hz peaks, respectively, in their force frequency decompositions even though the spindle and tooth passing frequencies are 29.16 Hz and 58.3 Hz. Thus, the frequency decomposition shown in Figure 14 has both tooth passing harmonics and the robot's vibratory modes. Therefore, to predict the robot tool tip vibrations, the measured forces were used in Equation (17), which was solved using the convolution theorem [66].

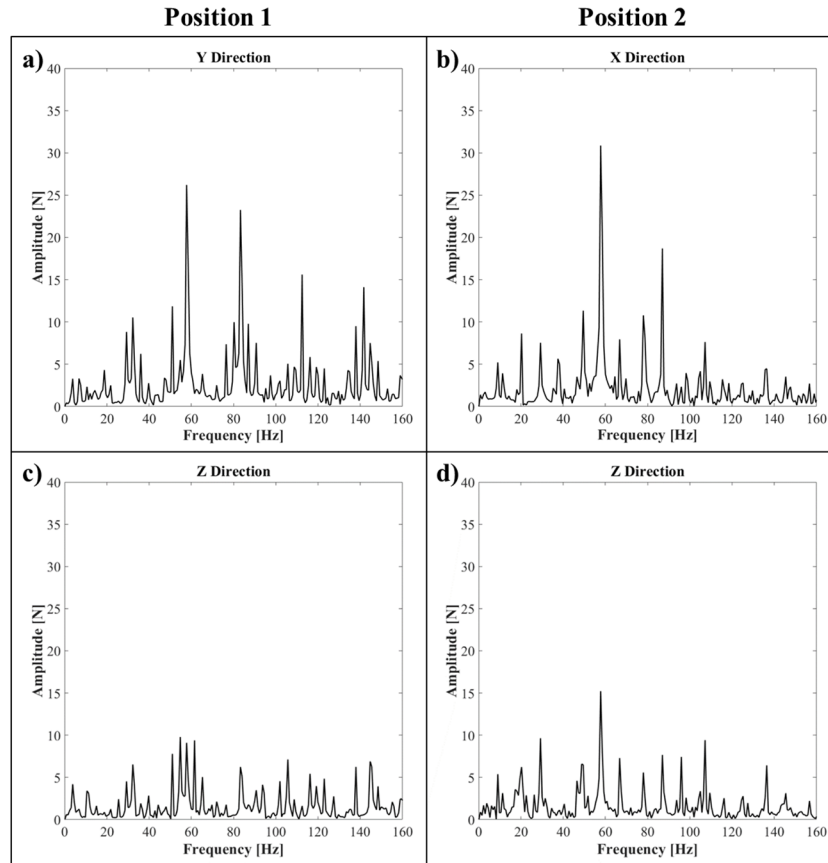


Figure 14. Frequency decomposition of the measured milling forces.

Figure 15 shows the measured FRFs and the GPR predictions for the two robot positions. Note that the measured FRFs shown in the figure are representative since three measurements were made at each robot position. The robot's dominant mode in Position 1 is more compliant in the Y direction (Figure 15a) compared to the X direction at Position 2 (Figure 15b). In addition, Figure 15b shows that while the 9 Hz mode does indeed become less compliant when transitioning to Position 2, the 62 Hz mode becomes larger and therefore is the most dominant mode, which is captured by the GPR model. In addition, the Z direction in Position 1 (Figure 15c) is less compliant than the Z direction in Position 2 (Figure 15d) because the robot behaves more like a cantilever beam in the Z direction at

Position 2. Note that the compliances and dominant modes in the Y and Z directions at Position 1 are similar, which can contribute to the mode-coupling effect [33]. Therefore, another potential application of the GPR model is prediction of chatter conditions in robotic milling.

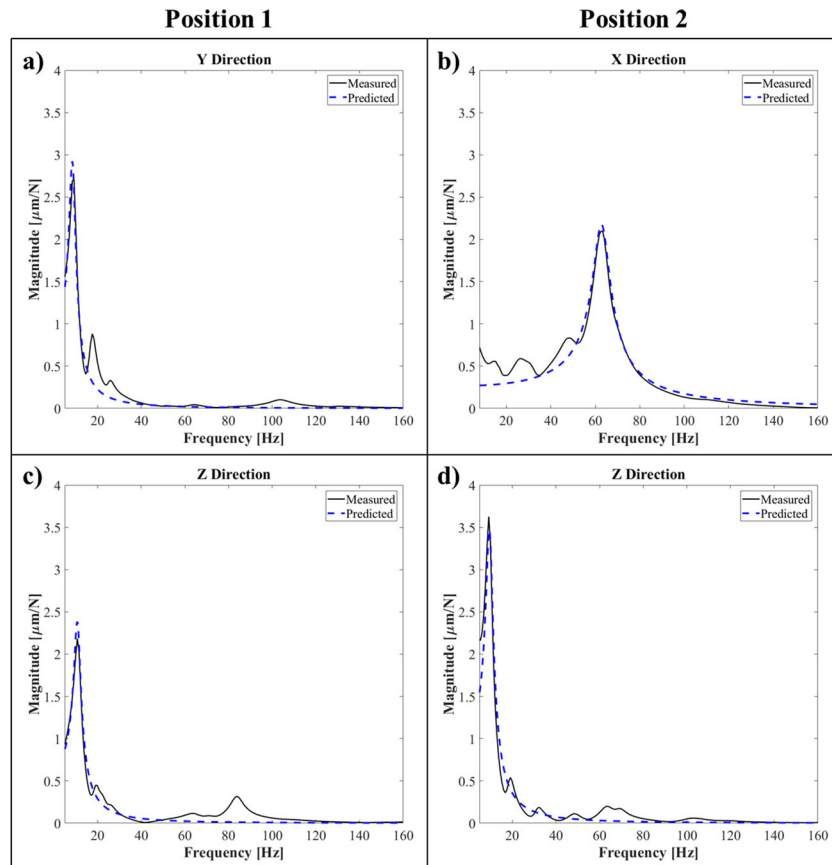


Figure 15. Measured and predicted FRFs for the two robot positions.

### 3.5.3 Results

Representative instantaneous robot tool tip deflections determined from the laser tracker data are shown in Figure 16 while Figure 17 shows the comparison of the measured and predicted average peak-to-valley vibration amplitudes derived from the measured force amplitudes taken every spindle revolution (34 ms). The milling forces produce a mean

deflection and associated vibrations of the robot tool tip, which is evident in Figure 16. Note that the mean deflections in the slot wall direction (Y) at Position 1 (Figure 16a) and the slot wall direction (X) at Position 2 (Figure 16b) are 0.14 mm and 0.083 mm, respectively. Therefore, the mean deflection in the slot wall direction at Position 1 is greater than at Position 2. However, the corresponding average peak-to-valley vibrations (Figure 17) at Position 1 and Position 2 are 0.083 mm and 0.506 mm, respectively. Therefore, Position 2 exhibits greater vibration amplitudes and will therefore contribute to a larger surface error in the slot wall direction. Figure 17 shows that the GPR model's average peak-to-valley vibrations at Position 1 and Position 2 are well correlated with the laser tracker measurements. The mean deflections in the slot floor surface (Z) direction at Position 1 and Position 2 are 0.075 mm and 0.182 mm, respectively, while the average peak-to-valley vibrations in the Z direction are 0.064 mm and 0.125 mm, respectively. As shown in Figure 15c and Figure 15d, the robot arm extension does not significantly change the dominant natural frequency although the compliance increases. Therefore, both the mean deflections and the peak-to-valley vibrations generated by milling increase from Position 1 to Position 2.

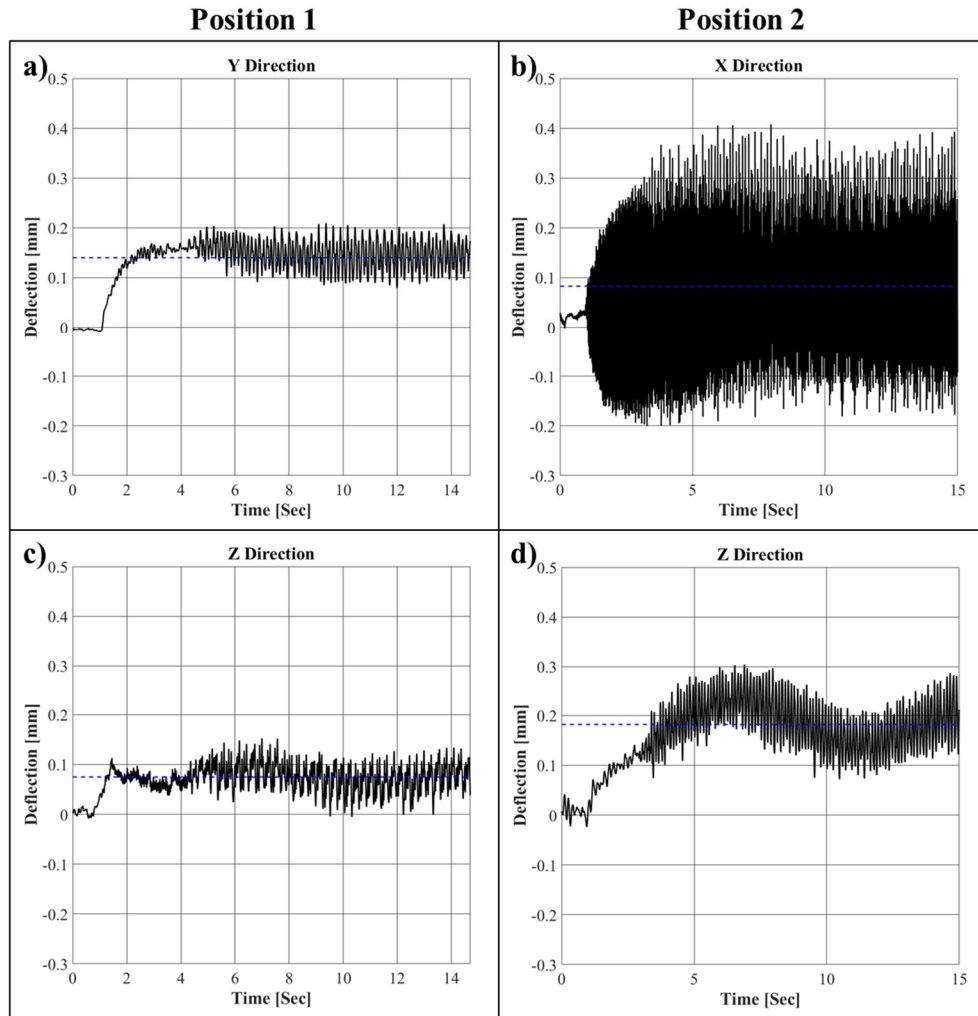


Figure 16. Representative tool tip deflections during robotic milling experiments. The blue dashed line indicates the mean values.

The GPR model is shown to follow similar trends as the measured average peak-to-valley vibrations (Figure 17). The largest error between the predicted and measured values is 0.028 mm in the X direction at Position 2 (Figure 17b), which experienced the largest vibrations. However, the smallest error is 0.006 mm in the Z direction at Position 1 (Figure 17a), which corresponds to the test with the smallest vibrations. Note that the laser tracker measurement resolution is 0.01 mm, and therefore the observed differences

between the predicted and measured peak-to-valley vibrations in the Z direction could be the result of tracker measurement error. In addition, the GPR appears to slightly underpredict the average peak-to-valley vibrations. The underprediction is most likely due to the inclusion of only a single vibration mode in the GPR model while the robot FRF has multiple modes that can contribute to the tool tip vibration. To account for this discrepancy, a more accurate model must consider the complete FRF at each point within the robot's workspace. However, predicting the entire FRF digitally (as opposed to coefficients of a second order system as reported in this work) requires a significantly larger number of predictor variables, which adds to the complexity of the model and the corresponding calculation time. Future work will investigate more efficient interpolation methods that permit the inclusion of the entire FRF as a function of robot position in the workspace.

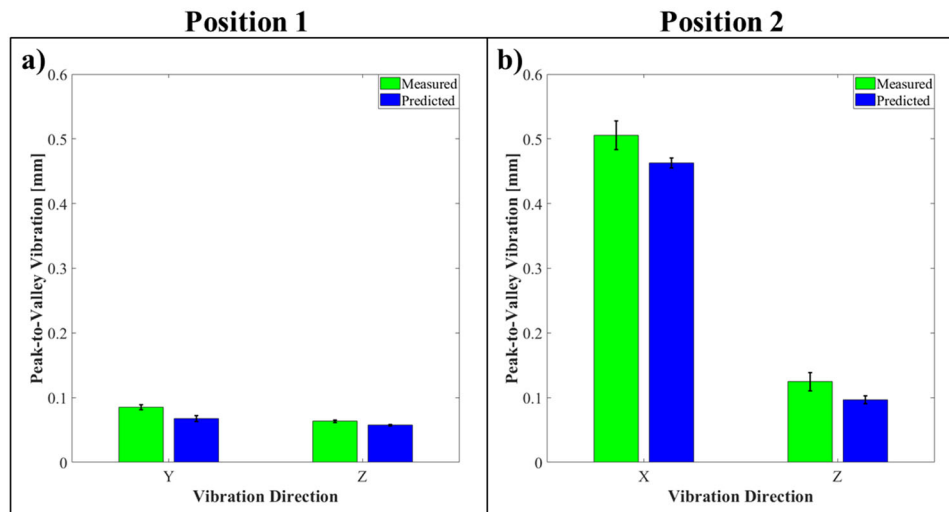


Figure 17. Comparison of predicted and measured average peak-to-valley tool tip vibration amplitudes.

### 3.6 Summary

A Gaussian Process Regression (GPR) based statistical modeling approach was used to determine the dynamic parameters of a 6-dof industrial robot over a finite workspace defined by the available workpiece mounting area. The GPR model allows the modal frequency, stiffness, and damping coefficient to be determined at different points in the robot's workspace. The EMA experiments showed that as the robot arm is extended from its base, the modal stiffness and natural frequency increased in the direction of arm extension whereas they decreased in the plane perpendicular to the direction of arm extension. The GPR model was found to accurately model the robot's dominant natural frequency, stiffness, and damping coefficient in its measurement space with maximum root mean square errors of 3.31 Hz, 150 KN/m, and 810 Ns/m, respectively, and was shown to be more accurate than a Multivariate Linear Regression model. However, it was found that the GPR model requires more sampling points in locations where the robot dynamics varies significantly, such as when the end effector is furthest from the robot base. The experimental modal analysis results were also compared with the modal parameters determined from the solution of a Jacobian based analytical model of the robot tool tip dynamics. This comparison has shown that the undamped natural frequency and stiffness of the robot obtained from the analytical model deviate significantly from the experimental values as the robot arm is extended further from its base. Hence, the data-driven modelling approach in this work shows the regions where the existing analytical model fails and would have to be improved. The modal parameters obtained from the GPR model were used to calculate the average peak-to-valley vibrations of the robot tool tip during robotic milling, which were compared with laser tracker measurements. The results have shown

that the average peak-to-valley vibrations predicted by the model followed the experimental trends. Hence, the data-driven modelling approach based on Gaussian Process Regression enables accurate prediction of tool tip vibrations in milling applications with a max error of 0.028 mm. Thus, the improvement in prediction accuracy demonstrated in this work further improves the feasibility of utilizing industrial robots in milling applications.

## **CHAPTER 4. POSE-DEPENDENT OPTIMAL CONTROL OF VIBRATIONS IN ROBOTIC MILLING**

### **4.1 Introduction**

The review of prior literature shows that an on-line feedback methodology that accounts for the pose-dependence of the modal properties of CNC machines nor industrial robots has not been investigated. Because the vibration characteristics of the robot tool tip vary with robot pose, the feedback controller gains used for disturbance rejection must change within the robot's work volume to account for changes in the robot's vibration characteristics with arm configuration. However, using empirically tuned feedback controllers would require manual tuning of the controller gains throughout the robot workspace. Therefore, to efficiently implement vibration suppression in robotic milling, a pose-dependent optimal controller that uses a system model of the robot's tool tip dynamics is required. The chapter presents a pose-dependent optimal controller based on the previous GPR statistical model of 6-dof industrial robot's pose-dependent modal properties for vibration suppression in milling applications. First, modal analysis of the robot's dominant modal vibration parameters for the pose-dependent optimal controller is described. The measured modal responses are utilized for building a GPR model that predicts the modal parameters (natural frequency, stiffness, and damping ratio) as a function of arm configuration. The optimal control strategy, which utilizes the GPR model, is then described. The controller performance is then evaluated through offset mass and robotic milling experiments.

## 4.2 Data-Driven Model Calibration Experiments

### 4.2.1 Experimental Setup

The modal parameter characterization procedure described in Chapter 3 was utilized at discrete points along a linear tool path in the  $-Y$  direction of the robot base frame, as shown in Figure 18. The modal parameters in the  $X$ ,  $Y$ , and  $Z$  directions at each discrete point were then calculated using the procedure discussed in Chapter 3. The length of the linear tool path was 1.235 m and the points were spaced 0.056 m apart yielding 20 sampled robot configurations, which resulted in 60 FRFs. The corresponding robot joint angles are listed in Table 1. While the example robot path considered in this chapter is a straight line aligned with a coordinate axis, the methodology is general and can be applied to more complex tool paths in the robot's workspace, as shown in Chapter 3.

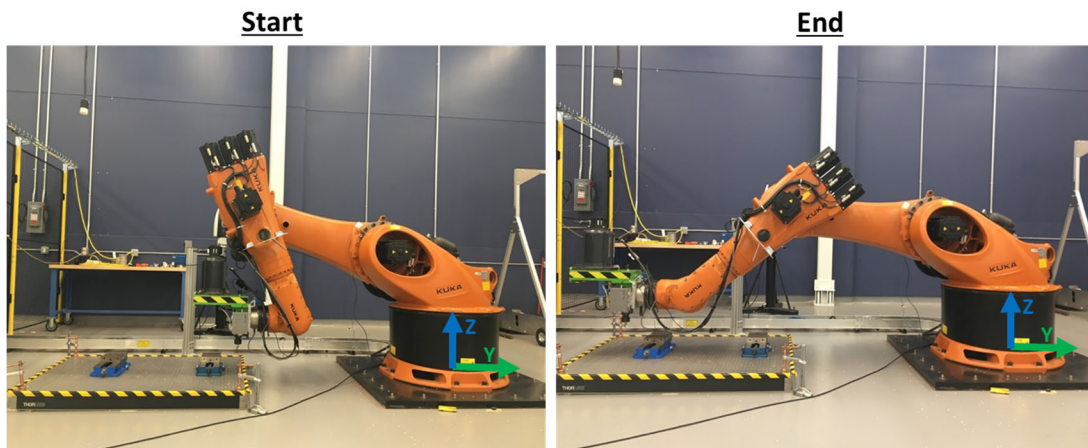


Figure 18. Start and end points for impact hammer experiments. The coordinate system in this illustration is fixed to the robot base frame.

Table 5. Joint angles for the start and end points of the linear robot path utilized in the impact hammer experiments. Units are in degrees.

Position	$\theta_1$	$\theta_2$	$\theta_3$	$\theta_4$	$\theta_5$	$\theta_6$
Start	87.97	-15.92	128.27	178.95	113.06	-1.15
End	88.88	-5.85	45.63	179.95	40.647	-0.69

#### 4.2.2 Modal Analysis Results

The results of the EMA tests in the X, Y, and Z directions are shown in Figure 19. The robot's modal stiffness values in the X and Z directions decrease as the arm is extended. This is because the arm behaves as a cantilever beam when the arm is extended, which increases the compliance. This is accompanied by a gradual decrease in the corresponding natural frequencies. Note that the modal stiffness in the Y direction gradually increases with arm extension because the axial stiffness of the arm is higher in the stretched configuration. Interestingly, the damping ratio exhibits significant non-linearity in the X and Z directions with respect to extension length as the robot arm is extended. Note that the mass and stiffness are known to have a nonlinear relationship with arm configuration and the damping ratio has been shown to be proportional to mass and stiffness [38]. Therefore, the damping ratio's behavior with arm extension is expected to be nonlinear. In addition, because the modal parameters exhibit functional behaviors that cannot be encompassed by a known a-priori parametric function, a non-parametric data-driven model must be used to predict the modal parameters within the robot's workspace.

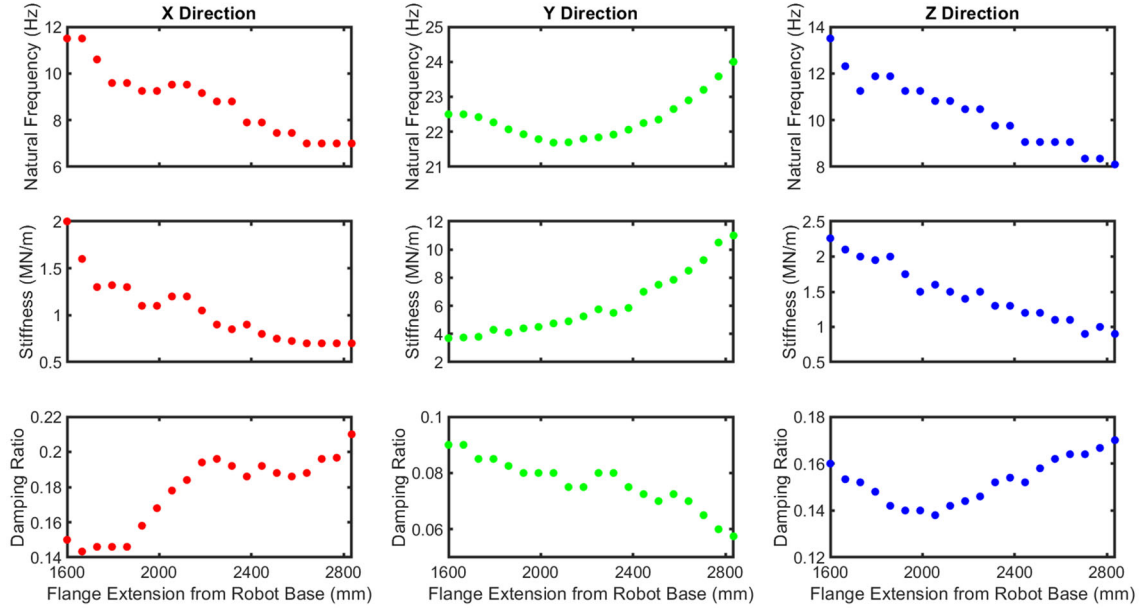


Figure 19. Modal parameter trends estimated from impact hammer tests.

#### 4.2.3 GPR Model Cross Validation Results

The modelling approach based on Gaussian Process Regression (GPR) presented in Chapter 3 was used to model the variation in the robot's modal stiffness, undamped natural frequency, and damping ratio along the tool path in the X, Y, and Z directions with the corresponding robot pose as model input. To validate the GPR models obtained for each Cartesian direction, a 5-fold cross validation was performed after training the models with the data shown in Figure 19. In this validation method, the entire dataset was randomly partitioned into five equal sub-sets with four sub-sets used to fit the model, which was then used to predict the remaining sample sub-set. The training and prediction methods were applied to all sub-sets. This validation procedure was applied to the modal parameters in each of the Cartesian directions. The correlation coefficients  $R^2$  and the root mean squared errors (RMSE) of the cross validations were calculated and are reported in Table 6. The

results show that all correlation coefficients are above 0.90, implying that the model prediction errors are normally distributed and the model is able to capture the main trends in the data. In addition, the models' RMSE are small compared to the range of values shown in Figure 19, with the largest RMSE percentage of 8% for the X direction modal stiffness.

Table 6. Correlation coefficients and *RMSE* values from cross validation.

	X			Y			Z		
	Natural Freq. [Hz]	Stiffness [MN/m]	Damping Ratio	Natural Freq. [Hz]	Stiffness [MN/m]	Damping Ratio	Natural Freq. [Hz]	Stiffness [MN/m]	Damping Ratio
$R^2$	0.97	0.90	0.95	0.97	0.25	0.0028	0.90	0.94	0.94
RMSE	0.23	0.11	0.0050	0.11	0.99	0.9	0.50	0.1	0.0024

### 4.3 Optimal Control Methodology

This section describes the optimal control strategy used for vibration suppression. The methodology is tested with offset mass experiments prior to conducting robotic milling experiments. The experimental setup is first described followed by the results.

#### 4.3.1 Linear Quadratic Regulator

This work uses an optimal controller derived from the solution of the Linear Quadratic Regulator (LQR) problem to minimize the robot's end effector vibrations. The effectiveness of LQR controllers have been demonstrated in other disturbance rejection applications [40, 41]. Prior work on disturbance rejection in a dual inverted pendulum system has also demonstrated that an LQR controller exhibits better disturbance rejection than an  $H_\infty$  controller even though the  $H_\infty$  controller does not require tuning of the cost function weights [67]. Without loss of generality, consider the following state space representation in discrete time:

$$\delta_{p+1} = \mathbf{A}_d \delta_p + \mathbf{B}_d u_p \quad (18)$$

where  $\delta_p$  is the state vector ( $\delta_p = [\delta_p \quad \dot{\delta}_p]^T$ ),  $u_p$  is the system input at time index  $p$ , and

$$\mathbf{A}_d = \sum_{i=0}^{\infty} \frac{\mathbf{A}^i T^i}{i!} \quad (19)$$

$$\mathbf{B}_d = (\mathbf{A}_d - \mathbf{I}) \mathbf{A}^{-1} \mathbf{B} \quad (20)$$

where  $T$  is the system sampling time. For a mass-spring-damper system expressed in terms of the modal mass  $m = k/w_n^2$  and damping coefficient  $c = 2mw_n/\zeta$  attached to a controlled point subjected to a disturbance induced by an external force [42],  $\mathbf{A}$  and  $\mathbf{B}$  are given by

$$\mathbf{A} = \begin{bmatrix} 0 & 1 \\ -k & -c \end{bmatrix} \quad (21)$$

$$\mathbf{B} = [0 \quad 1/m]^T \quad (22)$$

Because  $\mathbf{A}$  depends on the natural frequency, damping ratio, and modal stiffness of the robot, Equation (18) is the discrete state space representation of the GPR model. Thus, state feedback control  $u_p = -\mathbf{W} \delta_p$  leads to

$$\delta_{p+1} = (\mathbf{A} - \mathbf{B}\mathbf{W}) \delta_p \quad (23)$$

Thus, the LQR problem is used to determine the optimal state feedback gains  $\mathbf{W}$  such that the system is asymptotically stable and a prescribed cost function is minimized. To determine  $\mathbf{W}$ , the following cost function is defined

$$J = \sum_{p=0}^{\infty} (\delta_p^T \mathbf{Q} \delta_p + u_p^T \mathbf{R} u_p) \quad (24)$$

where  $\mathbf{Q}$  and  $\mathbf{R}$  are known positive semi-definite and positive definite symmetric constant matrices that weight the state vector and the system input, respectively. In this work,  $\mathbf{Q}$  was fixed as  $\begin{bmatrix} 1 & 0 \\ 0 & 0.001 \end{bmatrix}$  to ensure the position and velocity measurements were converted into the same units while  $\mathbf{R}$  was determined through simulation to be 0.001 in order to produce a stable response. Hence,  $\delta_p^T \mathbf{Q} \delta_p$  corresponds to minimization of the state vector while  $u_p^T \mathbf{R} u_p$  corresponds to minimization of the control effort. Note that Equation (24) implies infinite-horizon and discrete-time constraints. Minimization of the cost function  $J$  leads to the following expression for  $\mathbf{W}$

$$\mathbf{W} = (\mathbf{R} + \mathbf{B}^T \mathbf{P} \mathbf{B})^{-1} (\mathbf{B}^T \mathbf{P} \mathbf{A}) \quad (25)$$

where  $\mathbf{P}$  is a positive definite symmetric constant matrix calculated from the solution of the Riccati equation [43]

$$\mathbf{P} = \mathbf{A}^T \mathbf{P} \mathbf{A} - (\mathbf{A}^T \mathbf{P} \mathbf{B}) (\mathbf{R} + \mathbf{B}^T \mathbf{P} \mathbf{B})^{-1} (\mathbf{B}^T \mathbf{P} \mathbf{A}) + \mathbf{Q} \quad (26)$$

Note that, because  $\delta_p = [\delta_p \quad \dot{\delta}_p]^T$ ,  $\mathbf{W} = [w_1 \quad w_2]$ . Hence, the feedback gains  $w_1$  and  $w_2$  are applied to the measured displacement  $\delta_p$  and the calculated  $\dot{\delta}_p$ , respectively. Figure 20 shows a schematic of the control implementation after  $\mathbf{W}$  is calculated for a given robot pose using the GPR model described earlier.

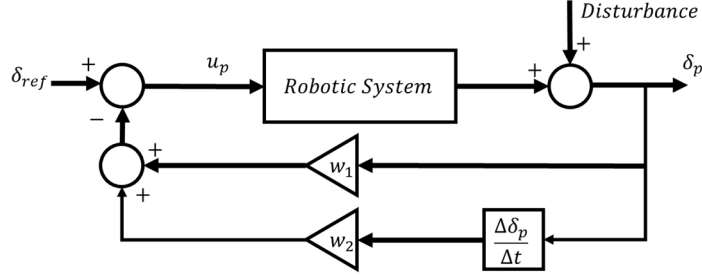


Figure 20. Control implementation block diagram. Note that in this work,  $\delta_{ref} = \mathbf{0}$  for disturbance rejection implementation.

#### 4.3.2 Offset Mass Experiments

To evaluate the performance of the LQR based optimal control approach discussed in the previous section, a controlled disturbance experiment was first performed. In this experiment, a rotating offset mass was attached to the robot end effector to induce vibrations at a prescribed excitation frequency. Figure 21 shows the setup of the offset mass experiment for a given arm configuration. The mass  $m_o$  is fixed at a constant length  $L$  from the spindle axis. When the spindle rotates at a constant speed  $\Omega$ , a centripetal force  $F_c$  acts toward the spindle axis. Assuming that the mass experiences minimal drag and the centripetal force acts radially, the force can be modeled as a sinusoidal wave relative to a fixed reference frame with a period determined by the spindle rotation speed

$$F_c = m_o L (2\pi\Omega)^2 \sin\left(\frac{2\pi t}{\Omega}\right) \quad (27)$$

The above periodic force induces cyclic vibration of the robot tool tip. For these experiments,  $L$  and  $m_o$  are 50.8 mm and 1 kg, respectively. While the spindle is rotating, the robot is commanded to move at 20 mm/s in a straight line in the X direction for 2

seconds. The rotating offset mass therefore induces instantaneous path deviations in the Y direction at the spindle frequency.

The offset mass experiments were conducted at spindle speeds of 480 RPM, 960 RPM, and 1440 RPM, which correspond to excitation frequencies of 8 Hz, 16 Hz, and 24 Hz, respectively. The instantaneous displacements (vibrations) of the robot were measured using a 6-dof laser tracker (Leica AT960 with T-MAC) at a sampling frequency of 1 kHz. Finite backward difference was used to compute the velocities from the instantaneous position measurements obtained from the tracker. The sensing and control actions were implemented in the Beckhoff TwinCAT real-time programming environment running on a personal (control) computer. The KUKA KRC4 controller was configured to drive the robot along the programmed linear path while the external path corrections in the Y direction were implemented using the KUKA Robotic Sensor Interface (RSI). The control computer communicated values to the KUKA RSI using the EtherCAT protocol at a command rate of 250 Hz.

For the midpoint robot position shown in Figure 21, the end-effector Cartesian configuration defined by XYZ (mm), Rx, Ry, and Rz (degrees) was [2300, 0.00, 680, -90.37, -89.13, -90.05], and the corresponding joint angles (in degrees) were [-0.11, -27.46, 94.04, 179.42, 66.83, -0.58]. To first test the optimal control methodology without introducing any prediction errors of the GPR model, the robot modal properties were measured directly using impact hammer tests at the midpoint of the path and used to tune the controller. Note that this approach assumes that the robot's modal properties change significantly over the 20 mm from the sampled configuration. The Y direction natural frequency, stiffness, and damping ratio that were 8.5 Hz, 0.775 MN/m, and 0.179,

respectively, and the LQR controller gains  $w_1$  and  $w_2$  were computed to be 0.079 and 0.0059, respectively.

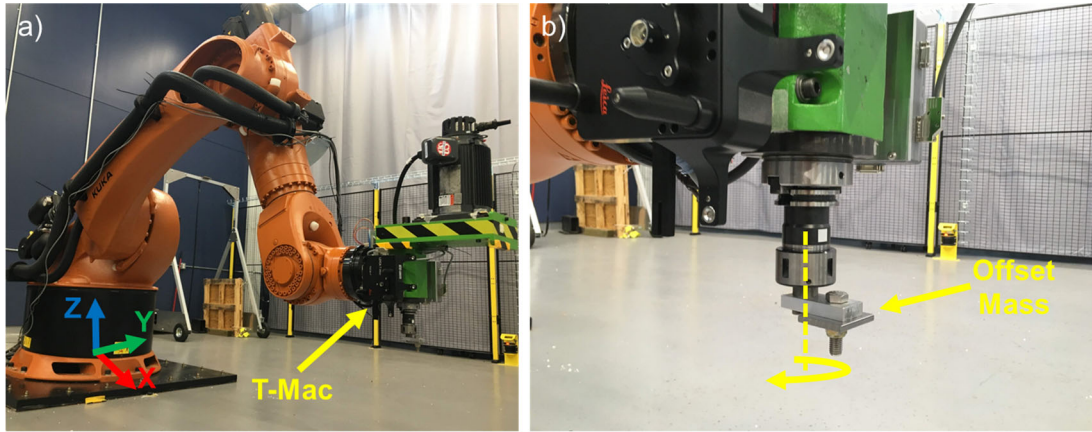


Figure 21. a) Robot and b) zoomed in tooling setup for offset mass experiments.

Figure 22 shows the results of applying the optimal controller during the rotating offset mass experiments. For the 480 RPM and 960 RPM cases, the controller is seen to reduce the vibration amplitudes from 0.93 mm to 0.39 mm and from 0.36 mm to 0.15 mm, respectively. However, at 1440 RPM, the controller is unable to suppress the vibrations and the robot even experiences harmonic dissonance. This is because the KRC4 robot controller exhibits a 32 ms delay between the commanded input and the actuator response. The cause of this delay appears to be the required breakaway torque and transition from stiction to sliding friction within the robot joints, and possible interface delays between the robot controller and the actuator commands [44, 45]. Unfortunately, determination and minimization of the root cause of the delay requires proprietary knowledge of the robot internal mechanics and software infrastructure, which is not available to end users. Therefore, the delay limits the range of spindle speeds where the LQR controller is

effective. However, this limitation is hardware dependent and general implementation of the proposed optimal control methodology is still applicable.

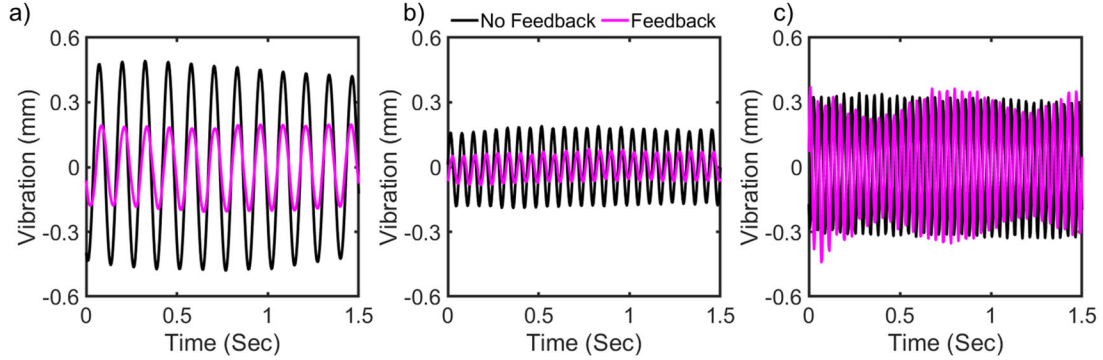


Figure 22. Offset mass experiment results for spindle speeds of (a) 480 RPM, (b) 960 RPM, and (c) 1440 RPM.

#### 4.3.3 Pose-Dependent Controller versus Constant Gain Controller

To evaluate the performance of the controller over longer paths, the offset mass experiments were conducted over a 900 mm long path at spindle speeds of 480 RPM and 960 RPM. The starting point of the path was the ending arm configuration shown in Figure 18 with robot motion in the +Y direction at a feed rate of 84 mm/s. Hence, the robot starts at an extended configuration and moves closer to its base as it traverses along the path. It is evident from Figure 19 that the X direction modal parameters change significantly along the 900 mm path length. In addition, note that the controller is configured to minimize vibrations in the X direction. Therefore, in these experiments,  $\mathbf{W}$  was calculated at 20 equally spaced points along the path using  $\mathbf{A}_d$  and  $\mathbf{B}_d$  matrices predicted by the GPR model. The values for the control gains  $w_1$  and  $w_2$  were then fitted using a polynomial fit with respect to distance along the path for gain scheduling within the TwinCAT real-time

environment. The fitted polynomial forms for  $w_1$  and  $w_2$  as a function of distance along the path  $d$  are as follows:

$$w_1 = -4.3 * 10^{-5}d + 0.12 \quad (28)$$

$$w_2 = -3 * 10^{-14}d^4 + 7 * 10^{-11}d^3 - 6 * 10^{-8}d^2 + 1 * 10^{-5}d + 0.006 \quad (29)$$

Figure 23 shows the gains as a function of distance along the path. Interestingly, the gains exhibit significant trends as the arm moves closer to its base. For instance,  $w_1$  becomes smaller because the arm's compliance and natural frequency in the X direction decrease as the end effector moves toward its base. Therefore, the controller requires less control action, as indicated by the smaller gains, to suppress vibration as the arm moves closer to its base. In addition,  $w_2$  also decreases in a nonlinear fashion that corresponds to a decrease in the damping ratio as shown before in Figure 19. Hence,  $w_2$  decreases in importance to compensate for the reduction in damping of the system response to input commands. Note that, in each control cycle, the TwinCAT environment calculates the instantaneous  $\mathbf{W}$  as a function of the toolpath position. The calculated  $\mathbf{W}$  is then applied to the measured disturbance to determine the corresponding control input. These results provide new insight into the performance of a pose-dependent optimal controller in that compliant systems such as 6-dof industrial robots require larger gains to suppress vibration and that the optimal gains for pose-dependent systems can vary significantly over a long path characterized by significant changes in the robot's vibration characteristics.

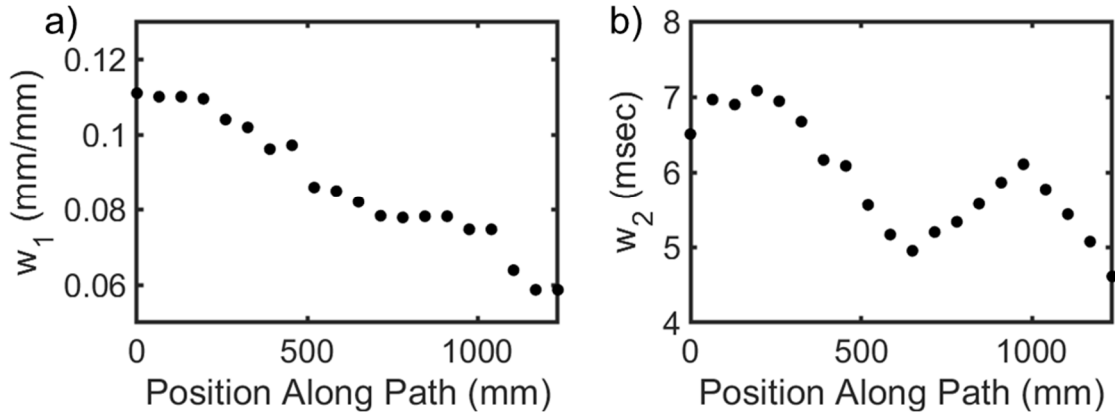


Figure 23. LQR gains for (a)  $w_1$  and (b)  $w_2$  along the path.

In addition, two constant gain controllers were evaluated in addition to the pose-dependent controller. The constant gain controllers were developed by calculating  $\mathbf{W}$  at a single robot configuration. The constant  $\mathbf{W}$  was then applied throughout the entire path. One set of gains was computed by using the robot configuration corresponding to the start of the path, and the other set was computed by using the robot configuration corresponding to the end of the path. The controller gains  $w_1$  and  $w_2$  computed at the start configuration were 0.11 and 0.0065, respectively, and  $w_1$  and  $w_2$  computed at the end configuration were 0.06 and 0.005, respectively. Note that robot is significantly more compliant at the start of the path than at the end of the path for the offset mass experiments, and therefore the gains computed at the start configuration are significantly larger than the gains computed at the end configuration. The results of the offset mass experiments are shown in Figure 24, and the start and end vibration amplitudes are presented in Table 7. It is seen that the vibrations of the robot increase as the arm traverses along the path. The open loop vibration amplitudes transition from 0.40 mm to 0.21 mm and 0.15 mm to 0.08 mm for the 480 RPM and 960 RPM conditions, respectively. This is expected because, for a given excitation

frequency, the robot's modal parameters change significantly along the path, as seen in Figure 19. Note that all the tested controllers appear to initially suppress vibration. However, while using the constant gain values computed from the start of the path initially results in similar performance as the pose-dependent controller, the system becomes unstable as it approaches the end of the path. This is because the gain values computed at the start of the path do not consider the change in stability conditions as the arm moves towards its base. In addition, the constant gain values computed at the end of the path were not able to suppress vibration as well as the pose-dependent controller at the start of the path. This is because the robot configuration at the end of the path was significantly stiffer and therefore did not require larger control gains. Hence, when applying these gains to regions where the robot is significantly more compliant, such as the start position, these control gains will not produce significant vibration suppression. These results show that the pose-dependent controller outperforms both constant gain controllers by minimizing vibration while maintaining stability.

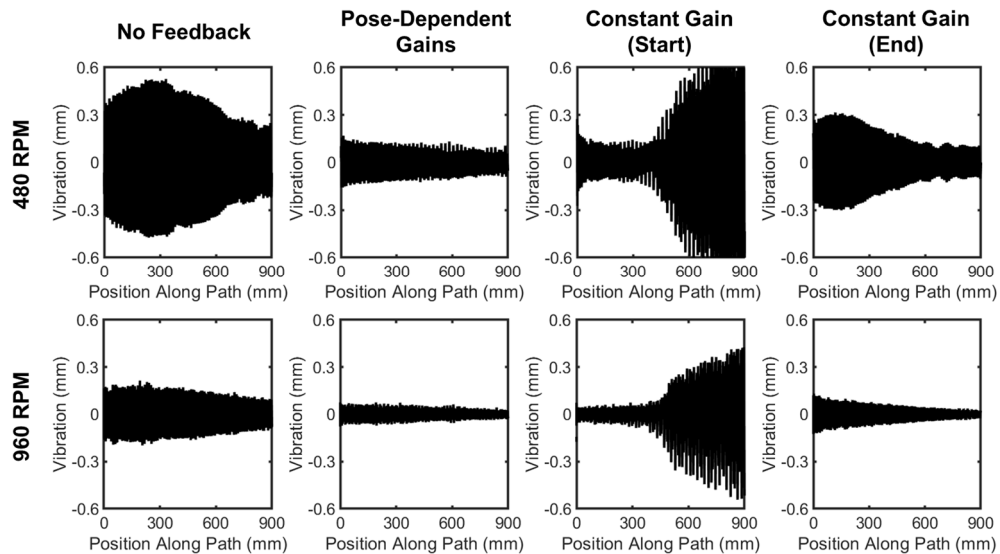


Figure 24. Offset mass experiment results.

Table 7. Start and end vibration amplitudes. Units are in mm.

Speed (RPM)	Start				End			
	No Feedback	Pose- Dependent Gains	Constant Gain (Start)	Constant Gain (End)	No Feedback	Pose- Dependent Gains	Constant Gain (Start)	Constant Gain (End)
<b>480</b>	0.40	0.13	0.14	0.29	0.21	0.08	1.39	0.09
<b>960</b>	0.15	0.06	0.50	0.10	0.08	0.03	0.42	0.03

#### 4.4 Milling Experiments

This section describes the milling experiments conducted to study the performance of the presented vibration suppression controller. The experimental setup is described followed by results and discussion.

##### 4.4.1 Experimental Setup

To evaluate further the performance of the active vibration suppression methodology when using both the GPR model and the LQR controller, robotic milling experiments were carried out. Two peripheral end milling experiments were performed without coolant on an Acetal Resin workpiece using a two flute, 25.4 mm diameter, 30° helix angle, cobalt tool. The axial depths of cut, feed/tooth, and spindle speeds utilized were 3 mm and 6 mm, 0.3 mm and 0.5 mm, and 125 and 250 RPM, respectively. The radial depth of cut and the length of cut were kept constant at 6 mm and 50 mm, respectively, in both tests. As shown in Figure 25, the experiments were conducted at two locations in the robot’s workspace to evaluate the effectiveness of the LQR controller to suppress milling force induced vibrations as a function of robot arm configuration. Note that the two robot configurations in Figure 25 differ significantly from each other and from the configuration shown in Figure 21. As discussed earlier, the robot’s modal vibration parameters vary with

arm configuration in the workspace, thus requiring the GPR model to predict the modal response at these locations. A full factorial experiment resulted in eight cutting conditions at two robot poses with and without the LQR controller for a total of 32 cutting tests. The same robotic milling setup used in the offset mass experiments was used in these experiments. Since the peripheral milling cuts create a machined wall surface and a floor surface on the workpiece, two separate, uncoupled controllers were implemented for vibrations in the X (wall surface) and Z (floor surface) directions. Note that joint angle control can address coupled vibrations in the X and Z directions. However, joint angle control requires an Inverse Kinematic approach that requires a highly accurate geometrical representation of the robotic arm. No control action was implemented in the robot Y direction, which is aligned with the tool feed direction.

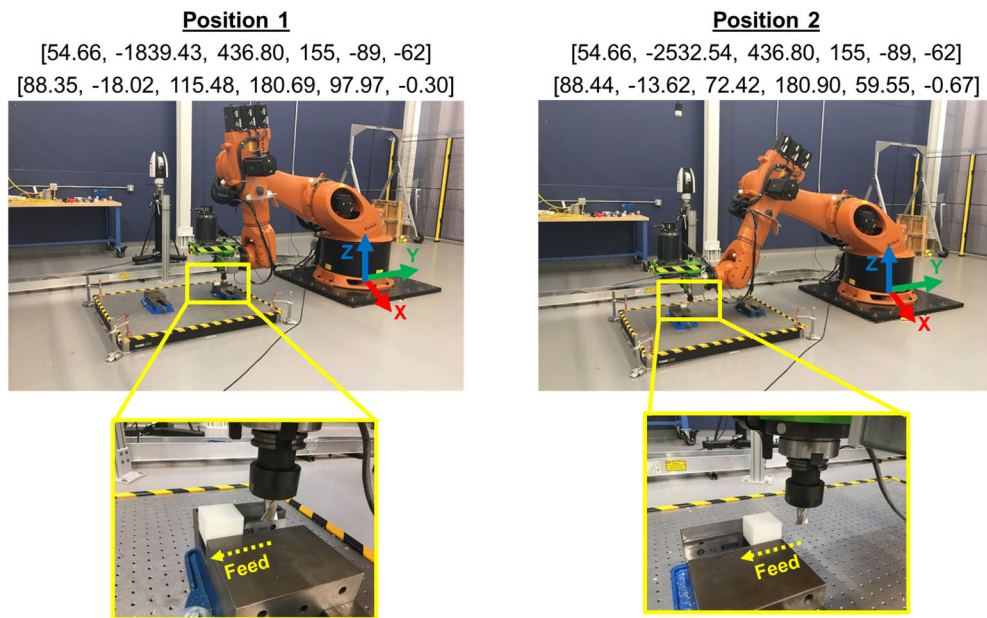


Figure 25. Robot poses for milling experiments. The midpoint of the tool path used in the milling experiments is provided in Cartesian (top) XYZ (mm), Rx, Ry, and Rz (degrees) and joint angles (bottom) notation.

The Cartesian positions of the robot end effector were input to the GPR model to predict the modal vibration parameters (stiffness, natural frequency, damping ratio) in the X and Z directions. Comparison of the predicted and measured modal parameters in Table 8 shows that the GPR model is able to predict the modal parameters within 10%. The largest error corresponds to the X direction modal stiffness of the robot at Position 1, which, as seen from Figure 19, corresponds to a region of rapid decrease in the modal stiffness, and therefore the prediction accuracy is lower.

Table 8. GPR model predictions at robot Positions 1 and 2.

Position		X			Z		
		Natural Freq. [Hz]	Stiffness [MN/m]	Damping Ratio	Natural Freq. [Hz]	Stiffness [MN/m]	Damping Ratio
1	Predicted	9.60	1.32	0.146	11.87	1.95	0.142
	Measured	9.50	1.20	0.150	11.88	1.99	0.13
2	Predicted	7.45	0.73	0.186	9.00	1.10	0.16
	Measured	7.40	0.74	0.190	9.06	1.15	0.15

Table 5 lists the optimal control gains computed from Equation (25) using the cost function in Equation (24). The GPR model predictions in Table 8 were used to determine the LQR controller gains corresponding to the two robot positions where milling was performed. Note that the control gain  $w_1$  for Position 2 is significantly larger than the corresponding control gain for Position 1, which corresponds to the results shown in Figure 23. This is to be expected because the system is more compliant at Position 2, which requires a stronger control action to suppress the vibration. In addition,  $w_2$  is larger for Position 2 than Position 1 because the damping ratio increases as the arm is outstretched. Therefore, the importance of the velocity term increases to compensate for the increase in damping of the system response to input commands.

Table 9. Optimal control gains.

Position	X		Z	
	$w_1$	$w_2$	$w_1$	$w_2$
1	0.061	0.0054	0.037	0.0033
2	0.11	0.0080	0.069	0.0057

#### 4.4.2 *Vibration Measurements*

Table 6 lists the RMS vibration amplitudes for all the robotic milling experiments obtained from laser tracker measurements. It can be seen that the LQR controller is able to reduce the RMS vibration amplitudes for a range of cutting conditions. The largest vibration amplitude was observed in Test 5, which had a larger feed and axial depth of cut, and a tooth passing frequency of 8.3 Hz that is close to the robot's dominant natural frequencies of 9.50 Hz and 7.40 Hz in the X direction, and 11.88 Hz and 9.06 Hz in the Z direction at Positions 1 and 2, respectively. The smallest vibrations occurred in Test 4, which had the lowest feed and axial depth of cut and a tooth passing frequency of 4.16 Hz that is farther away from the robot's natural frequencies. In this work, the average controller vibration reduction at the tooth passing frequencies of 4.2 Hz (Tests 1, 2, 3, and 4) and 8.3 Hz (Tests 5, 6, 7, and 8) were found to be 42% and 52%, respectively. Hence, the controller demonstrates better performance at 8.3 Hz than opposed to 4.2 Hz. This is because the controller is able to best suppress vibrations closest to the robot's predicted natural frequencies that were used in developing the controller. The controller performance for the cutting feeds of 0.3 mm (Tests 3, 4, 7 and 8) and 0.5 mm (Tests 1, 2, 5, and 6) were found to be 48% and 46%, respectively, demonstrating insignificant influence of the cutting feed in these experiments. In addition, the controller performance was found to be similar for axial depths of 3 mm (Tests 2, 4, 6 and 8) and 6 mm (Tests 1, 3, 5, and 7) with

improvements of 47% and 48%, respectively. Hence, the controller appears to be significantly influenced by the vibration frequency. On average, the controller is able to reduce the vibration amplitude by  $51\% \pm 13\%$  and  $43\% \pm 16\%$  in X and Z directions, respectively.

Table 10. RMS vibration amplitude results (mm) for milling experiments. “Open” refers to open loop and “Control” refers to LQR control.

Test No.	Speed (RPM)	Feed (mm)	Axial Depth of Cut (mm)	RMS Vibration Amplitude (mm)							
				Position 1				Position 2			
				X		Z		X		Z	
				Open	Control	Open	Control	Open	Control	Open	Control
1	125	0.5	6	0.279	0.142	0.067	0.042	0.331	0.191	0.115	0.046
2	125	0.5	3	0.293	0.132	0.069	0.046	0.216	0.143	0.049	0.031
3	125	0.3	6	0.249	0.109	0.058	0.035	0.202	0.166	0.071	0.038
4	125	0.3	3	0.146	0.066	0.033	0.025	0.113	0.071	0.047	0.020
5	250	0.5	6	0.388	0.158	0.101	0.036	0.401	0.244	0.093	0.049
6	250	0.5	3	0.147	0.073	0.041	0.036	0.259	0.092	0.048	0.024
7	250	0.3	6	0.284	0.118	0.064	0.045	0.378	0.174	0.098	0.037
8	250	0.3	3	0.158	0.048	0.050	0.030	0.209	0.075	0.066	0.018

Figure 26 shows representative time series data for the vibrations in Test 1 and Test 8. It can be seen that the larger arm compliance at Position 2 yields open loop vibrations in the X and Z directions that are larger than the corresponding vibrations at Position 1. Hence, the two positions exhibit two significantly different vibration responses for the same cutting conditions. For instance, the open loop RMS vibration amplitudes were 0.067 mm and 0.115 mm in the Z direction at Positions 1 and 2, respectively. In addition, the open loop RMS vibration amplitudes in the X direction at Positions 1 and 2 were 0.279 mm and 0.346 mm, respectively. In addition, it can be seen that the controller is able to significantly reduce the vibration amplitudes. For instance, Figure 26(b) shows that the

RMS vibration amplitude in the X direction is reduced from 0.158 mm to 0.048 mm at Position 1, and from 0.209 mm to 0.075 mm at Position 2. Similarly, the vibration amplitude in the Z direction is reduced from 0.050 mm to 0.030 mm at Position 1, and from 0.066 mm to 0.018 mm at Position 2. Note that the controller is unable to suppress the vibration completely due to the actuator delay and physical limitations of the actuator force that can be applied by the robot.

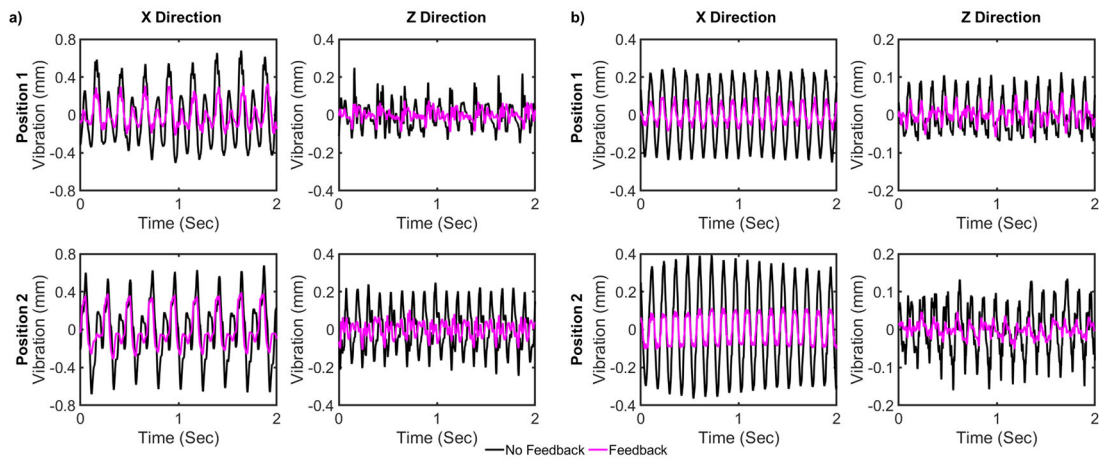


Figure 26. Vibration data with and without LQR control for (a) Test 1 and (b) Test 8.

Figure 27 shows the spectral decompositions of the vibration signals obtained in Test 1 and Test 8. Figure 27(a) shows that the controller is able to reduce vibration amplitudes at approximately 4 Hz and 8 Hz for both robot arm configurations (corresponding to Positions 1 and 2). Interestingly, the controller is also able to reduce the amplitude of some of the higher vibration modes. For instance, Figure 27(a) shows that the amplitude of the 24 Hz mode vibration mode in the X direction response at Position 2 is reduced. This is because reducing vibrations at 4 Hz and 8 Hz reduces their corresponding harmonics, including at 24 Hz. Hence, the controller's ability to suppress lower frequency

vibrations can propagate to minimization of higher frequency vibrations as well. In addition, it can be seen that both Position 1 and Position 2 exhibit significantly different frequency responses for the same cutting conditions, thus demonstrating that Position 1 and Position 2 have significantly different vibration characteristics. For instance, Figure 27(b) shows that the frequency response at 8 Hz in the Z direction is almost twice as large at Position 1 as at Position 2. In addition, the frequency responses in the Z direction show that the influence of the higher vibration modes is more prevalent at Position 2 than at Position 1, especially in Test 8.

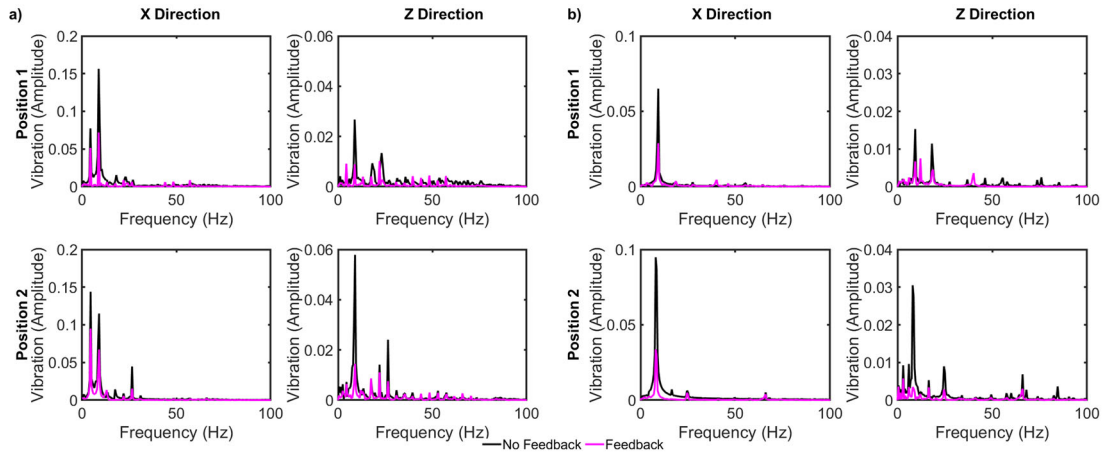


Figure 27. Spectral decomposition of the vibration data for (a) Test 1 and (b) Test 8.

#### 4.4.3 Part Surface Measurements

The eventual goal of the proposed optimal control methodology is to enhance the machining accuracy of the robot. To evaluate this, the wall and floor surface features, oriented in the X and Z directions, respectively, generated by the open and closed loop milling experiments were measured using a Coordinate Measuring Machine (CMM). The CMM line scans were spaced 0.5 mm along the axial depth of cut. Each scan consisted of

30 mm linear paths with a scanning increment of 50 points/mm. All the points along the scans were then averaged to calculate the average wall and floor surface profiles for each test. Figure 28 shows the average surface profiles obtained in Test 1 and Test 8. It can be seen that the measured deviations of the wall and floor surfaces are reduced when the LQR controller is implemented. Table 11 shows the RMS surface deviations for all cutting tests. The RMS surface deviations are found to be correlated with the vibrations with a Pearson's Correlation Coefficient of +0.76. On average, the LQR control methodology is able to reduce the surface deviations by  $25\% \pm 12\%$  in both the X and Z directions.

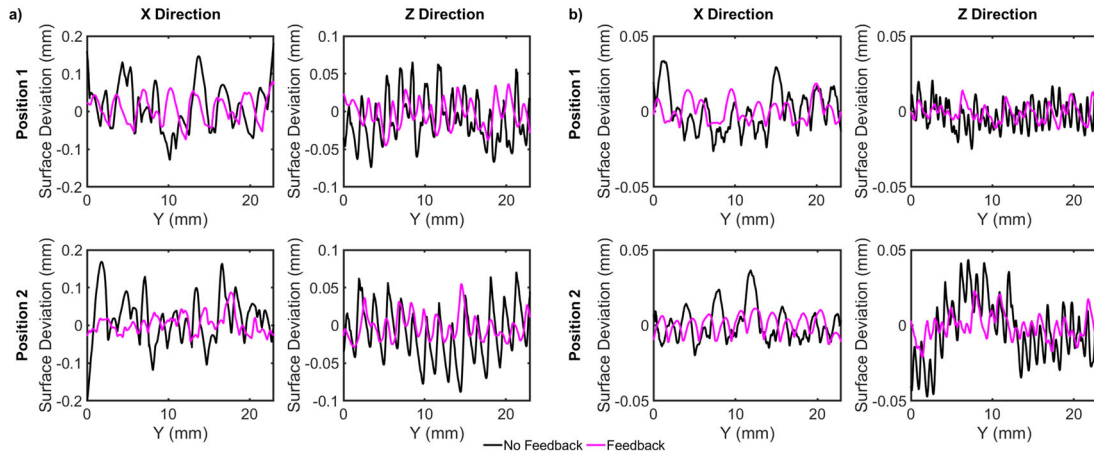


Figure 28. CMM results for (a) Test 1 and (b) Test 8.

Table 11. RMS surface deviations (in mm) in milling experiments. “Open” refers to open loop and “Control” refers to closed-loop optimal control.

Test No.	Speed (RPM)	Feed (mm)	Axial Depth of Cut (mm)	RMS Vibration Amplitude (mm)							
				Position 1				Position 2			
				X	Z	X	Z	X	Z	X	Z
1	125	0.5	6	0.060	0.045	0.032	0.021	0.064	0.044	0.035	0.020
2	125	0.5	3	0.056	0.049	0.017	0.015	0.045	0.037	0.034	0.021
3	125	0.3	6	0.034	0.027	0.024	0.016	0.040	0.034	0.022	0.018
4	125	0.3	3	0.024	0.018	0.011	0.009	0.027	0.020	0.018	0.014
5	250	0.5	6	0.068	0.052	0.039	0.019	0.064	0.042	0.036	0.027
6	250	0.5	3	0.032	0.026	0.015	0.013	0.048	0.041	0.024	0.020
7	250	0.3	6	0.027	0.020	0.011	0.010	0.029	0.021	0.019	0.014
8	250	0.3	3	0.026	0.019	0.012	0.010	0.029	0.020	0.020	0.014

#### 4.5 Summary

This section presented an optimal control methodology for active vibration suppression in robotic milling with a 6-dof industrial robot characterized by pose-dependent modal parameters consisting of the modal stiffness, undamped natural frequency, and damping ratio. The modal parameters predicted by a Gaussian Process Regression (GPR) model were used to formulate and solve the robot pose-dependent LQR optimal control problem to compute pose-dependent optimal gains for active vibration suppression. The LQR control methodology was validated using both offset mass experiments and robotic milling experiments under various excitation conditions and robot poses. The displacement gain was found to increase with the robot’s compliance while the velocity gain was found to positively trend with the robot’s damping ratio. The pose-dependent optimal controller was demonstrated to outperform constant gain controllers in the offset mass experiments. The controller was demonstrated to reduce milling vibration

amplitudes by  $51\% \pm 13\%$  and  $43\% \pm 16\%$  in X and Z directions, respectively, which was also shown to be correlated with a decrease in the machined surface deviations. Future generations of industrial robots should minimize actuator delay to facilitate better active control and therefore enhanced milling accuracy at even higher excitation frequencies.

## **CHAPTER 5. HYBRID STATISTICAL MODELLING OF ROBOT FREQUENCY RESPONSE FUNCTION**

### **5.1 Introduction**

Modal impact hammer experiments are generally used to calibrate pose-dependent FRF-prediction models because they can be used at any point in the workspace regardless of application constraints (e.g., workpiece locations for milling). However, this approach, known as Experimental Modal Analysis (EMA), can only be used at discrete points in the workspace corresponding to specific robot arm configurations, and therefore requires significant off-line testing effort to obtain adequate spatial resolution over the entire workspace. Alternatively, the process of determining robot FRFs through Operational Modal Analysis (OMA), which utilizes on-line milling process data (e.g., forces, vibrations, accelerations, etc.) gathered during robot operation, can continuously sample arm configurations along the tool path and thereby achieve greater spatial resolution. However, use of only OMA from milling process data is constrained by workpiece and fixturing limitations. For instance, the workpiece must be sufficiently large to sample a large workspace, which increases cost. In addition, the length and spacing of the required tool paths to sufficiently sample the robot workspace is unknown. Therefore, conducting OMA alone can be expensive and time-consuming. In light of these limitations, a hybrid modelling approach that combines FRF measurements from EMA and OMA can be helpful for efficiently creating a more accurate pose-dependent robot FRF prediction model valid over a larger workspace.

This chapter presents a statistical modelling approach to efficiently create an accurate robot FRF model valid over its workspace by combining FRFs calculated from EMA and OMA. An example schematic of the EMA and OMA measurement procedures used in the hybrid modelling approach is shown in Figure 29. Impact hammer experiments are conducted at discrete points in the robot’s workspace to initially train a Gaussian Process Regression (GPR) model of the robot’s pose-dependent FRF. Following this, OMA is used to calculate more spatially dense robot FRFs from milling experiments along a tool path in the robot’s workspace. The FRF calculated from OMA is then used to augment the GPR model calibrated (or trained) with EMA data. Instead of complete model retraining, the OMA-based FRFs are used to update the posterior distribution of the GPR model using Bayesian updating. In addition, prior knowledge of the GPR model hyperparameters is used to reduce the number of iterations required for hyperparameter optimization during model augmentation. The results of the statistical modelling approach are discussed, and the key conclusions of the work are summarized.

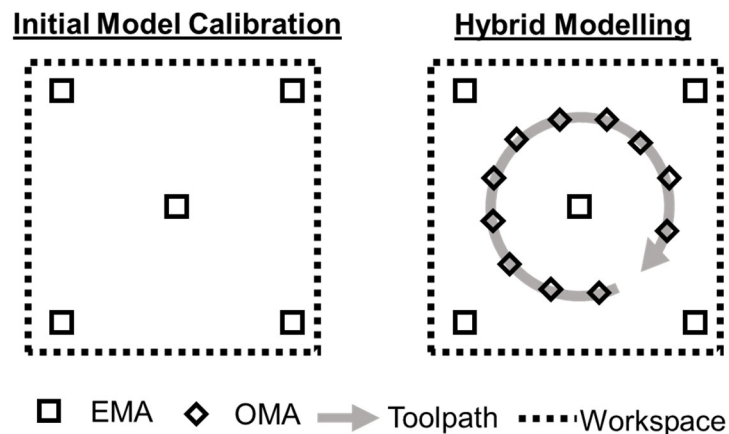


Figure 29. Example of hybrid modelling approach.

## 5.2 Hybrid Modelling Methodology

This section describes the hybrid modelling approach used in this chapter. The approach to calculate the FRFs using EMA to initially calibrate the data-driven is described. Then, the OMA approach to calculate the FRF using milling force and tool tip vibration data is described. Finally, the hybrid modelling approach that updates the initially calibrated EMA-based model using OMA-based FRFs is detailed.

### 5.2.1 FRF Computation using EMA

In the hybrid modelling approach, EMA is conducted through modal impact hammer tests performed at discrete points in the robot's workspace corresponding to specific arm configurations to determine the pose-dependent FRFs used to initially calibrate the GPR model. Note that the EMA based FRF computation and GPR modeling methods in this chapter is conducted in the same manner as described in Chapters 3 and 4. Therefore, Equation (5) was used to calculate the robot FRFs from the auto spectral densities of the input force signals and the cross-spectral densities of the force and acceleration signals acquired from impact hammer tests.

### 5.2.2 FRF Computation using OMA

After the initial model calibration step using the EMA-based FRFs, OMA is performed using the milling force and tool tip vibration data to calculate the robot FRFs along a more densely sampled tool path. Note that OMA methods including the transmissibility function-based [51] and Enhanced Frequency Domain Decomposition (EFDD) [52] methods have been used in prior robotic milling applications. However, the

transmissibility function–based method requires at least two tool paths to be executed for each robot configuration and the EFDD method only determines the mode shape. In this chapter, an alternative method of conducting OMA, which does not require multiple tool paths and can identify the mode shape in addition to scaling, is presented.

The OMA method in this chapter involves computing the robot FRF using Equation (5), similar to the EMA experiments, from the auto spectral densities of the cutting forces and the cross-spectral densities between the milling forces and tool tip vibrations. Note that milling forces theoretically consist of harmonics associated with the spindle and tooth passing frequencies, and therefore the milling force auto-spectral density at the unassociated frequencies would be 0. Thus, Equation (5) can theoretically only compute compliances at the spindle and tooth passing frequencies. However, prior work [58-60, 68] has shown that background noise in the force signal can generate broadband excitation of the dynamic structure, which enables determination of robot FRFs from operational data. Therefore, the robot FRF can actually be calculated from milling force and tool tip vibration data by using Equation (5) when there is sufficient background noise excitation in the milling force signal.

### *5.2.3 Initial Model Calibration*

The output forms of the GPR model that predicts the FRF as a function of robot Cartesian position are given in Equation (9) and (10) presented in Chapter 3. However, the GPR modelling approach in Chapter 3 was limited to predicting the natural frequency, damping coefficient, and modal stiffness of only the dominant vibration mode of a 6-dof industrial robot. However, modelling of the entire robot FRF is desired for a more accurate

prediction of the robot's vibration characteristics. Therefore, this chapter extends the prior robot FRF modelling approach to predict the entire FRF. To accomplish this, the robot FRF is separated into individual frequency bins. Then, an individual GPR model is trained to predict the FRF compliance of its corresponding frequency bin as a function of the arm configuration. Therefore, this approach results in multiple GPR models that together describe the entire FRF of the robot. Note that an alternative approach is to consider frequency and robot pose as input parameters in the GPR model, which would capture the correlations between frequency bins. However, this approach was previously shown to be computationally more expensive for model calibration and prediction due to the increase in size of the covariance matrix [69]. For instance, in this work, the size of the covariance matrix is 3x3 while the size of the covariance matrix using frequency as an input is 393x393.

#### 5.2.4 Bayesian Updating with OMA-based FRFs

Note that the posterior distribution of a GPR model is traceable through Bayesian inference. Thus, when a new data point, i.e. OMA-based FRF, is added to the initially calibrated EMA-based data set, the covariance matrix can be simply recomputed and the updated Equations (9) and (10) constitute the updated GPR model. However, this method does not update  $\sigma_l$ ,  $\sigma_f$ ,  $\sigma^2$ , and the coefficients of the basis function  $\mu(p)$ , which make up the set of hyperparameters  $\theta$ . To calculate the hyperparameters during initial model calibration, the following marginal log-likelihood function is maximized

$$P(y|p, \theta) = -\frac{1}{2}(y - \mu)^T[\mathbf{K}(p, p) + \sigma^2\mathbf{I}]^{-1}(y - \mu) - \frac{n}{2}\log 2\pi - \frac{1}{2}\log|\mathbf{K}(p, p) + \sigma^2\mathbf{I}| \quad (33)$$

Therefore, when new OMA-based FRF data is added to the initially calibrated GPR model, Equation (33) must be completely re-optimized to recalculate the hyperparameters. Equation (33) is generally optimized using Newton quasi-static optimization, where the Newton step at iteration  $k$  is given by [70]

$$\Delta\theta_k = -\alpha_k \mathbf{A}_k^{-1} \nabla P(y|p, \theta_k) \quad (34)$$

where  $\mathbf{A}_k$  is an approximation of the Hessian matrix and  $\alpha_k$  is the step size. In this thesis, the Broyden–Fletcher–Goldfarb–Shannon (BFGS) algorithm is used to update the Hessian inverse at each iteration as follows [71]

$$\mathbf{A}_{k+1}^{-1} = \left( \mathbf{I} - \frac{\Delta\theta_k \boldsymbol{\tau}_k^T}{\boldsymbol{\tau}_k^T \Delta\theta_k} \right)^T \mathbf{A}_k^{-1} \left( \mathbf{I} - \frac{\boldsymbol{\tau}_k \Delta\theta_k^T}{\boldsymbol{\tau}_k^T \Delta\theta_k} \right) + \frac{\Delta\theta_k \Delta\theta_k^T}{\boldsymbol{\tau}_k^T \Delta\theta_k} \quad (35)$$

where  $\boldsymbol{\tau}_k$  is defined as

$$\boldsymbol{\tau}_k = \nabla P(y|p, \theta_{k+1}) - \nabla P(y|p, \theta_k) \quad (36)$$

Note that Newton quasi-static optimization is the most time-consuming step in calibrating the GPR model [72]. Prior researchers have attempted to alleviate this problem by either selecting hyperparameters that are assumed to not vary significantly [73] or periodically updating hyperparameters after updating the covariance matrix [74]. Generally, updating the hyperparameters is not necessary because sufficient (though suboptimal) model accuracy can be achieved with constant hyperparameters [75]. However, updating the hyperparameters to their optimal values has been shown to at least marginally improve model accuracy [76]. Note that there are certain occasions where updating the hyperparameters is absolutely necessary, such as when the underlying process

physics and statistics change significantly [61]. In this thesis, the process statistics are assumed to have changed since the OMA-based FRFs are computed from sensors (force/torque sensor and laser tracker) that exhibit different noise characteristics than sensors used to calculate the EMA-based FRFs (accelerometer and impact hammer).

In this chapter, the hyperparameters are updated by starting the Newton quasi-static optimization search  $\Delta\theta_0$  from the optimal hyperparameters determined during initial calibration of the GPR model using FRFs obtained from EMA. By starting the search at the initially calibrated hyperparameters, the number of optimization iterations is reduced if the optimal set of hyperparameters is close to the starting set. Therefore, this approach still ensures that an optimal set of hyperparameters is found while reducing the number of functional computations.

### **5.3 OMA and EMA Experiments**

This section describes the experiments conducted to perform EMA and OMA for the hybrid modelling approach. The experimental procedures are described followed by presentation of the collected data.

#### *5.3.1 EMA Experiments*

EMA was performed on a KUKA KR500-3 6-dof industrial robot at three points at 0 m, 585 m, and 1.235 m along a linear tool path in the Y direction, as shown in Figure 30. An impact hammer (PCB 086D05) was used to apply an impulse excitation in the direction of the measurement axis of a uniaxial piezoelectric accelerometer (PCB 352A21) mounted on the cutting tool tip. The applied impulse force and the corresponding acceleration

response were sampled at 17 KHz through the MetalMax software [77]. The corresponding FRFs were calculated from the force and twice-integrated acceleration data. Note that cross-coupling was assumed to be negligible [5] and therefore the robot FRFs were calculated only in the X, Y, and Z directions. The robot joint angles  $[\theta_1 \dots \theta_6]$  corresponding to the start, middle and end positions of the tool path were  $[87.9, -15.9, 128.3, 178.9, 113.1, -1.15]$ ,  $[84.1, -15.6, 98.7, 173.3, 83.9, 0.4]$ , and  $[88.9, -5.9, 45.6, 179.9, 40.6, -0.7]$  degrees, respectively. Note that although the example robot path considered in this work is a straight line aligned with a particular robot coordinate axis, the methodology is general and can be applied to other tool paths in the robot's workspace.

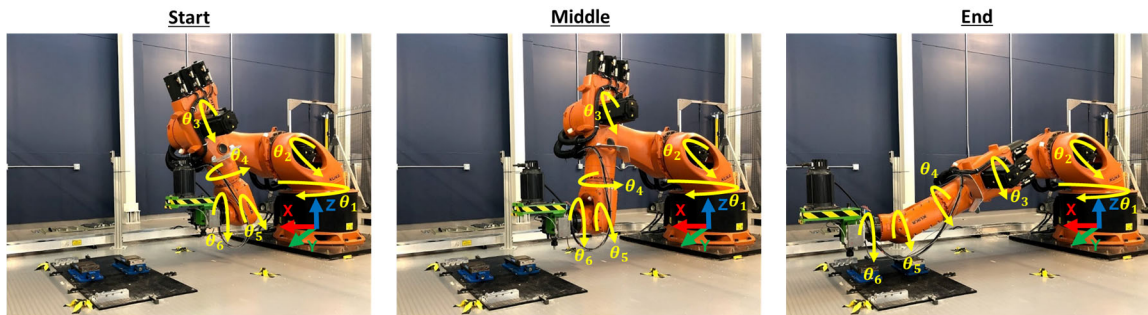


Figure 30. Robot configurations for impact hammer experiments. Note that the linear tool path is aligned with the Y direction of the robot base frame.

FRFs calculated from modal impact hammer tests performed in the X, Y, and Z directions of the three robot configurations are shown in Figure 31. It can be seen that as the robot arm extends from its base along the linear tool path, the X and Z direction compliances at frequencies less than 10 Hz increase while the compliance in the Y direction decreases. This is because of a cantilever beam effect that occurs with extension of the robot arm. In addition, there appears to be a dominant mode of vibration in each of the X,

Y, and Z direction FRFs ( $\sim 8$  Hz,  $\sim 23$  Hz, and  $\sim 8$  Hz, respectively) accompanied by weaker vibration modes. For instance, there appears to be a weaker mode at approximately 25 Hz in the X direction. Thus, these results justify the use of a data-driven modelling approach to predict the entire pose-dependent robot FRF.

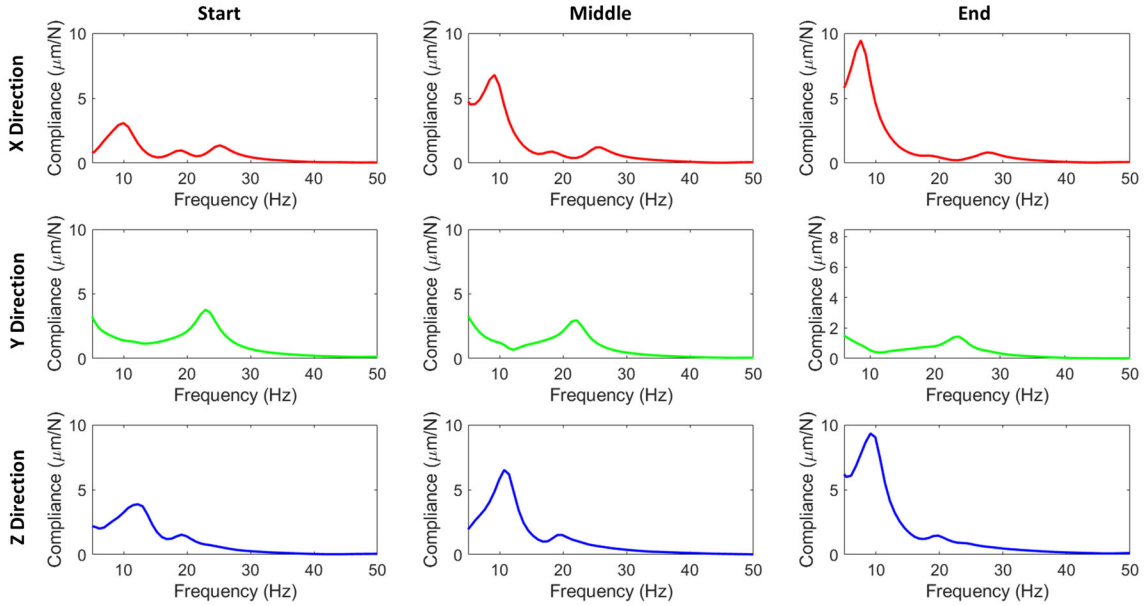


Figure 31. Robot FRFs computed from EMA experiments.

### 5.3.2 OMA Experiments

Dry peripheral milling tests (shown in Figure 32) with radial and axial depths of cut of 6 mm and 6 mm, respectively, were performed on Acetal Resin using a  $30^\circ$  helix angle, two flute, 25.4 mm diameter, cobalt end mill. The tool paths in these milling experiments were collinear with the Y direction of the robot base frame similar to the EMA tests shown in Figure 30. The feed per tooth was 0.85 mm and the spindle speed was 2700 RPM. The length of cut was 600 mm (from 0.635 m to 1.235 m along the tool path), and therefore the robot FRF cannot be assumed to be constant over the length of cut. Thus, the

cutting path was discretized into 50 mm cut lengths and the OMA-based FRFs were calculated over each cut length.

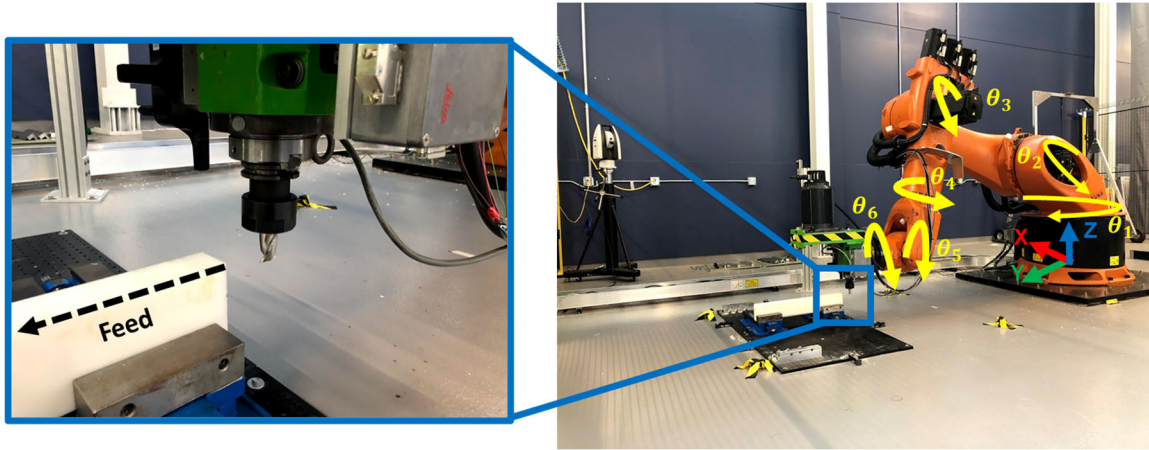


Figure 32. Milling experimental setup for OMA.

An ATI Omega 160 strain gauge-based force/torque sensor and a Leica AT960 6-dof laser tracker with T-MAC were used to measure the instantaneous milling forces and robot vibrations, respectively. Note that the laser tracker measures the vibrations at the T-MAC location and not at the tool tip. Therefore, the tool tip vibrations were calculated by applying a constant matrix transformation from the T-MAC location to the tool tip. In this work, the robot compliance is assumed to dominate the system vibrations compared to compliance of the tool-toolholder-spindle assembly. In addition, the milling forces at the tool tip were calculated by applying a constant matrix transformation from the force/torque sensor location to the tool tip. The force and vibration data were sampled synchronously at 1 kHz via the Beckhoff TwinCAT real-time programming environment. Similar to the modal impact hammer tests, the vibrations and milling forces were measured in the X, Y, and Z directions of the robot base frame. Note that robot vibrations have been shown to distort the force/torque sensor measurements and therefore an inverse filtering approach

described in detail in the author's prior work [69] was used to improve the accuracy of the measured cutting forces.

Figure 33 shows the milling force and tool tip vibration data for the OMA experiment. Note that the robot vibration amplitudes change as the tool tip moves along the tool path. Specifically, the X and Z direction vibrations visibly increase in amplitude because the compliance in these directions increases as the arm extends further from its base. Conversely, the Y direction vibrations decrease since the arm is stiffer in the Y direction as it extends further from the base. It is clear from these data that the robot FRF cannot be treated as constant throughout the tool path and therefore a pose-dependent FRF must be considered when modeling the robot's FRF.

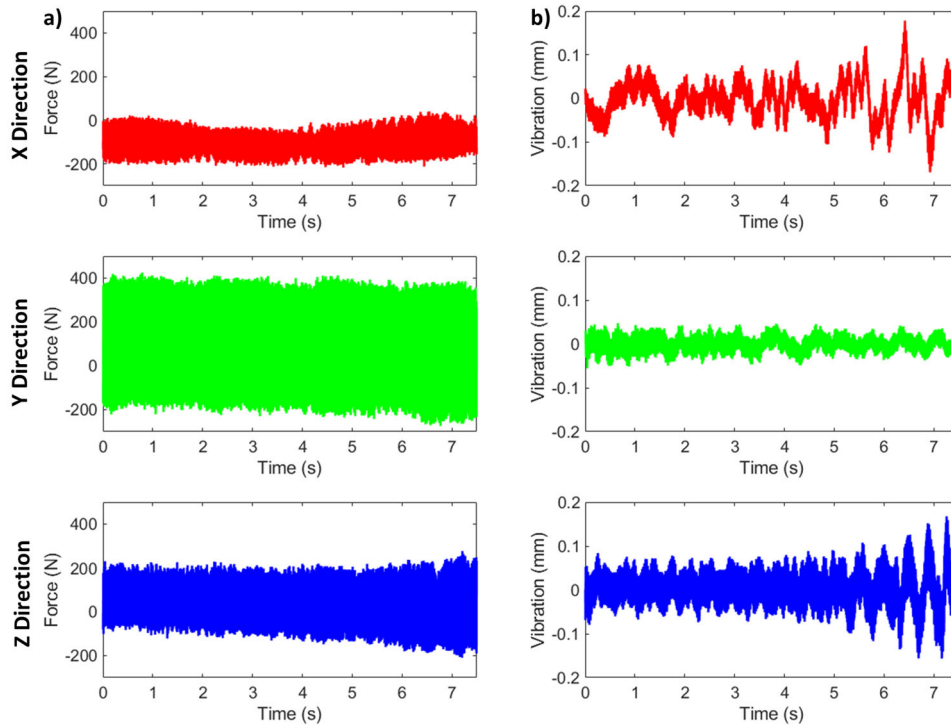


Figure 33. Measured a) milling forces and b) robot vibrations obtained in the longer tool path OMA experiment.

## 5.4 Hybrid Statistical Modeling Evaluation

The accuracy of the hybrid modelling methodology was evaluated using the following approach. The robot FRF corresponding to the arm configuration at 1.040 m along the linear path indicated in Figure 30 was predicted before and after updating the GPR model with the OMA based FRFs. Figure 34 schematically shows the validation test point in addition to the EMA and OMA points used for initial GPR model calibration and for model updating, respectively. Note that the validation point lies on the milling tool path. Therefore, to ensure proper validation, OMA-based FRFs were not computed within 50 mm of the validation point, and the model was updated using the remaining 10 OMA-based FRFs. The following section discusses the prediction accuracy of the hybrid modeling approach relative to the EMA-only model. In addition, the computational efficiency of the model updating procedure compared to complete model retraining is discussed.

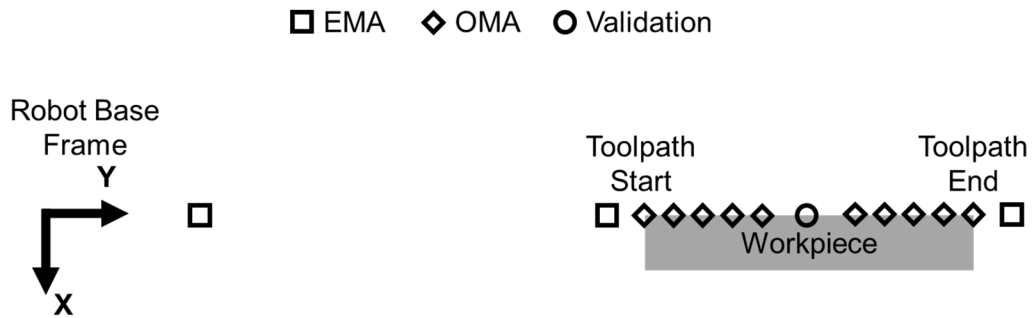


Figure 34. Top-down view of the calibration and validation points used in the experiments.

### 5.4.1 Prediction Accuracy

To predict the robot FRF using the GPR model, the robot FRF was separated into 131 frequency bins. Thus, each of the GPR models was calibrated for each frequency bin resulting in 131 GPR models that together describe the entire FRF for a single robot position. Figure 35 shows the prediction results before and after model updating. Note that before updating, the model prediction error for the dominant modes in the X, Y, and Z directions (8.3 Hz, 22.9 Hz, and 9.1 Hz, respectively) are 26%, 22%, and 33%, respectively. However, after updating the errors in the X, Y, and Z directions improve to 3.4%, 2.6%, and 4.2%, respectively. In addition, Table 12 lists the RMSE values for the entire FRF before and after model updating. Overall, it is seen that model updating improves the FRF prediction model accuracy across all frequencies.

Table 12. RMSE of FRF predictions (all units in  $\mu\text{m}/\text{N}$ ).

	X	Y	Z
Before Updating	0.275	0.156	0.540
After Updating	0.150	0.125	0.340

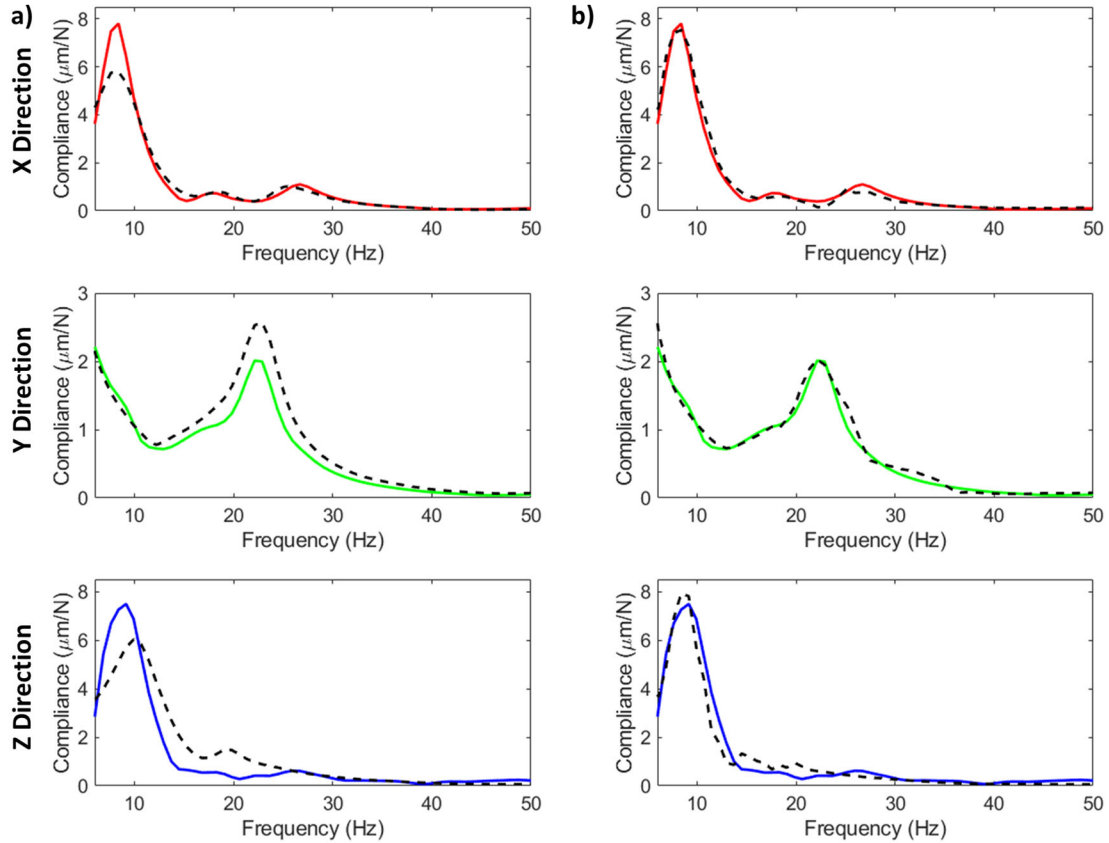


Figure 35. Model prediction a) before and b) after updating. The solid and dashed lines represent FRFs determined from modal impact hammer experiments and the model, respectively.

#### 5.4.2 Updating Iterations

The number of iterations in the quasi-Newton optimization search required for completely retraining the model, i.e. determining the hyperparameters from the EMA and OMA points as a single dataset, were compared against the number of iterations required for updating the EMA-calibrated GPR model using the updating methodology presented in the previous section. The number of iterations per model type was calculated by summing the total number of optimization iterations for all 131 GPR models. The average number

of iterations for the 131 GPR models are given in Table 13. Interestingly, the table shows that the proposed GPR model updating method requires significantly less number of average number of iterations compared to complete retraining of the model. Recall that the GPR models were initially calibrated using only 3 EMA-based FRFs and updated with 10 OMA-based FRFs. Thus, it is expected that complete retraining of the model with all 13 FRFs would not result in much difference in optimization iterations as opposed to updating with 10 FRFs. However, the results in Table 13 clearly show that using an initial guess of the hyperparameters based on only the 3 initial calibration FRFs is still superior to an initial guess starting from no prior information. The number of optimization iterations can be further reduced if the variance is assumed to be constant, which would be a valid assumption if the underlying physics and the statistics of the measured data were similar. Also, the computation time for all methods can be further reduced by parallelizing the calibration of the 131 GPR models though the total number of iterations would remain the same.

Table 13. Number of optimization iterations for complete retraining of GPR models vs. using model updating with OMA-based FRFs.

Complete Retraining	Updating
$4186 \pm 135$	$2078 \pm 103$

## 5.5 Summary

This chapter described and experimentally validated a hybrid statistical modelling approach to efficiently derive a higher fidelity model for predicting the entire FRF of an industrial robot by combining the use of Experimental Modal Analysis (EMA) with Operational Modal Analysis (OMA) of a milling process. The GPR modeling approach

presented in Chapter 3 was extended to enable the prediction of the entire pose-dependent FRF. A Bayesian inference approach for updating the EMA-calibrated GPR models of the robot FRF with OMA-based FRF data was shown to improve the model's RMSE by 34% compared to only EMA-based calibration. In addition, the proposed updating methodology was demonstrated to reduce the average number of iterations required to determine the optimal hyperparameters by 50.3%. Future work involves expanding this methodology to higher dimensional workspaces to further realize its practicality. In addition, a methodical approach to determine the optimal number of required points and tool paths for EMA and OMA, respectively, should be investigated to improve measurement efficiency.

## CHAPTER 6. CONCLUSIONS AND RECOMMENDATIONS

This chapter summarizes the main conclusions and the original contributions of this thesis. In addition, it recommends possible areas for future work.

### 6.1 Conclusions

The main conclusions of this thesis are summarized below.

#### 1. Data-Driven Modeling of the Modal Properties of a 6-DOF Industrial Robot

- A Gaussian Process Regression (GPR) based statistical modeling approach was developed to determine the pose-dependent modal parameters of a 6-dof industrial robot.
- The GPR model was found to accurately model the robot's dominant natural frequency, stiffness, and damping coefficient in its measurement space with maximum root mean square errors of 3.31 Hz, 150 KN/m, and 810 Ns/m, respectively.
- The experimental modal analysis results were compared with the modal parameters determined from an analytical model. This comparison showed that the undamped natural frequency and stiffness of the robot obtained from the analytical model deviate significantly from the experimental values as the robot arm is extended further from its base.
- The results showed that the average peak-to-valley vibrations predicted by the model followed the experimental trends measured by a laser tracker. The largest

and smallest errors between the predicted and measured values were 0.028 mm and 0.006 mm, respectively.

## **2. Pose-Dependent Optimal Controller in Robotic Milling**

- An optimal control methodology for active vibration suppression in robotic milling was developed using the outputs of the GPR model to formulate pose-dependent state-space matrices to solve the Linear Quadratic Regulator (LQR) problem.
- The control methodology was shown to reduce the vibration amplitudes from 0.93 mm to 0.39 mm and from 0.36 mm to 0.15 mm for 480 RPM and 960 RPM speeds, respectively. However, at 1440 RPM, the controller is unable to suppress the vibrations due to the 32 ms delay between the commanded input and the robot controller response.
- The controller was demonstrated to reduce milling vibration amplitudes by  $51\% \pm 13\%$  and  $43\% \pm 16\%$  in X and Z directions, respectively, which were also shown to be correlated with a decrease in machined surface deviations.

## **3. Data-Driven Model Augmentation using Milling Process Data**

- A statistical modelling methodology combining the use of impact hammer experiments and milling process measurements to predict the FRF of industrial robots was presented and experimentally validated.
- The OMA results show that cutting data pertaining to milling harmonics far from the robot's natural frequencies can be used to calculate the robot's FRF since the robot's natural modes were excited by background white noise in the milling force.

- Updating a previously calibrated statistical model from impact hammer experiments was shown to improve the RMSE by 34% while reducing the number of iterations by 50.3% required to determine the optimal hyperparameters and update the covariance matrix.

## **6.2 Original Contributions**

This research has yielded the following significant contributions:

1. A robust data-driven modeling approach to predict the tool tip vibrations of a 6-dof industrial robot arm in milling applications.
2. An optimal control strategy for online vibration suppression of a 6-dof articulated arm robot.
3. An approach to improve the prediction accuracy of a data-driven model of the robot's modal vibration parameters incorporating data obtained from milling experiments.

## **6.3 Recommendations for Future Work**

All methods presented in this thesis can apply to structures with pose-dependent vibratory behavior including cranes and humanoid robot structures. In addition, these methods can apply to alternate robotic applications including robotic painting and additive manufacturing. Even in low-force industrial robotic applications, high acceleration in the robot trajectory can induce inertial forces and result in end effector vibrations. Therefore, the methods in this thesis can be used to analyze and suppress inertial vibrations and improve robot performance. In addition, the data-driven modelling aspect can apply to

vibration suppression methods that require knowledge of structural modal properties including inertial stiffening and resonant frequency detuning. Inertial stiffening optimal control algorithms require a plant model describing how the command input influences the structural behavior. Knowledge of the pose-dependent plant model using the data-driven modelling approach in this thesis can be used in optimal controller formulation to significantly reduce the required manual tuning. In addition, resonant frequency detuning involves shunting the structural natural frequency when the external force approaches the structure's natural frequency. Using the data-driven modelling approach in this work for structures pose-dependent dynamics, the natural frequency can be tracked as a function of position and therefore the resonant frequency detuning approach can be used in a more optimal (as opposed to robust) fashion. However, note that use of the data-driven modelling for computation of the robot FRF is time consuming and may not satisfy control cycle time requirements in vibration suppression. Therefore, alternative efficient methods of utilizing the data-driven model for online vibration suppression techniques are critical. In addition, though more accurate, data-driven models are known to require more calibration measurements than analytical models. Therefore, a hybrid model combining both data-driven models and analytical models would be an optimal method of improving model accuracy while minimizing required measurements.

## APPENDIX A. MODAL PARAMETER MEASUREMENTS

Table A1. Modal parameters from calibration experiments. Z (mm),  $R_x$  (degree), and  $R_y$  (degree) were fixed at 325, 0, and 0, respectively.

Test no.	X [mm]	Y [mm]	Rz [deg]	Natural Frequency [Hz]			Stiffness [MN/m]			Damping Coefficient [KNS/m]		
				X	Y	Z	X	Y	Z	X	Y	Z
1	2100	-300	0	16.00	9.00	11.25	3.00	1.10	1.05	7.13	9.89	5.64
				16.00	8.50	11.25	3.00	1.20	1.05	7.13	10.30	5.64
				16.00	9.00	11.25	3.00	1.25	1.05	7.13	9.79	5.64
2	2100	-300	45	16.09	8.00	11.00	3.50	0.86	1.25	8.31	7.51	5.79
				16.09	8.00	11.00	3.50	0.84	1.00	8.31	8.20	4.63
				16.50	8.00	11.00	3.60	0.80	1.00	8.33	7.64	4.63
3	2100	-300	90	21.50	9.50	10.79	3.20	1.25	1.32	6.16	7.54	5.44
				21.50	9.00	10.79	3.20	0.95	1.32	6.16	6.05	5.44
				21.50	9.00	10.79	3.20	0.95	1.32	6.16	6.05	5.44
4	2100	-300	135	15.33	8.98	10.79	2.80	1.00	1.35	6.98	7.36	5.97
				15.33	8.98	10.79	2.80	1.00	1.35	6.98	7.36	5.97
				15.33	8.98	10.79	2.80	1.00	1.35	6.98	7.36	5.97
5	2100	-300	180	15.33	8.23	11.23	2.99	1.10	1.79	6.14	9.36	8.51
				15.33	8.23	11.23	2.50	1.00	1.79	5.14	8.51	8.51
				15.33	8.23	11.23	2.50	1.00	1.79	5.14	8.51	8.51
6	2100	0	0	16.00	9.28	11.50	2.50	1.55	1.40	5.47	9.04	6.78
				16.00	9.28	11.50	2.50	1.55	1.40	5.47	9.04	6.78
				16.00	9.28	11.50	2.50	1.55	1.40	5.47	9.04	6.78
7	2100	0	45	15.50	8.70	11.50	3.00	1.06	1.50	7.70	7.77	6.64
				15.50	8.70	11.50	3.00	1.06	1.50	7.70	7.77	6.64
				15.50	8.70	11.50	3.00	1.10	1.50	7.70	8.05	6.64
8	2100	0	90	21.83	10.00	11.50	3.50	1.00	1.40	5.10	5.41	6.20
				21.83	9.50	11.50	3.50	1.00	1.40	5.10	5.70	6.20
				21.83	9.50	11.50	3.50	1.00	1.40	5.10	5.86	6.20
9	2100	0	135	15.00	9.00	11.23	3.00	0.95	1.25	6.54	6.86	5.93
				15.00	9.00	11.23	3.00	0.95	1.25	6.54	6.86	5.93
				15.00	9.00	11.50	3.00	0.95	1.35	6.54	6.86	6.35
10	2100	0	180	15.33	9.50	11.00	2.88	1.25	1.70	5.91	7.54	8.36
				15.33	9.50	11.00	2.88	1.40	1.70	5.91	8.44	8.36
				15.33	9.50	11.00	2.88	1.40	1.70	5.91	8.44	8.36
11	2100	300	0	16.51	8.23	11.00	3.40	1.29	1.15	7.21	8.99	5.82
				16.51	7.97	11.00	3.40	1.35	1.15	7.54	9.71	5.82
				16.51	7.97	11.00	3.40	1.20	1.15	7.54	9.11	5.82
12	2100	300	45	15.50	8.23	11.25	3.00	1.10	1.40	6.78	7.23	6.73
				15.50	8.23	11.25	3.00	1.10	1.40	6.78	7.66	6.73
				15.50	8.23	11.25	3.00	1.10	1.40	6.78	7.66	6.73

13	2100	300	90	21.00	8.23	11.00	3.20	1.05	1.35	5.34	7.72	6.14
				21.00	8.23	11.25	3.20	1.05	1.60	5.34	7.72	7.24
				21.00	8.23	11.25	3.20	1.00	1.60	5.34	6.96	7.24
14	2100	300	135	15.76	8.75	11.23	3.00	1.10	1.20	6.97	7.04	5.70
				15.76	8.75	11.23	3.00	1.10	1.45	6.97	7.04	6.88
				15.76	8.75	11.23	3.00	1.10	1.20	6.97	7.04	5.70
15	2100	300	180	15.25	9.00	11.00	2.60	1.50	1.30	6.51	8.60	6.40
				15.25	9.00	11.00	2.60	1.50	1.30	6.51	8.60	6.40
				15.25	9.00	11.00	2.60	1.50	1.30	7.05	8.60	6.40
16	2100	600	0	16.94	7.97	11.25	3.10	1.40	1.20	6.99	10.60	6.28
				16.94	7.97	11.25	3.10	1.40	1.10	6.99	10.60	5.60
				17.00	7.97	11.25	3.40	1.40	1.20	7.64	10.60	6.28
17	2100	600	45	16.09	8.53	11.25	2.85	1.10	1.10	7.05	7.59	5.76
				15.50	8.53	11.25	2.85	1.30	1.10	7.32	8.49	5.76
				16.09	8.53	11.25	2.85	1.30	1.00	7.05	8.49	4.95
18	2100	600	90	22.00	9.25	11.23	3.50	0.88	1.50	6.08	6.29	7.12
				22.00	9.25	11.23	3.30	0.88	1.50	5.73	6.29	7.12
				22.00	9.25	11.23	3.30	0.83	1.50	5.73	5.93	7.12
19	2100	600	135	16.50	9.50	11.23	3.50	1.10	1.35	7.43	7.74	6.89
				16.50	9.50	11.23	3.75	1.10	1.35	7.96	7.74	6.51
				16.50	9.50	11.23	3.05	0.95	1.25	6.47	6.37	6.02
20	2100	600	180	15.33	8.70	11.23	2.80	1.30	1.25	6.40	9.04	6.55
				15.33	8.70	11.23	2.80	1.30	1.25	6.40	9.04	6.55
				15.33	8.70	11.23	2.80	1.30	1.25	6.40	9.04	6.55
21	2400	-300	0	16.51	8.53	10.18	3.50	1.20	0.98	6.07	8.51	5.49
				16.51	8.53	10.18	4.00	1.20	0.98	6.94	8.51	5.49
				16.51	8.53	10.18	3.50	1.20	0.98	6.75	8.51	5.49
22	2400	-300	45	16.51	7.78	10.18	4.00	0.93	0.98	8.87	6.47	5.49
				16.51	7.78	10.18	4.00	0.93	1.05	9.25	6.47	5.91
				16.51	7.78	10.18	4.00	0.93	1.05	9.25	6.47	5.91
23	2400	-300	90	22.50	8.23	10.50	4.50	0.90	1.30	7.00	5.92	6.70
				22.50	8.75	10.50	4.50	0.83	1.20	7.64	5.59	6.18
				20.00	8.75	10.50	3.80	0.83	1.10	6.96	5.59	5.34
24	2400	-300	135	15.76	8.53	10.50	3.20	0.95	1.15	7.77	6.03	5.58
				15.76	8.53	10.50	3.20	0.95	1.15	7.77	6.03	5.93
				15.76	8.25	10.50	3.20	0.93	1.15	7.77	6.07	5.93
25	2400	-300	180	15.76	7.50	10.50	3.60	1.20	1.30	8.74	8.66	6.70
				15.76	7.50	10.50	3.60	1.10	1.30	8.74	7.94	6.70
				15.76	7.50	10.50	3.60	1.10	1.20	8.74	7.94	6.18
26	2400	0	0	16.51	7.50	10.00	4.00	1.15	0.99	8.85	8.79	5.67
				16.51	7.50	10.00	4.00	1.05	0.99	8.85	8.02	5.67
				16.51	7.50	10.00	4.00	1.15	0.99	8.85	8.79	5.67
27	2400	0	45	16.51	8.50	10.25	4.20	0.95	1.10	9.29	6.40	5.47
				16.51	8.50	10.25	4.20	0.95	1.10	9.29	6.40	5.47
				16.51	8.50	10.50	4.20	0.95	1.25	9.29	6.40	6.06
28	2400	0	90	22.00	8.23	10.50	3.75	0.88	1.25	6.51	6.09	6.06

				22.00	8.23	10.47	3.75	0.88	1.00	6.51	6.09	5.44
				22.00	8.23	10.47	3.75	0.88	1.00	6.51	6.09	5.44
29	2400	0	135	15.76	8.23	10.50	3.40	0.90	1.10	8.25	6.27	5.67
				15.76	8.23	10.50	3.40	0.90	1.15	8.25	6.27	5.93
				15.76	8.23	10.50	3.40	0.90	1.15	8.25	6.27	5.93
30	2400	0	180	15.76	8.23	10.47	3.27	1.20	1.20	7.27	8.59	6.53
				15.76	8.23	10.47	3.27	1.00	1.25	7.27	7.16	6.80
				15.76	8.23	10.47	3.27	1.10	1.25	7.27	7.87	6.80
31	2400	300	0	16.85	7.78	10.47	5.00	1.35	1.00	9.45	10.50	5.44
				16.85	7.78	10.47	5.00	1.10	1.05	9.45	8.10	5.72
				16.85	7.78	10.47	5.00	1.10	1.00	9.45	8.10	5.44
32	2400	300	45	16.50	7.78	11.00	4.30	0.90	1.10	8.30	6.48	5.70
				16.50	7.78	11.00	4.30	0.90	1.10	8.30	6.48	5.70
				16.50	7.78	11.00	4.30	0.93	1.10	8.30	6.66	5.70
33	2400	300	90	21.50	8.50	10.47	4.50	0.88	1.10	6.00	6.06	5.99
				21.50	8.50	10.47	4.50	0.88	1.00	6.00	6.06	5.44
				21.50	8.50	10.47	4.50	0.95	1.10	6.00	6.76	5.99
34	2400	300	135	16.09	8.25	10.47	4.00	0.85	1.00	8.70	5.90	5.32
				16.09	8.25	10.47	3.80	0.85	1.05	8.27	5.90	5.43
				16.09	8.25	10.47	3.80	0.85	1.05	8.27	5.90	5.43
35	2400	300	180	15.76	8.75	10.50	3.20	1.15	1.15	7.11	7.53	6.70
				15.76	8.75	10.50	3.00	1.15	1.15	6.67	7.53	6.70
				15.76	8.75	10.50	3.00	1.15	1.20	6.67	7.53	7.28
36	2400	600	0	17.27	8.00	10.00	4.20	1.15	0.97	8.13	8.80	5.71
				17.27	8.00	10.00	4.20	1.15	0.97	8.13	8.80	5.71
				17.27	8.00	10.00	4.20	1.15	0.97	8.13	8.80	5.71
37	2400	600	45	16.75	8.53	10.50	3.80	1.10	0.93	7.58	7.22	5.19
				16.75	8.53	10.50	4.00	1.10	0.93	7.60	7.22	5.19
				16.75	8.53	10.50	4.00	1.10	0.93	7.60	7.22	5.19
38	2400	600	90	21.50	7.78	10.50	3.75	0.83	1.05	5.55	6.28	5.09
				21.50	7.25	10.50	4.20	0.75	1.20	5.60	6.59	5.82
				21.50	7.25	10.50	4.20	0.75	1.05	5.60	6.59	5.09
39	2400	600	135	16.09	7.78	10.50	4.00	0.90	1.10	8.70	6.26	5.34
				16.09	8.25	10.50	4.00	0.92	1.10	8.70	6.39	5.67
				16.09	8.00	10.50	4.00	0.88	1.05	8.70	6.27	5.41
40	2400	600	180	15.76	8.23	10.18	3.35	1.05	1.15	6.77	7.93	6.83
				15.76	8.23	10.18	3.35	0.95	1.15	6.77	7.35	7.01
				15.76	8.23	10.18	3.35	0.98	1.10	6.77	7.54	6.71
41	2700	-300	0	64.00	8.23	10.00	4.75	0.85	0.85	1.28	6.21	4.87
				64.00	8.23	10.00	4.75	0.88	0.85	1.28	6.77	4.87
				64.00	8.23	10.00	4.75	0.88	0.80	1.28	6.77	4.58
42	2700	-300	45	17.27	8.23	10.00	5.40	0.70	0.95	10.90	5.66	5.14
				17.27	8.23	10.00	5.40	0.70	0.95	10.90	5.66	5.14
				17.27	8.23	10.00	5.40	0.70	0.95	10.90	5.66	5.14
43	2700	-300	90	22.94	7.50	10.00	7.00	0.70	0.90	8.74	5.35	4.87
				22.94	7.50	9.50	7.00	0.70	0.90	8.74	5.35	5.13

				22.94	7.50	9.50	7.00	0.70	0.90	8.74	5.35	5.13
44	2700	-300	135	16.09	7.78	9.50	5.00	0.80	0.98	9.89	5.89	5.55
				16.09	7.78	9.50	5.00	0.70	0.98	9.89	5.16	5.55
				16.09	7.78	9.50	5.00	0.70	0.98	9.89	5.16	5.55
45	2700	-300	180	61.87	7.25	9.50	4.10	0.75	1.00	1.16	6.75	6.37
				63.00	7.50	9.50	4.50	0.83	1.00	1.36	7.18	6.37
				63.00	7.50	9.50	4.00	0.78	1.00	1.11	6.74	6.37
46	2700	0	0	64.00	7.50	9.73	4.50	0.78	0.80	1.22	6.74	5.03
				64.00	7.50	9.73	4.50	0.78	0.80	1.22	6.74	5.03
				64.00	7.50	9.73	4.50	0.78	0.80	1.22	6.74	5.03
47	2700	0	45	17.27	8.09	9.73	5.50	0.73	0.80	10.10	5.13	4.84
				17.27	8.09	9.73	5.50	0.73	0.80	10.10	5.13	4.84
				17.27	8.09	9.73	5.50	0.73	0.80	10.10	5.13	4.84
48	2700	0	90	23.00	8.50	9.73	5.50	0.78	0.92	7.61	5.22	5.56
				23.00	8.25	9.73	5.50	0.76	0.92	7.61	5.24	5.11
				23.00	8.25	9.73	5.50	0.70	0.90	7.61	4.86	5.01
49	2700	0	135	16.09	7.24	9.73	5.25	0.73	0.90	9.80	6.06	5.45
				16.09	7.50	9.73	5.25	0.75	0.90	9.80	6.05	5.45
				16.09	7.50	9.73	5.25	0.75	0.90	9.80	6.05	5.45
50	2700	0	180	63.00	8.09	9.73	4.00	0.85	0.93	1.01	6.52	5.45
				63.00	8.09	9.73	4.00	0.85	0.93	1.01	6.52	5.45
				63.00	8.09	9.73	4.00	0.85	0.93	1.01	6.52	5.45
51	2700	300	0	63.44	7.46	9.73	4.00	0.83	0.78	1.20	6.66	4.71
				63.44	7.49	9.73	4.00	0.85	0.78	1.20	7.22	4.71
				63.44	7.49	9.73	4.00	0.83	0.78	1.20	7.01	4.71
52	2700	300	45	17.00	7.78	9.73	5.25	0.80	0.78	11.30	6.29	4.71
				17.00	7.78	9.73	5.25	0.80	0.78	11.30	6.29	4.71
				17.00	7.78	9.73	5.25	0.80	0.78	11.30	6.29	4.71
53	2700	300	90	22.00	7.78	9.73	5.75	0.70	0.83	7.90	5.58	4.99
				22.00	7.78	9.73	5.75	0.70	0.83	7.90	5.58	4.99
				22.00	7.78	9.73	5.75	0.68	0.83	7.90	5.39	4.99
54	2700	300	135	16.51	8.00	9.73	4.00	0.70	0.88	8.85	5.36	5.30
				16.51	8.00	9.73	4.50	0.65	0.88	9.95	4.97	5.30
				16.51	8.00	9.73	4.50	0.65	0.88	9.95	4.97	5.30
55	2700	300	180	63.00	7.78	9.73	4.30	0.93	0.90	1.06	7.33	5.45
				63.00	8.00	9.73	4.30	0.90	0.90	1.06	6.89	5.59
				63.00	8.00	9.73	4.30	0.90	0.90	1.06	6.89	5.59
56	2700	600	0	63.84	7.49	9.28	3.50	0.83	0.85	1.14	7.36	5.25
				63.84	7.49	9.75	3.75	0.83	0.80	1.23	7.36	4.70
				63.84	8.00	9.75	3.75	0.80	0.80	1.23	6.53	4.70
57	2700	600	45	17.27	7.50	9.50	5.25	0.90	0.88	10.60	6.88	4.98
				17.27	7.50	9.50	5.25	0.85	0.88	10.60	6.49	4.98
				17.27	7.50	9.50	5.00	0.85	0.88	10.10	6.49	4.98
58	2700	600	90	22.00	7.78	9.50	5.00	0.75	0.88	7.96	5.90	4.98
				22.00	7.78	9.50	5.00	0.75	0.88	7.96	5.90	4.98
				22.00	7.78	9.50	5.00	0.75	0.88	7.96	5.90	4.98

59	2700	600	135	16.85	7.78	9.50	5.00	0.70	0.88	9.45	5.58	4.98
				16.85	7.78	9.50	5.00	0.70	0.93	9.45	5.58	5.27
				16.85	8.00	9.50	0.65	0.93	0.93	9.45	5.43	5.27
60	2700	600	180	64.50	7.49	9.50	0.77	0.98	0.98	1.05	6.74	5.88
				64.50	8.00	10.00	0.80	0.95	0.95	1.05	6.53	5.44
				64.50	8.00	10.00	0.77	0.95	0.95	1.05	6.28	5.44

---

Table A2. External validation measurements. Z (mm), R<sub>x</sub> (degree), and R<sub>y</sub> (degree) were fixed at 325, 0, and 0, respectively.

Test no.	X [mm]	Y [mm]	Rz [deg]	Natural Frequency [Hz]			Stiffness [MN/m]			Damping Coefficient [KNs/m]		
				X	Y	Z	X	Y	Z	X	Y	Z
1	2250	-150	0	16.00	8.50	11.33	3.75	1.20	1.70	7.46	8.32	7.16
2	2250	-150	45	16.09	8.00	10.75	3.25	1.00	1.30	7.07	8.36	5.77
3	2250	-150	90	19.25	8.50	11.00	2.90	0.88	1.15	4.80	7.54	5.32
4	2250	-150	135	15.51	8.00	11.00	3.15	0.96	1.50	7.11	7.45	6.51
5	2250	-150	180	15.10	8.25	10.75	3.25	1.12	1.35	6.51	8.21	6.00
6	2250	150	0	16.50	7.50	10.75	4.00	1.10	1.35	7.72	8.87	6.00
7	2250	150	45	18.00	8.50	11.01	3.50	0.97	1.35	6.85	6.54	5.85
8	2250	150	90	19.13	8.00	10.79	3.00	0.85	1.35	4.49	6.09	6.37
9	2250	150	135	18.00	8.00	10.75	3.50	0.96	0.94	7.18	6.88	4.71
10	2250	150	180	15.00	8.25	10.63	3.00	1.18	1.05	6.68	8.00	5.01
11	2250	450	0	16.50	8.00	11.25	4.25	1.15	1.55	8.21	8.69	7.02
12	2250	450	45	17.00	8.25	10.75	2.65	1.00	1.10	5.91	6.94	5.54
13	2250	450	90	19.42	8.01	11.00	1.99	0.90	1.15	4.13	6.26	6.09
14	2250	450	135	16.27	8.50	10.63	3.50	1.03	1.12	7.53	6.94	6.54
15	2250	450	180	15.00	8.50	10.41	3.25	1.15	1.30	6.66	7.75	7.35
16	2550	-150	0	17.27	9.31	9.95	5.19	1.05	1.10	10.49	7.64	6.69
17	2550	-150	45	18.03	7.50	10.00	4.00	0.78	0.83	7.06	6.66	4.49
18	2550	-150	90	19.25	7.60	10.00	3.50	0.73	1.03	5.22	7.01	5.23
19	2550	-150	135	16.00	8.23	9.88	4.50	0.78	0.88	8.06	5.99	4.82
20	2550	-150	180	15.76	7.50	10.10	3.25	0.90	1.02	6.56	7.64	5.95
21	2550	150	0	16.85	7.00	10.03	5.98	0.80	0.93	10.18	7.09	4.99
22	2550	150	45	17.65	7.25	10.03	3.90	0.73	0.88	7.03	5.73	4.72
23	2550	150	90	19.25	7.50	10.10	3.25	0.79	0.90	4.85	6.54	5.07
24	2550	150	135	18.00	7.75	10.10	5.00	0.80	0.85	8.80	6.08	4.62
25	2550	150	180	15.76	7.75	10.10	3.25	0.85	0.83	6.56	6.63	4.55
26	2550	450	0	16.85	7.50	9.73	5.50	0.92	0.88	10.39	7.81	5.72
27	2550	450	45	17.65	8.00	10.00	4.00	0.75	0.83	6.85	5.97	4.99
28	2550	450	90	19.25	7.75	10.00	3.15	0.73	0.83	4.95	6.25	5.12
29	2550	450	135	16.44	7.75	9.88	6.00	0.75	0.80	8.07	6.24	4.67
30	2550	450	180	15.76	8.01	9.75	3.10	0.82	0.80	6.26	6.48	4.90

## REFERENCES

- [1] H.N. Huynh, E. Riviere-Lorphevre, O. Verlinden, Report of robotic machining measurements using a stäubli tx200 robot: Application to milling, International Design Engineering Technical Conferences and Computers and Information in Engineering Conference, 58189 (2017) V05BT08A007.
- [2] A. Verl, A. Valente, S. Melkote, C. Brecher, E. Ozturk, L.T. Tunc, Robots in machining, CIRP Annals, 68 (2019) 799-822.
- [3] H. Zhang, J. Wang, G. Zhang, Z. Gan, Z. Pan, H. Cui, Z. Zhu, Machining with flexible manipulator: Toward improving robotic machining performance, 2005 IEEE/ASME International Conference on Advanced Intelligent Mechatronics, (2005) 1127-1132.
- [4] I. Tyapin, G. Hovland, P. Kosonen, T. Linna, Identification of a static tool force model for robotic face milling, 2014 IEEE/ASME 10th International Conference on Mechatronic and Embedded Systems and Applications, (2014) 1-6.
- [5] L. Cen, S.N. Melkote, Effect of robot dynamics on the machining forces in robotic milling, Procedia Manufacturing, 10 (2017) 486-496.
- [6] S. Mejri, V. Gagnol, T.-P. Le, L. Sabourin, P. Ray, P. Paultre, Dynamic characterization of machining robot and stability analysis, The International Journal of Advanced Manufacturing Technology, 82 (2016) 351-359.
- [7] L. Tunc, D. Stoddart, Tool path pattern and feed direction selection in robotic milling for increased chatter-free material removal rate, The International Journal of Advanced Manufacturing Technology, 89 (2017) 2907-2918.
- [8] P.P. Radecki, K.M. Farinholt, G. Park, M.T. Bement, Vibration suppression in cutting tools using a collocated piezoelectric sensor/actuator with an adaptive control algorithm, Journal of Vibration and Acoustics, 132 (2010) 051002.
- [9] N.-C. Tsai, L.-W. Shih, R.-M. Lee, Spindle vibration suppression for advanced milling process by using self-tuning feedback control, The International Journal of Advanced Manufacturing Technology, 48 (2010) 1-10.
- [10] B. Peeters, G. De Roeck, Stochastic system identification for operational modal analysis: A review, Journal of Dynamic Systems, Measurement, and Control, 123 (2001) 659-667.
- [11] A. Klimchik, D. Bondarenko, A. Pashkevich, S. Briot, B. Furet, Compliance error compensation in robotic-based milling, Informatics in Control, Automation and Robotics, (2014) 197-216.

- [12] S. Cetinkunt, W.J. Book, Symbolic modeling and dynamic simulation of robotic manipulators with compliant links and joints, *Robotics and Computer-Integrated Manufacturing*, 5 (1989) 301-310.
- [13] G. Alici, B. Shirinzadeh, Enhanced stiffness modeling, identification and characterization for robot manipulators, *IEEE Transactions on Robotics*, 21 (2005) 554-564.
- [14] G. Palli, C. Melchiorri, T. Wimbock, M. Grebenstein, G. Hirzinger, Feedback linearization and simultaneous stiffness-position control of robots with antagonistic actuated joints, 2007 IEEE International Conference on Robotics and Automation, (2007) 4367-4372.
- [15] U. Schneider, M. Momeni-K, M. Ansaloni, A. Verl, Stiffness modeling of industrial robots for deformation compensation in machining, 2014 IEEE/RSJ International Conference on Intelligent Robots and Systems, (2014) 4464-4469.
- [16] S. Mousavi, V. Gagnol, B.C. Bouzgarrou, P. Ray, Dynamic modeling and stability prediction in robotic machining, *The International Journal of Advanced Manufacturing Technology*, 88 (2017) 3053-3065.
- [17] B. Armstrong, O. Khatib, J. Burdick, The explicit dynamic model and inertial parameters of the puma 560 arm, 1986 IEEE International Conference on Robotics and Automation, 3 (1986) 510-518.
- [18] Z. Pan, H. Zhang, Z. Zhu, J. Wang, Chatter analysis of robotic machining process, *Journal of Materials Processing Technology*, 173 (2006) 301-309.
- [19] C.H. An, C.G. Atkeson, J.M. Hollerbach, Estimation of inertial parameters of rigid body links of manipulators, 1985 24th IEEE Conference on Decision and Control, (1985) 990-995.
- [20] S. Adhikari, Damping modelling using generalized proportional damping, *Journal of Sound and Vibration*, 293 (2006) 156-170.
- [21] M. Ruderman, F. Hoffmann, T. Bertram, Modeling and identification of elastic robot joints with hysteresis and backlash, *IEEE Transactions on Industrial Electronics*, 56 (2009) 3840-3847.
- [22] J. De Caigny, J.F. Camino, J. Swevers, Interpolation-based modeling of mimo lpv systems, *IEEE Transactions on Control Systems Technology*, 19 (2011) 46-63.
- [23] F. Ferranti, Y. Rolain, A local identification method for linear parameter-varying systems based on interpolation of state-space matrices and least-squares approximation, *Mechanical Systems and Signal Processing*, 82 (2017) 478-489.
- [24] G. Chen, Y. Li, X. Liu, Pose-dependent tool tip dynamics prediction using transfer learning, *International Journal of Machine Tools and Manufacture*, 137 (2019) 30-41.

- [25] C. Deng, J. Miao, B. Wei, Y. Feng, Y. Zhao, Evaluation of machine tools with position-dependent milling stability based on kriging model, *International Journal of Machine Tools and Manufacture*, 124 (2018) 33-42.
- [26] K.B. Kaldestad, I. Tyapin, G. Hovland, Robotic face milling path correction and vibration reduction, *Advanced Intelligent Mechatronics (AIM)*, 2015 IEEE International Conference on, (2015) 543-548.
- [27] J. Li, B. Li, N. Shen, H. Qian, Z. Guo, Effect of the cutter path and the workpiece clamping position on the stability of the robotic milling system, *The International Journal of Advanced Manufacturing Technology*, 89 (2017) 2919-2933.
- [28] S. Mousavi, V. Gagnol, B.C. Bouzgarrou, P. Ray, Stability optimization in robotic milling through the control of functional redundancies, *Robotics and Computer-Integrated Manufacturing*, 50 (2018) 181-192.
- [29] Z. Pan, H. Zhang, Analysis and suppression of chatter in robotic machining process, *International Conference on Control, Automation and Systems*, (2007) 595-600.
- [30] U. Schneider, M. Drust, M. Ansaloni, C. Lehmann, M. Pellicciari, F. Leali, J.W. Gunnink, A. Verl, Improving robotic machining accuracy through experimental error investigation and modular compensation, *The International Journal of Advanced Manufacturing Technology*, 85 (2016) 3-15.
- [31] G.-C. Vosniakos, E. Matsas, Improving feasibility of robotic milling through robot placement optimisation, *Robotics and Computer-Integrated Manufacturing*, 26 (2010) 517-525.
- [32] J. Wang, H. Zhang, T. Fuhlbrigge, Improving machining accuracy with robot deformation compensation, *2009 IEEE/RSJ International Conference on Intelligent Robots and Systems*, (2009) 3826-3831.
- [33] L. Cen, S.N. Melkote, Cct-based mode coupling chatter avoidance in robotic milling, *Journal of Manufacturing Processes*, 29 (2017) 50-61.
- [34] L. Cen, S.N. Melkote, J. Castle, H. Appelman, A wireless force-sensing and model-based approach for enhancement of machining accuracy in robotic milling, *IEEE/ASME Transactions on Mechatronics*, 21 (2016) 2227-2235.
- [35] J. Franks, Z. Pan, H. Zhang, Robotic machining from programming to process control: A complete solution by force control, *Industrial Robot: An International Journal*, (2008).
- [36] O. Sörnmo, B. Olofsson, U. Schneider, A. Robertsson, R. Johansson, Increasing the milling accuracy for industrial robots using a piezo-actuated high-dynamic micro manipulator, *2012 IEEE/ASME International Conference on Advanced Intelligent Mechatronics*, (2012) 104-110.

- [37] M.M. Daniali, G. Vossoughi, Intelligent active vibration control of constrained manipulators in robotic deburring, 2009 International Conference on Industrial Mechatronics and Automation, (2009) 76-80.
- [38] Z. Wang, P. Keogh, Active vibration control for robotic machining, ASME 2017 International Mechanical Engineering Congress and Exposition, (2017) V002T002A079-V002T002A079.
- [39] R. Vinter, Optimal control, Springer Science & Business Media, 2010.
- [40] C.M.G. Bort, M. Leonesio, P. Bosetti, A model-based adaptive controller for chatter mitigation and productivity enhancement in cnc milling machines, Robotics and Computer-Integrated Manufacturing, 40 (2016) 34-43.
- [41] H. Moradi, G. Vossoughi, M.R. Movahhedy, H. Salarieh, Suppression of nonlinear regenerative chatter in milling process via robust optimal control, Journal of Process Control, 23 (2013) 631-648.
- [42] F. Beltrán Carbajal, E. Chávez Conde, A. Favela Contrera, R.F. Vázquez Bautista, Active perturbation rejection in motion control of milling machine tools, Revista Facultad de Ingeniería Universidad de Antioquia, (2013) 193-204.
- [43] D.G. Ford, A. Myers, F. Haase, S. Lockwood, A. Longstaff, Active vibration control for a cnc milling machine, Proceedings of the Institution of Mechanical Engineers, Part C: Journal of Mechanical Engineering Science, 228 (2014) 230-245.
- [44] A. Brandt, Noise and vibration analysis: Signal analysis and experimental procedures, John Wiley & Sons, 2011.
- [45] C. Chen, F. Peng, R. Yan, X. Tang, Y. Li, Z. Fan, Rapid prediction of posture-dependent frf of the tool tip in robotic milling, Robotics and Computer-Integrated Manufacturing, 64 (2020) 101906.
- [46] H.N. Huynh, H. Assadi, E. Rivière-Lorphèvre, O. Verlinden, K. Ahmadi, Modelling the dynamics of industrial robots for milling operations, Robotics and Computer-Integrated Manufacturing, 61 (2020) 101852.
- [47] N. Suzuki, Y. Kurata, T. Kato, R. Hino, E. Shamoto, Identification of transfer function by inverse analysis of self-excited chatter vibration in milling operations, Precision Engineering, 36 (2012) 568-575.
- [48] D. Poddar, M. Shunmugam, Development of an automated modal extraction methodology through oma by random cutting excitation of a legacy milling machine, Mechanical Systems and Signal Processing, 122 (2019) 448-462.
- [49] B. Li, H. Cai, X. Mao, J. Huang, B. Luo, Estimation of cnc machine-tool dynamic parameters based on random cutting excitation through operational modal analysis, International Journal of Machine Tools and Manufacture, 71 (2013) 26-40.

- [50] A. Maamar, T.-P. Le, V. Gagnol, L. Sabourin, Modal identification of a machine tool structure during machining operations, *The International Journal of Advanced Manufacturing Technology*, (2019) 1-12.
- [51] A. Maamar, V. Gagnol, T.-P. Le, L. Sabourin, Pose-dependent modal behavior of a milling robot in service, *The International Journal of Advanced Manufacturing Technology*, 107 (2020) 527-533.
- [52] S. Mejri, V. Gagnol, T.-P. Le, L. Sabourin, P. Ray, P. Paultre, Identification du comportement dynamique d'un robot d'usinage en service', in, *MUGV*, 2014.
- [53] J. Berthold, M. Kolouch, V. Wittstock, M. Putz, Identification of modal parameters of machine tools during cutting by operational modal analysis, *Procedia CIRP*, 77 (2018) 473-476.
- [54] B. Powalka, K. Jemielniak, Stability analysis in milling of flexible parts based on operational modal analysis, *CIRP Journal of Manufacturing Science and Technology*, 9 (2015) 125-135.
- [55] I. Zaghbani, V. Songmene, Estimation of machine-tool dynamic parameters during machining operation through operational modal analysis, *International Journal of Machine Tools and Manufacture*, 49 (2009) 947-957.
- [56] K. Zhu, G. Hong, Y. Wong, W. Wang, Cutting force denoising in micro-milling tool condition monitoring, *International Journal of Production Research*, 46 (2008) 4391-4408.
- [57] S. Wojciechowski, R.W. Maruda, G.M. Krolczyk, P. Niesłony, Application of signal to noise ratio and grey relational analysis to minimize forces and vibrations during precise ball end milling, *Precision Engineering*, 51 (2018) 582-596.
- [58] P. Mohanty, D.J. Rixen, Operational modal analysis in the presence of harmonic excitation, *Journal of Sound and Vibration*, 270 (2004) 93-109.
- [59] B. Peeters, B. Cornelis, K. Janssens, H. Van der Auweraer, Removing disturbing harmonics in operational modal analysis, *Proceedings of International Operational Modal Analysis Conference*, Copenhagen, Denmark, (2007).
- [60] S. Chauhan, M. Hansen, D. Tcherniak, Application of operational modal analysis and blind source separation/independent component analysis techniques to wind turbines, *Proceedings of XXVII International Modal Analysis Conference*, Orlando (FL), USA, (2009).
- [61] C.E. Rasmussen, Gaussian processes in machine learning, *Advanced lectures on machine learning*, Springer, 2004, pp. 63-71.
- [62] C. Dumas, S. Caro, S. Garnier, B. Furet, Joint stiffness identification of six-revolute industrial serial robots, *Robotics and Computer-Integrated Manufacturing*, 27 (2011) 881-888.

- [63] U. Schneider, M. Ansaloni, M. Drust, F. Leali, A. Verl, Experimental investigation of sources of error in robot machining, International Workshop on Robotics in Smart Manufacturing, (2013) 14-26.
- [64] J.H. Ginsberg, Mechanical and structural vibrations: Theory and applications, Wiley New York, 2001.
- [65] Y. Altintas, Manufacturing automation: Metal cutting mechanics, machine tool vibrations, and cnc design, Cambridge University Press, 2012.
- [66] R.N. Bracewell, R.N. Bracewell, The fourier transform and its applications, McGraw-Hill New York, 1986.
- [67] L.C. Phillips, Control of a dual inverted pendulum system using linear-quadratic and h-infinity methods, in, Massachusetts Institute of Technology, 1994.
- [68] V. Nguyen, S.N. Melkote, Identification of industrial robot frequency response function for robotic milling using operational modal analysis, Procedia Manufacturing, (2020).
- [69] V. Nguyen, S.N. Melkote, Modeling of flange-mounted force sensor frequency response function for inverse filtering of forces in robotic milling, Procedia Manufacturing, 34 (2019) 804-812.
- [70] B.G. Pfrommer, M. Côté, S.G. Louie, M.L. Cohen, Relaxation of crystals with the quasi-newton method, Journal of Computational Physics, 131 (1997) 233-240.
- [71] J.D. Head, M.C. Zerner, A broyden—fletcher—goldfarb—shanno optimization procedure for molecular geometries, Chemical Physics Letters, 122 (1985) 264-270.
- [72] M. Seeger, C. Williams, N. Lawrence, Fast forward selection to speed up sparse gaussian process regression, in, 2003.
- [73] Z. Chen, B. Wang, How priors of initial hyperparameters affect gaussian process regression models, Neurocomputing, 275 (2018) 1702-1710.
- [74] A. Ranganathan, M.-H. Yang, J. Ho, Online sparse gaussian process regression and its applications, IEEE Transactions on Image Processing, 20 (2010) 391-404.
- [75] A. Gelman, Prior distributions for variance parameters in hierarchical models (comment on article by browne and draper), Bayesian Analysis, 1 (2006) 515-534.
- [76] S. Chan, P. Treleaven, L. Capra, Continuous hyperparameter optimization for large-scale recommender systems, 2013 IEEE International Conference on Big Data, (2013) 350-358.
- [77] BlueSwarf, <http://www.blueswarf.com/>, April 28, 2020